UNIVERSITÀ DEGLI STUDI DI MILANO

Dottorato di Ricerca in Fisica, Astrofisica e Fisica Applicata

The Borexino Experiment: Test of the Purification Systems and Data Analysis in the Counting Test Facility

Director of the Doctoral School: Prof. Rodolfo Bonifacio

Advisors: Prof. Gianpaolo Bellini
Prof. Wolfgang Hampel

Davide Franco
Ph.D. Thesis
XVII Cycle

Academic Year: 2004-2005

Joint Degree Program "Cotutelle" with the

RUPERTO-CAROLA UNIVERSITY OF HEIDELBERG

Combined Faculties for the Natural Sciences and for Mathematics

for the degree of

Doctor of Natural Sciences

The Borexino Experiment: Test of the Purification Systems and Data Analysis in the Counting Test Facility

Davide Franco

Advisors: Prof. Gianpaolo Bellini
Prof. Wolfgang Hampel

Introduction

The past six years have witnessed an impressive evolution in the solar neutrino research. The exciting recent results from solar (SNO and SuperKamiokande) and reactor (KamLAND) neutrino experiments have provided robust evidences in favor of neutrino oscillation as explanation of the missing solar neutrino problem.

The next challenge is the accurate measurement in real time of the solar neutrino flux and spectra below 1 MeV. According to the Standard Solar Model, more than 98% of the solar neutrino flux is predicted to lie below 1 MeV. A measurement of the *pp* and ^{7}Be fluxes would represent a strong improvement in our understanding of energy production in the Sun. In the neutrino oscillation physics, MSW matter effects due to the neutrinos' passage through the solar plasma are negligible in the low energy domain and will permit direct observation of the vacuum oscillation. Moreover, measuring neutrino flux below 1 MeV could reveal new physics.

Borexino is a real-time experiment for low energy neutrino spectroscopy. The installation is almost completed at the underground Gran Sasso National Laboratories (3800 mwe depth). Borexino is specifically designed to measure the mono-energetic (866 keV) ^{7}Be flux via neutrino-electron elastic scattering in ultra-pure organic scintillation liquid. The separation of signal and background relies on the identification of the Compton-like edge in the recoil electron energy spectrum at 667 keV.

The Borexino's 300-ton liquid scintillator target is housed in a 8.5 m diameter spherical nylon membrane and shielded by 1000 tons of buffer fluid. 2200 photomultiplier tubes, mounted on a stainless steel sphere, observes the scintillation light. A second nylon vessel (11.5 m diameter) protects the active target from radon emanated at the periphery of the detector.

The physics potential of Borexino strongly depends on the unprecedented requirements of low level background. In order to reach a signal to background ratio equal to 1, the contamination activity must be contained below 5×10^{-5} Bq/ton in the energy window of interest (250-800 keV). Detector design and installation procedures have minimized the unshieldable background of the Borexino medium itself, arising from naturally (e.g. ^{238}U and ^{232}Th), anthropogenic (e.g. ^{85}Kr) and cosmogenic (e.g. ^{14}C and ^{39}Ar) radioactive contaminants. Moreover, the detector is equipped with a purification system designed to purify on-line the scintillator and buffer liquids.

The capability of controlling background is then one of the main issues for the Borex-

ino experiment success. Contamination removal through the purification plants and analysis techniques for the residual background identification (e.g. statistical subtraction, delayed coincidence) are priority for the experiment. The main subject of this thesis is the development and test of purification system and data analysis techniques for the Borexino experiment.

In particular, ^{39}Ar and ^{85}Kr gaseous contaminants can be effectively removed by stripping materials with nitrogen. In order to reach a highly efficient purification, nitrogen itself must be argon and krypton free. We demonstrated (Chapter 3) that carbon-based adsorbers effectively remove ^{85}Kr but are ineffective on ^{39}Ar. At the same time, we measured several commercial nitrogen samples with mass spectrometer and proportional counters, identifying the proper nitrogen which fulfills the Borexino specifications on ^{39}Ar and ^{85}K. Finally, we defined the correct delivery procedure.

The Counting Test Facility (CTF), a Borexino detector prototype, has been opportunely designed to verify experimentally the required radiopurity of the detector materials and to test the efficiencies of the purification systems. The target mass consists of 4 tons of scintillator contained in 2 m diameter nylon sphere and surrounded by a water buffer. In the previous CTF data campaigns, several promising results have been achieved. Among these, the ^{238}U and ^{232}Th intrinsic contaminations were measured consistent with the Borexino requirements (10^{-16} g/g of scintillator).

The last data campaign, still ongoing since three years, has been devoted to measure the initial contamination of the scintillator from trace radioactive isotopes and, specifically, to test the ^{14}C content of the Borexino scintillator delivery. Moreover, CTF evaluated the efficiency of the scintillator purification techniques for Borexino.

Data analysis (Chapter 5) of the delayed coincidences have successfully quantified single isotope activity, even when it was less than 1 event per day (e.g. ^{226}Ra). The statistical analyses (energy and radial), based on an analytical approach, have confirmed some of the coincidence results and allowed the identification of the ^{210}Po contamination, whose high activity was unexpected.

Single nuclide rate measurements have given us the possibility to estimate the efficiencies in purifying single isotopes. When, on the other hand, the purification results were found ambiguous, the analysis has addressed the collaboration to operate toward the correct solution.

In Chapter 6, I present a study on the potential of Borexino in probing neutrinos from the solar CNO chain and *pep* fusion process. For this purpose, the observed energy window has to be extended up to 1.3 MeV, a region dominated by the *in situ* produced cosmogenic ^{11}C. We analyzed all the possible mechanisms which bring to the ^{11}C production and we investigated on the possibility to implement the Martin Deutsch's idea of eliminating the ^{11}C events by looking at the three-fold coincidence with the parent muon track and the subsequent neutron capture on protons.

Finally, in Chapter 7, we applied the three-fold coincidence to the CTF data in order to tag

^{11}C nuclide events by events. The results show a good agreement with the ^{11}C rate predicted by a previous muon beam experiment at CERN and by the FLUKA simulation, confirming the potential of Borexino in ^{11}C removal and thus in probing CNO and *pep* neutrinos.

Acknowledgements

The work I carried out in the last three years would not have been possible without the help and support of so many people that it would be impossible to name them all.

I wish to thank my advisor, Prof. Gianpaolo Bellini, who gave me the opportunity of doing research in neutrino physics. I want also to express great appreciation to my German advisor Prof. Wolfgang Hampel who made possible my stimulating experience at the Max Planck Institut of Heidelberg.

A special thank to Sandra Malvezzi and Stefan Schoenert for their suggestion, support and encouragement not only in physics. Without their time and untiring effort, this endeavor would not have been possible.

I am grateful to the entire Borexino group in Milano - Silvia Bonetti, Emanuela Meroni, Barbara Caccianiga, Marco Giammarchi, Gioacchino Ranucci, Lino Miramonti and Maria Elena Monzani - for their time and assistance. Special thanks to Barbara for her patience, advices and long discussions during these years.

Many tanks also to all the people (not already mentioned) who contributed to this work: Davide D'Angelo, Daniela Manuzio, Marco Pallavicini, Aldo Ianni, Alessandro Razeto, George Korga, Andrea Pocar, Cristian Galbiati, Laura Cadonati, Burkhard Freudiger, Grzegorz Zuzel, Hardy Simgen... too many to be listed here. Thanks also to all the LNGS staff!

Dario: I appreciate your many useful comments on this work, but even more so, I appreciate your advice, comments, and willingness to discuss any questions or ideas that I have had. But also thank you for the funny situations you made me live in Heidelberg.

Ein großes Dankeschön goes to my colleagues and friends at the Max Planck Institut of Heidelberg for all the fun and collaboration: Elisa, Burkhard, Georg, Florian, Christian, Grzegorz, Hardy, Peter and Martin. A special appreciation to Ferenc who spent a lot of time correcting my English.

I can not forget all the people of the III Piano Lita and of the Centro di Calcolo at the University of Milano for providing me with an excellent working atmosphere. In particular Giovanna, Stefano, Massimo, Marco, Lorenzo and Laura who shared with me all the stages from the very beginning of this adventure.

I also want to thank all the friends, near and far, that have been closed to me, especially Lorenza, Luca, Gianluca, Donald, Carlo, Ludovica and Jose'.

A lot of gratitude to Alessandra: I feel very lucky to have your neverending encouragement and thank you for the incredible amount of patience you had with me in the last three months.

I would like to dedicate this thesis to my parents, Bella and Enrico, and to my brother Roberto. They have done all they could and more to get me to this point.

Contents

Chapter 1

Solar Neutrinos and Neutrino Oscillations

The neutrino was hypothesized in the early 1930's by Wolfgang Pauli to uphold energy and momentum conservation in nuclear beta decays. It took more than 20 before Reines and Cowan [1] in 1956 detected anti-neutrinos by monitoring a volume of cadmium chloride with scintillating liquid near to a nuclear reactor.

Neutrinos are known to be tiny and neutral elementary particles in three species or "flavours": electron neutrinos, muon neutrinos, and tau neutrinos. They interact with matter via the weak nuclear force but their interaction cross section is so small that matter is almost transparent to them. It is interesting to observe that the discovery of neutrino is related to a laboratory nuclear physics problem but it is also invoked to explain energy production in our Sun and in all other stars. We now know that nuclear fusion and decay processes, which occur within the stellar core, produce large amounts of neutrinos predicted by reliable "standard" models. Since neutrinos rarely interact with matter, they pass through the Sun and the Earth practically unhindered, carrying precious information about the stellar core composition.

In the last three decades, several solar neutrino experiments observed a deficit in the neutrino flux. The possibility of finding errors in the standard solar model has been investigated at length. However, the current data fits the model (including helioseismology) so well that such errors are highly improbable. The deficit can be explained by a neutrino flavour conversion along the trip from the production point in the Sun to the Earth. This effect is referred as to "neutrino oscillation".

The recent results from solar, atmospheric and reactor neutrino experiments has provided compelling evidence in favour of neutrino oscillations, opening the long-awaited door to physics beyond the Standard Model. Oscillation not only requires that neutrinos have mass, it implies a rich set of parameters and phenomenological behaviour. Numerous experiments have gradually constrained these parameters, zooming in on the correct oscillation behaviour.

1.1 The Solar Model

Until the late 1800's, the most accredited hypotheses explaining the source of the stellar energy were based on chemical reactions and gravitational contraction in the stars. Nevertheless, the energy that can be produced through these processes is not enough to account for the observed solar luminosity, integrated over its age, and estimated through geological considerations.

It was Hans Bethe (1939) who first realized that the weak nuclear interaction was capable of converting a proton into a neutron during the brief encounter of a p+p scattering event.

H. Bethe and C. H. Critchfield (1938) [2] presented the details of the full proton-proton (pp) chain of reactions (Figure 1.1) that convert hydrogen to helium and allow the Sun to shine for about 10 billion years. The overall reaction balance can be represented by:

$$4p \rightarrow \alpha + 2e^{+} + 2\nu_e. \tag{1.1}$$

with a mass excess of 24.7 MeV plus 2 MeV from the annihilation of e^{+}'s. The pp-chain is now known to contribute about 98% of the Sun's energy production in its inner core. The remainder is contributed by the carbon-nitrogen-oxygen (CNO) cycle, which was independently discovered by C. F. von Weizsäcker (1938) [3] and H. Bethe (1939) [4]. The details of the nuclear reactions in the pp and CNO cycles are summarized in Tables 1.1 and 1.2.

Solar processes are difficult to be tested since the region in which thermonuclear fusion is assumed to take place is the Sun's core and it is hidden by thick layers of cooler material. Among the particles released by these reactions, only the neutrino can escape the surface of Sun. The study of solar neutrinos is therefore the only direct way we have, at present, to study the processes by which the Sun (and other stars) shine.

Since the pp reaction is at the base of the pp chain, the pp neutrino flux is connected directly to the Sun luminosity, but for all the other neutrino sources detailed models describing the conditions inside the Sun are necessary.

The Solar Models are essentially solutions of the stellar evolution equations using the known properties of luminosity, mass, radius and age as boundary conditions and cross sections for nuclear reactions, element abundances and radiative absorption coefficients as input data. Since the oblateness is very small, the Sun is assumed to be spherical. The models basically assume that the gravitational contraction is balanced by the radiative pressure from thermonuclear reactions. Further, the energy is transported only by convection and radiation from the core of the Sun to the surface.

The evolution equation, solved iteratively starting from the initial main sequence (also called zero-age main-sequence, ZAMS), then outputs radial distributions of temperature, density and pressure, the composition of the Photosphere (the outer layer of the Sun), the frequency spectrum for acoustic oscillations of the Sun's surface and the solar neutrino spectra and fluxes.

Reaction		Branching ratio (%)	Q [MeV]	Eν [MeV]	$\langle q_\nu \rangle$ [MeV]
$p + p \rightarrow {}^2H + e^+ + \nu_e$	(pp)	99.77	1.442	$\leq$0.420	0.265
$p + e^- + p \rightarrow {}^2H + \nu_e$	(pep)	0.23	1.442	1.442	1.442
${}^2H + p \rightarrow {}^3He + \gamma$		100	5.494		
${}^3He + {}^3He \rightarrow \alpha + 2p$		84.92	12.860		
${}^3He + p \rightarrow {}^4He + e^+ + \nu_e$	(hep)	10^{-5}	19.795	$\leq$18.8	9.27
${}^3He + {}^4He \rightarrow {}^7Be + \gamma$		15.08	1.586		
${}^7Be + e^- \rightarrow {}^7Li + \nu_e$	$({}^7Be)$	15.07	0.862 (90%)	0.862	0.862
			0.383 (10%)	0.383	0.383
${}^7Li + p \rightarrow 2\alpha$		15.07	17.347		
${}^7Be + p \rightarrow {}^8B + \gamma$		0.01	0.137		
${}^8B \rightarrow {}^8Be^* + e^+ + \nu_e$	$({}^8B)$	0.01	17.980	$\leq$15	6.71
${}^8Be^* \rightarrow {}^4He + {}^4He$		0.01			

Table 1.1: The proton-proton (pp) cycle of nuclear fusion reactions in the Sun. There are five ν-emitting reactions in this cycle.

Reaction		Q [MeV]	Eν [MeV]	$\langle q_\nu \rangle$ [MeV]
${}^{12}C + p \rightarrow {}^{13}N + \gamma$		1.943		
${}^{13}N \rightarrow {}^{13}C + e^+ + \nu_e$	$({}^{13}N)$	2.221	$\leq$ 1.199	0.7067
${}^{13}C + p \rightarrow {}^{14}N + \gamma$		7.551		
${}^{14}N + p \rightarrow {}^{15}O + \gamma$		7.297		
${}^{15}O \rightarrow {}^{15}N + e^+ + \nu_e$	$({}^{15}O)$	2.754	$\leq$ 1.732	0.9965
${}^{15}N + p \rightarrow {}^{12}C + \alpha$		4.966		
or				
${}^{15}N + p \rightarrow {}^{16}O + \gamma$		12.128		
${}^{16}O + p \rightarrow {}^{17}F + \gamma$		0.600		
${}^{17}F \rightarrow {}^{17}O + e^+ + \nu_e$	$({}^{17}F)$	2.762	$\leq$ 1.740	0.9994
${}^{17}O + p \rightarrow {}^{14}N + \alpha$				

Table 1.2: The SSM predicts 1.5% of the energy from the Sun comes from the CNO cycle. Three neutrinos are emitted from this source.

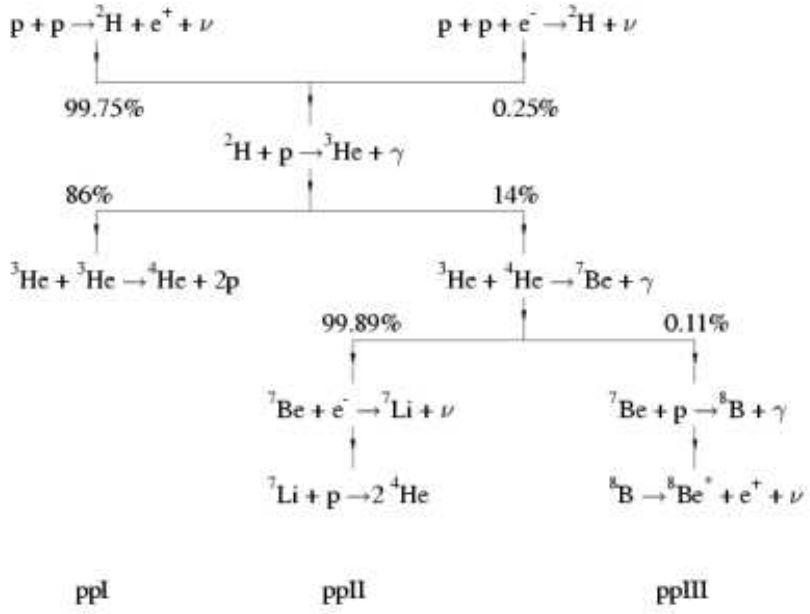

Figure 1.1: The proton-proton (pp) cycle of nuclear fusion reactions in the Sun. The % values indicated are the branching ratio of each reaction.

Solar Models can be also tested by comparing their predictions for the sound speed inside the Sun with the radial distributions calculated from the helioseismic activity precision observations made by several experiments [25]. The agreement between the measurements and the predictions of the BP2000 [7] model is at the level of 0.1 % rms (Figure 1.2). Hereafter, we will consider the model recently published by Bahcall and Pinsonneault as the Standard Solar Model (SSM), referred as BP2004 [8].

The fluxes of each individual source listed in Table 1.3 are predicted by the BP2004 model combined with the recent result from the Laboratory Underground Nuclear Astrophysics experiment (LUNA) [9] that measured the ^{14}N(p,γ)^{15}O fusion reaction. The energy spectra corresponding to the solar neutrino fluxes are shown in Figure 1.3.

Source	Flux $[10^{10} cm^{-2} s^{-1}]$
pp	5.98 (1 ± 0.01)
pep	1.42 (1 ± 0.02) x 10^{-2}
hep	7.93 (1 ± 0.16) x 10^{-7}
^{7}Be	4.86 (1 ± 0.12) x 10^{-1}
^{8}B	5.77 (1 ± 0.23) x 10^{-4}
^{13}N	3.23 $(1\ ^{+0.37}_{-0.35})$ x 10^{-2}
^{15}O	2.54 $(1\ ^{+0.43}_{-0.39})$ x 10^{-2}
^{17}F	5.85$(1\ ^{+0.44}_{-0.44})$ x 10^{-2}

Table 1.3: Solar neutrino fluxes assuming BP2004 [8] plus the recent result on the ^{14}N+p fusion reaction from LUNA [9]. The correspondent capture rates in chlorine and gallium solar experiments are 8.2±1.8 and 127^{+12}_{-10} SNU, respectively (1 SNU = 10^{-36} events per target atom per second).

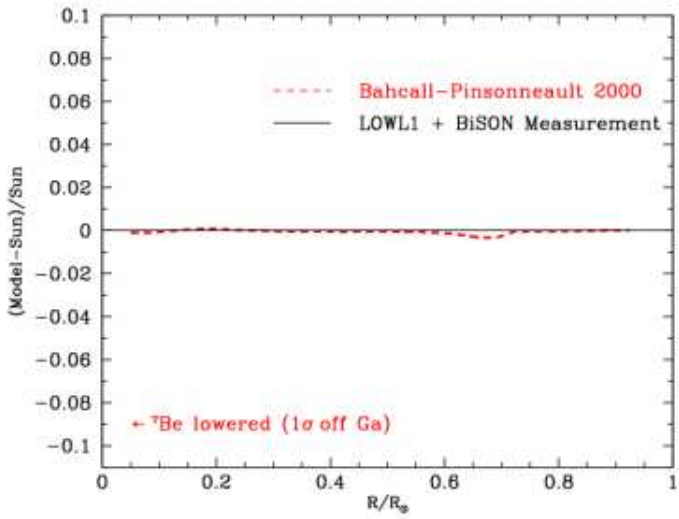

Figure 1.2: Predicted versus measured sound speeds in the Sun. The figure highlights the excellent agreement between the sound speeds predicted (red) by the standard solar model (BP00 [7]) and the helioseismologically measurements (black). The ν flux deficit observed in the gallium solar neutrino experiments can not be explained by changing the input parameters in the standard solar model. The arrow, indeed, indicates the distance of the BP00 from the helioseismological measurements forcing the model to explain the deficit.

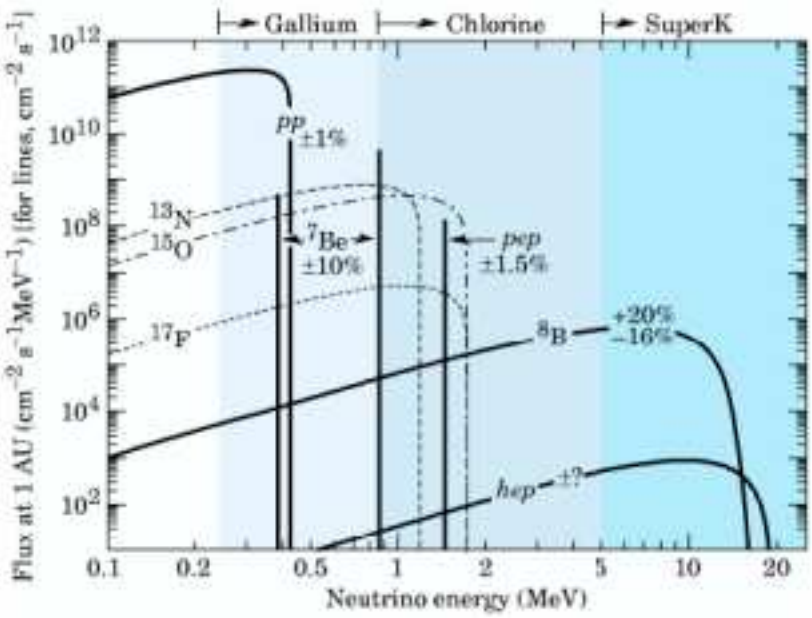

Figure 1.3: Energy spectrum of the pp and CNO chain solar neutrinos according to the BP2000 solar model.

1.2 Solar neutrino experiments

The difficulties of solar neutrino experiment are connected to the very low neutrino cross sections of interaction with matter. The typical requirements are large detector volume, high detection sensitivity, low background environments and deep underground location to shield the detectors from cosmic rays. At present, only six experiments have detected solar neutrinos and they can be classified in two types:

- Radiochemical measurements based on neutrino capture reactions by specific isotopes. The reaction products are then chemically separated from the target mass and counted through low background proportional chambers. This technique is sensitive to the total capture rate above a certain threshold but does not convey any information on the neutrino energy spectrum.

- Real time experiments which detect Cerenkov light from reactions involving elastic scattering of neutrinos from electrons, the inverse beta decay reaction on deuterium emitting energetic electrons and inelastic scattering on deuterium producing free neutrons. Such experiments supply information about the energy, time and direction of neutrino interactions.

In this section, I will briefly describe the experiments and the achieved results.

Solar neutrinos were first detected in 1968 by the pioneering ^{37}Cl experiment of Raymond Davis in the Homestake gold mine in Lead, South Dakota [10]. The detector was based on a concept first proposed by Bruno Pontecorvo at Chalk River Laboratory in Canada in 1946 [11], in which neutrino reactions on chlorine are measured. Neutrinos striking chlorine can make an isotope of argon through the reaction

$$\nu_e + {}^{37}Cl \rightarrow e^- + {}^{37}Ar \tag{1.2}$$

with an energy threshold of 0.814 MeV (sensitive mainly to ^{7}Be, ^{8}B, and CNO neutrinos, see Tables 1.1 and 1.2).

The detector was sited at a water equivalent depth of 4200 m and consisted of a 390 m^3 tank of C_2Cl_4. ^{37}Ar atoms were extracted periodically every couple of months. Small proportional chambers measured the 2-3 keV Auger electrons emitted by the ^{37}Ar electron capture decay ($\tau_{1/2} \sim 35$ days).

The experiment successfully detects a solar neutrinos rate, averaged on the 25 years of data taking (1970-1995), of:

$$R_{Homestake} = 2.56 \pm 0.16\,(stat.) \pm 0.16\,(syst.)\,SNU \tag{1.3}$$

The measured rate (from BP2004+LUNA [8, 9]) is only one-third of the predicted value:

$$R_{predicted} = 8.2 \pm 1.8\,SNU. \tag{1.4}$$

A deficit was observed also by the other three radiochemical experiments, SAGE [12], GALLEX [13] and GNO [14] which detect neutrinos via the electron capture reaction on ^{71}Ga:

$$\nu_e + {}^{71}Ga \rightarrow e^- + {}^{71}Ge \tag{1.5}$$

The low energy threshold at 0.233 MeV makes the gallium experiments the only ones able to detect solar neutrinos also from the *pp* reaction. The produced ^{71}Ge atoms decay via electron capture in $\tau_{1/2} \sim 11.5$ days and are detected by low background proportional chambers.

SAGE, located at the Baksan Neutrino Observatory in the Northern Caucasus (Russia) used a target of 50 tons of solid gallium, shielded by 4700 m of water equivalent. GALLEX is located in the Gran Sasso underground laboratory in Italy at the depth of 3800 mwe. The sensitive target mass consists of 30 tons of gallium in form of liquid $GaCl_3$ solution. GNO is an upgrade of the GALLEX detector up to 100 tons of target mass.

The measured capture rates, after approximately 10 years of running,

$$R_{SAGE} = 67.2^{+7.2}_{-7.0}\,(stat.)\,^{+3.5}_{-3.0}\,(syst.)\,SNU \tag{1.6}$$

$$R_{GALLEX} = 77.5 \pm 6.2(stat.)\,^{+4.3}_{-4.7}\,(syst.)\,SNU \tag{1.7}$$

$$R_{GNO} = 65.8^{+10.2}_{-9.6}\,(stat.)\,^{+3.4}_{-3.6}\,(syst.)\,SNU \tag{1.8}$$

are significantly below (54%) the BP2004+LUNA predictions,

$$R_{predicted} = 131 \pm 11\,SNU \tag{1.9}$$

confirming the depletion scenario seen by the Chlorine experiment.

Kamiokande [15, 16] and its successor experiment, SuperKamiokande [17], were built in the Kamioka mine in Japan (2600 mwe). They are light water neutrino detectors with 680 ton and 22.5 kiloton fiducial mass, respectively. Solar neutrinos are observed through the elastic scattering of neutrinos from electrons,

$$\nu + e^- \rightarrow \nu + e^- \tag{1.10}$$

detecting the Cerenkov light from the recoiling electron with $\sim$ 1000 photomultiplier tubes in Kamiokande and $\sim$ 11000 in SuperKamiokande.

This technique has the advantage to be sensitive, event-by-event, to all the neutrino flavours. The directionality of the Cerenkov light provides direct evidence of the solar origin of the neutrino. Furthermore, it supply information on the neutrino energy spectrum and on the neutrino flux time variations by recording the time of each event. On the other hand, the background imposes high energy thresholds (7.5 MeV for Kamiokande and 5 for SuperKamiokande) making both experiments sensitive only to ^{8}B and *hep* neutrinos.

In almost a decade of data taking, Kamiokande observed a solar neutrino flux from ^{8}B equal to [16]:

$$\Phi_{Kamiokande} = 2.80 \pm 0.16\,(stat.) \pm 0.16\,(syst.) \times 10^6 cm^{-2} s^{-1}. \tag{1.11}$$

Mainly due to its higher mass, SuperKamiokande greatly increased the precision of this measurement:

$$\Phi_{SuperKamiokande} = 2.32 \pm 0.03\,(stat.)\,^{+0.08}_{-0.07}\,(syst.) \times 10^6 cm^{-2} s^{-1} \tag{1.12}$$

which corresponds to a deficit respect to the predicted value of (see Table 1.3):

$$\Phi_{SuperKamiokande}/\Phi_{BP2004} = 0.465 \pm 0.015. \tag{1.13}$$

SuperKamiokande is also sensitive to the shape of the ^{8}B signal energy spectrum. The measured spectrum is consistent with the ^{8}B neutrino spectrum as predicted by the SSM, with no energy-dependent distortions. The seasonal variation of the flux is also consistent with that expected from the eccentricity of the Earth's orbit. However, there is a discrepancy between the flux measured during the day and during the night:

$$\frac{\Phi_n - \Phi_d}{\Phi_n + \Phi_d} = 0.033 \pm 0.022\,(stat.)\,^{+0.013}_{-0.012}\,(syst.). \tag{1.14}$$

showing a weak departure from 0 at about 1.3 σ.

The Subdury Neutrino Observatory (SNO) [18] is sited 2000 m underground (6200 mwe) near Subdury, Ontario, Canada. The target mass of 1100 tons of heavy water is contained by a spherical acrylic vessel and shielded by a volume of light water. Surrounding the acrylic vessel is a geodesic structure supporting 9500 photomultiplier tubes.

The use of heavy water in SNO allows the detection of neutrinos with energies > 6.75 MeV via capture on deuterium nuclei in addition to the neutrino-electron elastic scattering:

$$\begin{aligned} \nu_e + d \rightarrow p + p + e^- \quad & (Charged\ Current:\ CC) \\ \nu_x + e^- \rightarrow \nu_x + e^- \quad & (Elastic\ Scattering:\ ES) \\ \nu_x + d \rightarrow p + n + e^- \quad & (Neutral\ Current:\ NC). \end{aligned} \tag{1.15}$$

In the above reactions, the Cerenkov light emitted by the recoil electrons in the CC and ES reactions are observed by the PMT's. For the NC reaction, the free neutron is thermalized and capture by protons yielding γ-ray. Its electron shower is detected by Cerenkov effect.

The CC reaction is sensitive exclusively to the ν_e component of the ^{8}B flux while the NC cross section is independent on the neutrino flavour providing information of the total ^{8}B flux. Also, the ES reaction is sensitive to all neutrino flavours even though the ν_e-e$^-$ cross section dominates $\nu_{\mu,\tau}$-e$^-$ by a factor ~ 6.5.

To enhance sensitivity to the NC reaction, two methods have been planned: neutron capture on ^{35}Cl in NaCl added to the heavy water, producing 8.6 MeV γ-rays (already implemented) and ^{3}He filled proportional counters placed inside the vessel (actually the installation is on progress).

In September 2003, the SNO collaboration reported the last results using the NC reaction measurement. The entire first phase data set (November 1999 - May 2001), without salt, was re-analyzed with a lower energy threshold (5 MeV). The measured ^{8}B fluxes for each reaction

are [19, 20, 21]:

$$\begin{aligned}
\Phi_{CC}^{SNO} &= 1.59 \pm {}^{+0.08}_{-0.07}\,(stat.) \pm {}^{+0.06}_{-0.08}\,(syst.) \times 10^6 cm^{-2}s^{-1} \\
\Phi_{ES}^{SNO} &= 2.21 \pm {}^{+0.31}_{-0.26}\,(stat.) \pm 0.10\,(syst.) \times 10^6 cm^{-2}s^{-1} \\
\Phi_{NC}^{SNO} &= 5.21 \pm 0.27\,(stat.) \pm 0.38\,(syst.) \times 10^6 cm^{-2}s^{-1}.
\end{aligned} \tag{1.16}$$

It is interesting to observe the agreement between the ES reaction results in SNO and SuperKamiokande (Eq 1.12) which confirms the deficit with respect to the BP2004 prediction. At the same time, the NC result agrees with the SSM prediction (Table 1.3) within 1σ uncertainty:

$$\Phi(^8B)_{measured} = (0.88 \pm 0.04\,(stat.) \pm 0.11\,(syst.)) \times \Phi(^8B)_{theory}. \tag{1.17}$$

It appears clear, from the results listed in Eq 1.16, that only one third of the solar neutrino flux from ^{8}B above 5 MeV has electronic flavour.

1.3 The solar neutrino problem

The essence of the solar neutrino problem is the experimental detection of two to three times fewer solar neutrinos than predicted by the Standard Solar Model. Since the Chlorine experiment, more than 20 years ago, this represented the only solar neutrino problem. The data accumulation from the following experiments confirmed the inconsistence as is clearly shown in Figure 1.4, where the measured rates (blue) are directly compared to the predicted ones for each solar neutrino source (coded with different colours).

In 1990, J. N. Bahcall and H. Bethe [23] pointed out a second neutrino problem, comparing the measured rates from Kamiokande and Chlorine experiments. The Chlorine experiment had a low energy threshold of 814 keV, whereas the Kamiokande experiment, due to significant quantities of radon dissolved in the water, had a low energy threshold of 7.5 MeV. Most of the neutrinos detected were therefore produced from the ^{8}B source. Normalizing and subtracting the Kamiokande rate from the Chlorine one, there is no space for *pep*, CNO and ^{7}Be neutrinos, whose rate is found to be negative: -0.22 ± 0.10 SNU.

The results from the Gallium experiments, SAGE, GALLEX and GNO, constitutes the third solar neutrino problem. The measured rate in the Gallium experiments is all accounted by the *pp* neutrinos, leaving no space for the large expected contribution from ^{7}Be neutrinos. The inconsistency lies in the fact that, in the Sun, ^{7}Be is the only conceivable source of ^{8}B, which is clearly observed in the water Cerenkov detectors. This problem, usually referred as the missing ^{7}Be neutrinos problem, differs from the previously discussed solar neutrino problems because strongly depends upon the *pp* neutrinos. Their flux is closely related to the total luminosity of the Sun and therefore approximately independent of the Solar Model.

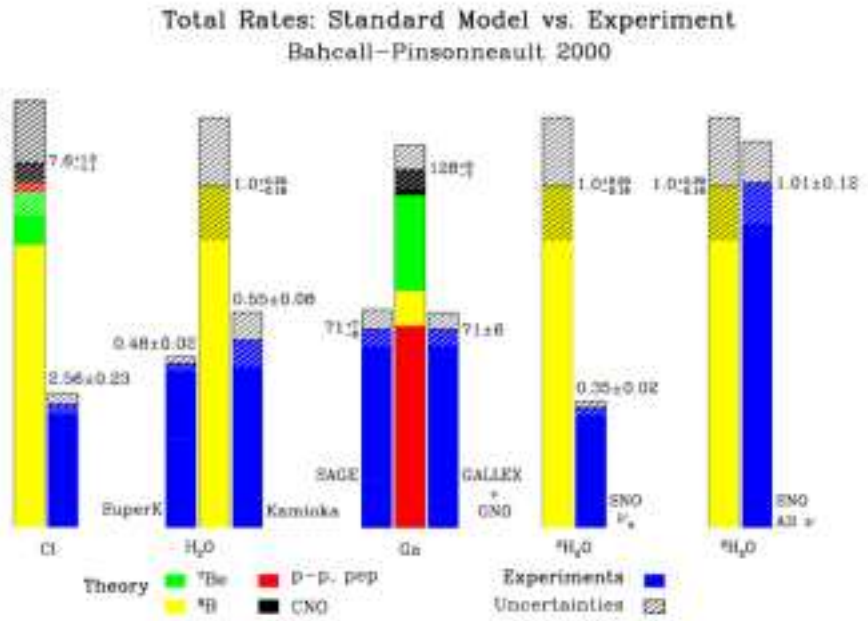

Figure 1.4: Comparison of the Standard Solar Model predictions with the total rates in the six solar neutrino experiments [24].

Many "non-standard" astrophysical solutions have been proposed in order to solve the solar neutrino problem, where "non-standard" indicates the use of different assumptions in the stellar evolution equations or *ad hoc* input parameters in order to predict a lower neutrino capture rate. A strong constraint on the validity of Solar Models, indeed, is given by the total neutrino flux. A specific linear combination of the neutrino fluxes must be proportional to the solar luminosity:

$$\frac{L_\odot}{4\pi\,(AU)^2} = \sum_i \alpha_i \phi_i \tag{1.18}$$

where $L_\odot$ is the solar luminosity measured at the Earth's surface and 1 AU is the average Earth-Sun distance. The coefficient α_i is the amount of energy provided to the star by nuclear fusion reactions associated with each of the main solar neutrino fluxes, ϕ_i [6].

The main idea at the base of the non-standard Solar Models is to lower the central temperature of the Sun by a few percent. This will mean fewer high-energy nuclear reactions occurring in the Solar core and thus fewer neutrinos being produced and detected. There are a number of ways to lower the central solar temperature. Mixing will cause fresh fuel to be brought into the core, and thus a lower temperature will be needed to maintain equilibrium. Rotation, convection, or other instabilities could cause mixing in the core. Other more exotic

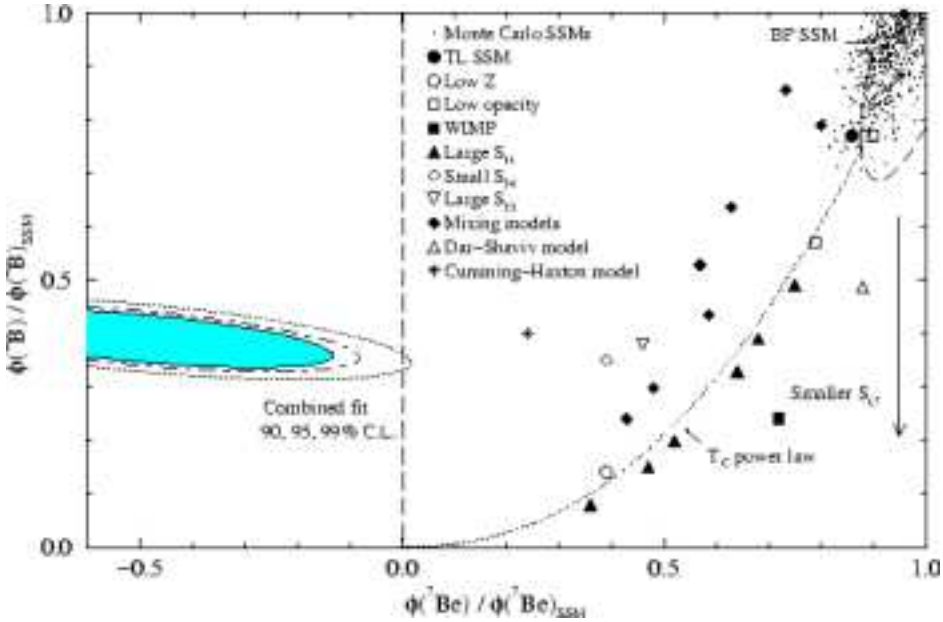

Figure 1.5: Predicted fluxes of ^{8}B and ^{7}Be neutrinos for several non-standard solar models, compared to the allowed region by a combined fit of the experimental measurements. The best fit would lead to the non-physical region of negative ^{7}Be neutrino flux [24].

solutions rely changing the metallicity of the core (that is, changing the relative abundances of the heavy elements) and using WIMPs (Weakly Interactive Massive Particles), that would replace neutrinos as carriers for part of the Sun's energy.

A summary of the predictions for the ^{8}B and ^{7}Be neutrino fluxes by non-standard solar models is shown in Figure 1.5. While some models predict a ^{8}B flux near to the measured value, none of them are capable of explaining the strong suppression of the ^{7}Be neutrinos, inferred from a combined fit of all the experimental data.

Moreover, as already discussed in Section 1.1, helioseismological results favours the Standard Solar Model (at the level of 0.1% rms) and strongly suppresses non-standard astrophysical solutions. As shown in Figure 1.2, the arrow at the bottom indicates that the distance of the Standard Solar Model from the helioseismological measurements is off by at least 9% rms when the model is forced to explain the deficit [25].

If astrophysical solutions are unadapted to solve the solar neutrino problem, an alternative way lies beyond the minimal standard electroweak model. The SNO results directly suggest that an energy dependent conversion of the neutrino flavours occurs on their way from the Sun to the Earth. This effect is known as "neutrino oscillations".

1.4 Neutrino oscillations

The idea of neutrino oscillation was first introduced by Bruno Pontecorvo [26] in 1958 for neutrino and antineutrino system. The oscillation between weak (flavour) eigenstates was considered by Maki et al. (1962) [27] and Pontecorvo [28] (1967). If at least one neutrino is massive, in general the mass eigenstates and flavour eigenstates may not coincide but they are related by a unitary transformation similar to the Cabibbo-Kobayashi-Maskawa (CKM) mixing matrix in the quark sector.

In 1978, Wolfenstein [31] observed that *"the effect of coherent forward scattering must be taken into account when considering the oscillations of neutrinos travelling through matter"*. He discovered that if there exists an interaction through which neutrinos can change flavour, the conversion can be enhanced when travelling through matter. In 1985, Mikheyev and Smirnov [29, 30], argued that for specific oscillation and matter density parameters, this enhancement could develop a resonance behaviour. This mechanism, known as the MSW effect, produces large ν_e suppressions even with small mixing and in a vast parameter region and it is now widely considered as the most likely solution to the solar neutrino problem.

1.4.1 Oscillations in vacuum

Since the flavour $|\nu_\alpha\rangle$ (α = e, μ, τ) and the mass $|\nu_i\rangle$ (i = 1,2,3) eigenstates are orthogonal basis of the general neutrino state, they are related by a 3x3 unitary matrix:

$$|\nu_\alpha\rangle = \sum_i U_{\alpha,i} \, |\nu_i\rangle \tag{1.19}$$

where $U_{\alpha,i}$ is the leptonic mixing matrix also called the MNS (Maki-Nakagawa-Sakata) matrix.

Hereafter I will consider the simplest case of the transition between two types of neutrinos. In this scenario the flavour and the mass basis are related by a single parameter, the mixing angle θ:

$$\begin{aligned} |\nu_e\rangle &= cos\theta \, |\nu_1\rangle + sin\theta \, |\nu_2\rangle \\ |\nu_x\rangle &= -sin\theta \, |\nu_1\rangle + cos\theta \, |\nu_2\rangle \, . \end{aligned} \tag{1.20}$$

where θ is the mixing angle. An electron neutrino $|\nu_e\rangle$ produced at time t 0 with momentum p will propagate as the superposition of the two mass eigenstates:

$$|\nu_e(\overrightarrow{x}, t)\rangle = cos\theta \, |\nu_1\rangle \, e^{-i\,(E_1 t - \overrightarrow{p}\cdot\overrightarrow{x})} + sin\theta \, |\nu_2\rangle \, e^{-i\,(E_2 t - \overrightarrow{p}\cdot\overrightarrow{x})}. \tag{1.21}$$

Under the assumption that the masses are small and neutrinos relativistic, $m << p$ and the energy of the mass states can be rewritten as $E_j = \sqrt{\overrightarrow{p}^{\,2} + m^2} \simeq p + \frac{m_j^2}{2p}$ ($|\overrightarrow{p}| \equiv p$) for mass

states with momentum $p \simeq E$. Defining $\Delta m^2 = m_1^2 - m_2^2$, the neutrino transition probabilities to observe an electronic or a muon neutrino at time t are:

$$\begin{aligned} P(\nu_e \to \nu_x; E, t) &= |\langle \nu_\mu | \nu_e(t) \rangle|^2 = sin^2 2\theta \, sin^2 \frac{\Delta m^2}{4E} t \\ P(\nu_e \to \nu_e; E, t) &= |\langle \nu_e | \nu_e(t) \rangle|^2 = 1 - sin^2 2\theta \, sin^2 \frac{\Delta m^2}{4E} t. \end{aligned} \tag{1.22}$$

Introducing the *vacuum oscillation length*:

$$L_\nu = \frac{4\,\pi\,E}{\Delta m^2} \tag{1.23}$$

in Eq 1.22, the transition probabilities become:

$$\begin{aligned} P(\nu_e \to \nu_x; E, t) &= sin^2 2\theta \, sin^2 \frac{\pi\,R}{L_\nu} \\ P(\nu_e \to \nu_e; E, t) &= 1 - sin^2 2\theta \, sin^2 \frac{\pi\,R}{L_\nu} \end{aligned} \tag{1.24}$$

where R is the source-detector distance. The transition probability has then an oscillating behaviour where the $sin^2 2\theta$ is the amplitude parameter and the phase a function of the mass-square difference, Δm^2, and of the distance R. The parameter space ($sin^2 2\theta$,Δm^2) can be tested by varying the energy and the distance of the neutrino source. If $R \ll L_\nu$, the phase varies too slowly and the transition probability is not appreciable. When the frequency is very high, $R \gg L_\nu$, the transition probability undergoes fast oscillations. Averaging over small energy intervals corresponding to a finite resolution of the detector or over small variations of the source-detector distance, the observed probability becomes $\frac{1}{2} sin^2 2\theta$.

1.4.2 Oscillations in matter

Matter can enhance neutrino mixing and the probabilities of neutrino oscillations in matter can be large even if the mixing angle in vacuum is small. The propagation of neutrinos in matter is affected by coherent forward scattering through the weak interaction. Z^0-exchange processes (NC) are the same for ν_e, ν_μ and ν_τ generating a common phase that can be neglected. On the other hand, $W^\pm$-exchange (CC) contributes only to ν_e scattering and significantly changes the propagation equation. Coherent interactions generate an additional effective potential energy [32]:

$$V_{CC} = \frac{g^2}{M_W^2} N_e \simeq \sqrt{2} N_e G_F \tag{1.25}$$

where N_e is the electron density, g the weak interaction coupling, M_W the W-boson mass and G_F is the Fermi constant. This potential leads to an extra term in the neutrino oscillation

Hamiltonian, whose diagonalization leads to effective squared mass differences and mixing angles in matter ($sin^2 2\theta_m$,Δm_m^2) which are, in general, different from the vacuum values ($sin^2 2\theta$,Δm^2). Since the energy and momentum of ν_e are related by:

$$p^2 + m^2 = (E - V)^2 - V^2 \simeq E^2 - 2\,E\,V, \tag{1.26}$$

neglecting the small term V^2, the extra term in the Hamiltonian is $2\sqrt{2}N_e G_F E$.

The vacuum mass matrix in the basis of ν_e and ν_x is expressed by:

$$M^2_{vacuum} = \frac{1}{2}\begin{bmatrix} m_1^2 + m_2^2 & 0 \\ 0 & m_1^2 + m_2^2 \end{bmatrix} + \frac{1}{2}\Delta m^2 \begin{bmatrix} -cos2\theta & sin2\theta \\ sin2\theta & cos2\theta \end{bmatrix} \tag{1.27}$$

Adding the extra term, the Hamiltonian then becomes:

$$i\frac{d}{dt}\begin{pmatrix} \nu_e \\ \nu_x \end{pmatrix} = -\frac{M^2_{matter}}{2E}\begin{pmatrix} \nu_e \\ \nu_x \end{pmatrix} \tag{1.28}$$

where

$$M^2_{matter} = \frac{1}{2}\begin{bmatrix} m_1^2 + m_2^2 - \Delta m^2 cos2\theta + 4\sqrt{2}N_e G_F E & \Delta m^2 sin2\theta \\ \Delta m^2 sin2\theta & m_1^2 + m_2^2 + \Delta m^2 cos2\theta \end{bmatrix}. \tag{1.29}$$

Diagonalization of the Hamiltonian in Eq 1.28 gives the following neutrino eigenstates ("heavy" and "light") in matter:

$$\begin{aligned} |\nu_H\rangle &= cos\theta_m\,|\nu_e\rangle + sin\theta_m\,|\nu_x\rangle \\ |\nu_L\rangle &= -sin\theta_m\,|\nu_e\rangle + cos\theta_m\,|\nu_x\rangle\,. \end{aligned} \tag{1.30}$$

and eigenvalues:

$$m^2_{m_{(H,L)}} = \frac{1}{2}(m_1^2 + m_2^2 + 2\sqrt{2}G_F N_e E) \pm \frac{1}{2}\Delta m^2 \frac{sin2\theta}{sin2\theta_m} \tag{1.31}$$

The mixing angle in matter θ_m , given by:

$$sin2\theta_m = \frac{\Delta m^2 sin2\theta}{\sqrt{(2\sqrt{2}G_F N_e E - \Delta m^2 cos2\theta)^2 + (\Delta m^2 sin2\theta)^2}}. \tag{1.32}$$

is different from the vacuum mixing angle θ and therefore the matter eigenstates $|\nu_A\rangle$ and $|\nu_B\rangle$ do not coincide with the mass eigenstates $|\nu_1\rangle$ and $|\nu_2\rangle$. The oscillation length in matter

L_m is then defined by:

$$L_m = \frac{2\pi}{|E_H - E_L|} = \frac{4\pi E}{\sqrt{(2\sqrt{2}G_F N_e E - \Delta m^2 cos2\theta)^2 + (\Delta m^2 sin2\theta)^2}} \tag{1.33}$$

where E_H and E_L are the eigenenergies in matter. The probability of $\nu_e \longleftrightarrow \nu_x$ oscillations in matter

$$P(\nu_e \rightarrow \nu_x; L) = sin^2 2\theta_m sin^2\left(\frac{\pi R}{L_m}\right) \tag{1.34}$$

has exactly the same form as the probability of oscillations in vacuum (Eq 1.24), except that the vacuum mixing angle θ and oscillating length L_v are replaced by those in matter, θ_m and L_m.

The oscillation amplitude in Eq 1.32 has a typical resonance form, with the maximum values $sin^2 2\theta_m = 1$ in

$$N_{e,res} = \frac{\Delta m^2}{2E}\frac{cos2\theta}{\sqrt{2}G_F} \tag{1.35}$$

called the MSW resonance condition. From Eq 1.32, it follows that when the MSW resonance is fulfilled, mixing in matter is maximal ($\theta_m = 45°$) for any non-zero vacuum mixing angle. As a consequence, if neutrinos cross a region with a sufficiently high N_e, there is a large probability that a flavour conversion occurs.

In the Sun, ν_e's are produced at high density and then propagated to the vacuum where they are measured. One makes the usual assumption that, in vacuum, ν_e is almost identical to the light mass eigenstate ν_L an $\nu_\mu \sim \nu_H$. But as the density $N_e(r)$ increases, the matter effects make ν_e heavier than ν_μ. If the evolution is adiabatic, i.e. $N_e(r)$ changes slowly, the survival probability depends only on the initial and final density but not on the details of the density profile. A neutrino produced as a ν_e in the core of the Sun, crossing the resonance electron density $N_{e,res}$, must therefore exit the Sun as the heavier vacuum eigenstate, $\nu_e \rightarrow \nu_H(r)$. This mechanism implies a complete conversion $\nu_e \rightarrow \nu_\mu$ producing a flux that cannot be detected via charged current.

1.5 Evidence in favour of oscillations

1.5.1 Global analysis of the solar neutrino data

Solar neutrino results from Homestake, Kamiokande, SAGE, GALLEX, GNO and Super-Kamiokande, reported in Section 1.2, conflicts with the Standard Solar Model predictions, indicating a disappearance of solar electron neutrinos on their way from the Sun to the Earth. The real breakthrough in the solution of the Solar Neutrino Problem was due to the SNO experiment. The SNO results for the first time, provided a direct evidence (model independent)

of the presence of non-electron active neutrino component in the solar neutrino flux. Using the neutral current, elastic scattering and charged current reactions and assuming the ^{8}B neutrino shape predicted by the SSM, it is possible to derive the electron and active non-electron neutrino components of the solar flux at high energies (>5 MeV), as shown in Figure 1.6. The non-electron component, found to be $\sim 5\sigma$ greater than zero, represents the strongest evidence of the flavour oscillation in the neutral lepton sector. Moreover, the neutral current measurement is in good agreement with the prediction of the total neutrino flux, confirming the validity of the SSM.

The impact of these measurements restricts the mixing parameter space to mainly two allowed regions: the strongly favored solution, the so-called Large Mixing Angle (LMA) [33], with parameters $\Delta m^2 \sim (7-9)\cdot 10^{-5} eV^2$ and $tan^2\theta \sim 0.35 - 0.45$, shown in the top of Figure 1.7, the low mass (LOW) and (Quasi) Vacuum solutions at lower Δm^2.

1.5.2 Reactor experiment: the KamLAND results

KamLAND (Kamioka Liquid scintillator Anti-Neutrino Detector) [34] is a long baseline neutrino oscillation experiment studying the oscillation of $\overline{\nu}_e$'s emitted from power reactors. The underground detector site, in the Kamioka mine, Japan (2700 mwe of depth), is conveniently located among 53 nuclear power plants ranging in distance of 120-210 km from the detector. The $\overline{\nu}_e$ flux is well determined from the power spectra and the burn-up rates provided by the power stations with a precision of $\sim$ 3%. The low energy of the reactor $\overline{\nu}_e$'s ($\sim$ MeV) makes them ideal for exploring oscillations with small mass differences and relatively large mixing angles. The comparison between measured and predicted rates allows to quantify the reactor anti-neutrino disappearance, providing a direct determination of the flavour oscillation parameters.

KamLAND is a 1 kton pure liquid scintillator detector housed in a 13 m diameter spherical vessel and monitored by 1879 photomultiplier tubes. A 3.2 kton water Cerenkov detector surrounds the containment sphere, absorbing γ-rays and neutrons from the enclosing rock and tagging cosmic-ray muons.

$\overline{\nu}_e$'s are detected via charged current reaction through the inverse β-decay:

$$\overline{\nu}_e + p \rightarrow e^+ + n \tag{1.36}$$

with a low energy threshold of 1.8 MeV. The $\overline{\nu}_e$ identification is based on the delayed coincidence between e^+ and the 2.2 MeV γ from the neutron capture on protons.

At the end of 2002, the KamLAND collaboration published the first results [35] where the ratio between the number of observed $\overline{\nu}_e$ events and the predicted one in absence of neutrino oscillations is equal to :

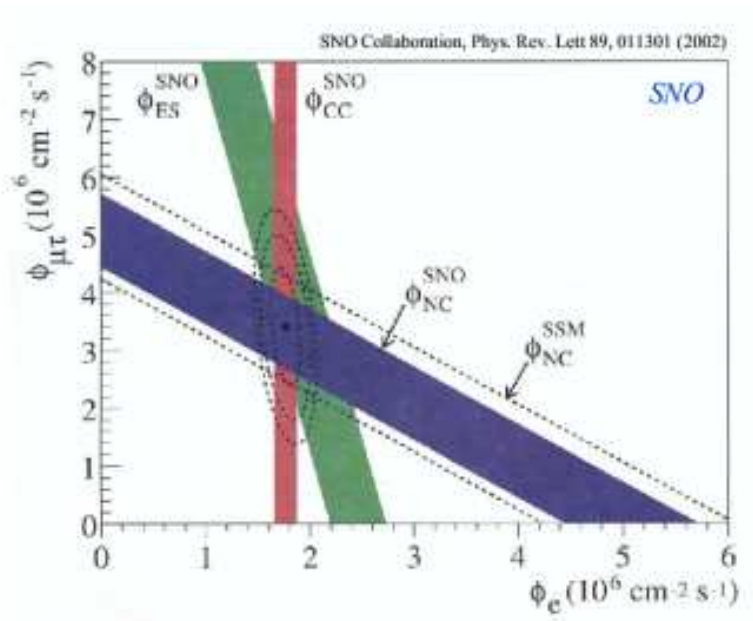

Figure 1.6: Measured ν_e and $\nu_{\mu,\tau}$ components of solar ^{8}B neutrino flux from SNO. The NC result (blue band) is in agreement with the SSM prediction (dashed line) [20].

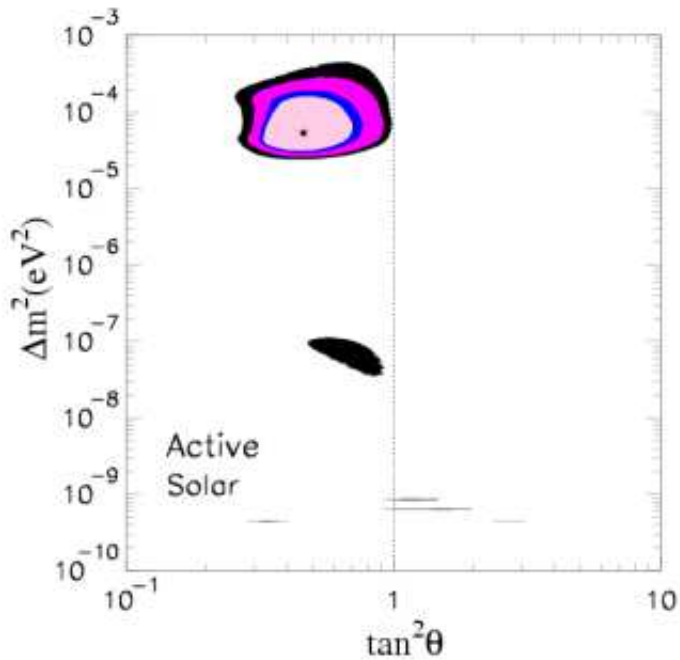

Figure 1.7: Allowed regions in neutrino oscillation mixing parameter space after the SNO neutral current result [20], combining the solar neutrino data [33]. The CL contours shown in the figure are 90%, 95%, 99%, and 99.73% (3σ). The global best-fit point is marked by a star [38].

$$\frac{N_{observed}(\overline{\nu}_e)}{N_{predicted}(\overline{\nu}_e)} = \frac{258}{365.2 \pm 23.7} = 0.686 \pm 0.044\,(stat.) \pm 0.045\,(syst.) \tag{1.37}$$

demonstrating the reactor $\overline{\nu}_e$ disappearance at 99.995% confidence level (Figure 1.8).

The last results, released in 2004, further support the neutrino oscillation evidence. The observed distortion in the $\overline{\nu}_e$ energy spectrum disagrees with the expected spectral shape in the absence of neutrino oscillation at the 99.9% confidence level while agrees with the distortion expected from the $\overline{\nu}_e$ oscillation effects (see Figure 1.8).

The KamLAND results have also had a big impact on the solar neutrino physics since it explores a region of neutrino oscillation parameters $(\Delta m^2, tan^2\theta)$ which overlaps the solar neutrino oscillation parameter space. Assuming that CPT symmetry is satisfied, the global analysis [37] including all the solar neutrino data and the KamLAND results provides more stringent limits especially in Δm^2 as shown in Figure 1.9. The LMA solution is, up to date, the only allowed region, at 3σ, in the the solar neutrino oscillation parameter space [38]:

$$\begin{aligned} \Delta m^2 &= (8.2^{+0.3}_{-0.3}) \times 10^{-5} eV^2 \\ tan^2\theta &= 0.39^{+0.05}_{-0.04}. \end{aligned} \tag{1.38}$$

1.5.3 Atmospheric neutrino experiments

Chronologically, the first evidence of neutrino oscillations was found with atmospheric neutrinos. Atmospheric neutrinos arise from the decay of particles (primarily pions, muons and kaons) produced in the collision of high energy cosmic ray particles with the atmosphere. The dominant production process is:

$$\pi^{\pm} \rightarrow \mu^{\pm} + \nu_{\mu}(\bar{\nu}_{\mu}) \tag{1.39}$$

followed by:

$$\begin{aligned} \mu^+ &\rightarrow e^+ + \bar{\nu}_{\mu} + \nu_e \\ \mu^- &\rightarrow e^- + \nu_{\mu} + \bar{\nu}_e \end{aligned} \tag{1.40}$$

The muon to electron neutrino ratio is then, in a first approximation, expected to be 2. The ratio increases since the probability that a muon does not decay before reaching the ground is higher at energies above few GeV. Thank to the (almost) independence of the primary cosmic ray flux, the uncertainty on the predicted ratio is lower than 5% even if the total neutrino flux is predicted with a precision of 20%.

The large cosmic ray background on the Earth's surface ($\sim 2 \times 10^2$ m^{-2} s^{-1}) atmospheric

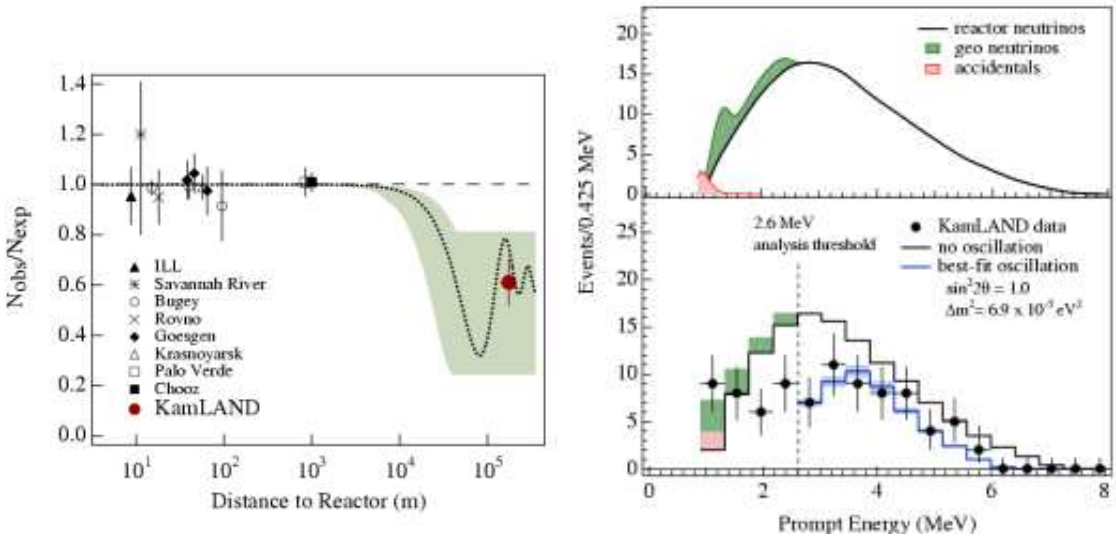

Figure 1.8: Measured to expected $\overline{\nu}_e$ flux ratio from reactor experiments (left). The shaded region corresponds to the LMA prediction at 95% C.L. from the global analysis of the solar neutrino data. The dotted line is derived assuming $\Delta m^2 = 5.5 \cdot 10^{-5} eV^2$ and $tan^2\theta = 0.42$ [35]. The comparison (right) between the expected reactor $\overline{\nu}_e$ energy spectrum (top) and the measured spectrum (bottom) highlights the energy distortion due to the neutrino oscillation effect [36].

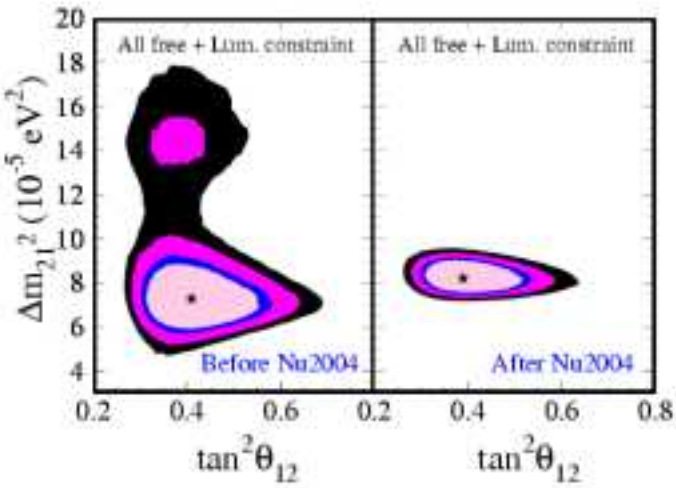

Figure 1.9: Allowed regions in neutrino oscillation mixing parameter space combining solar experiment data, KamLAND and the solar luminosity constraint (Eq 1.18). The CL contours shown in the figure are 90%, 95%, 99%, and 99.73% (3σ). The global best-fit points are marked by a star [37].

neutrinos can be detected only by deep underground experiments, observing the charged current reaction:

$$\nu\,(\bar{\nu}) + N \rightarrow l^{\pm} + X. \tag{1.41}$$

Two water Cerenkov detectors, IMB [39] and Kamiokande [40], in 1992, observed the strong suppression of ν_μ events with respect to the ν_e events:

$$R = \frac{\left(\frac{\Phi(\nu_\mu)+\Phi(\bar{\nu}_\mu)}{\Phi(\nu_e)+\Phi(\bar{\nu}_e)}\right)_{observed}}{\left(\frac{\Phi(\nu_\mu)+\Phi(\bar{\nu}_\mu)}{\Phi(\nu_e)+\Phi(\bar{\nu}_e)}\right)_{predicted}} = 0.61 \pm 0.03\,(stat.) \pm 0.05\,(syst.) \tag{1.42}$$

where $\Phi(\nu_{e,\mu})$ is the number of electron or muon like neutrinos.

The Kamiokande group, in 1994, also studied the angular dependence of the ratio [41], and agrees with a model in which downward ν_μ's have path lengths too short to oscillate, and the upward ν_μ's, which have travelled from the far side of the Earth, have been depleted by oscillations. In contrast to the muon events, the angular dependence of the electron events suggests that ν_e are not affected by oscillations. The angular dependence alone therefore supports an interpretation in terms of ν_μ disappearance. The relative low statistics, however, did not allow to discriminate between $\nu_\mu \leftrightarrow \nu_\tau$ (ν_μ disappearance) and $\nu_\mu \leftrightarrow \nu_e$ (ν_e appearance).

In the following years, the atmospheric neutrino anomaly received important confirmations from the iron calorimeter detectors, Soudan2 [42] and MACRO [43]. In 1998, finally, the large statistics water Cerenkov detector, SuperKamiokande, gathering data for more than 1000 days, reached the sensitivity to precisely quantify the asymmetry in the zenith angle [44]. The $\nu_\mu \leftrightarrow \nu_e$ oscillation hypothesis is strongly disfavored since the ν_e contained events (i. e. events whose vertex is in the detector fiducial volume) are well described by the Standard Model prediction. On the other hand, $\nu_\mu \leftrightarrow \nu_\tau$ oscillation hypothesis is consistent with the ν_μ suppression in the parameter space [45]:

$$\begin{aligned} \Delta m^2_{atm} &= (2.6 \pm 0.4) \times 10^{-3} eV^2 \\ sin^2 2\theta_{atm} &= 1^{+0.00}_{-0.05} \end{aligned} \tag{1.43}$$

This result has been confirmed by the KEK-to-Kamioka (K2K) experiment [46] that observed a 30% disappearance of accelerator generated 1.3 GeV ν_μ's after they traveled 250 km to Kamioka.

1.6 What next?

What we have learnt from solar neutrinos has involved mostly the high energy solar neutrino spectrum. 98% of the total solar neutrino flux lies below 1 MeV. Directly observing

^{7}Be or *pp* neutrinos can strongly improve our knowledge of the Sun [47]. However such measurements require the resolution of several problems, especially the presence of naturally occurring radioactive backgrounds many orders of magnitude higher than the signal to detect. The Borexino experiment is specifically designed to face this challenge by measuring in real time the ^{7}Be solar neutrino flux for the first time.

Furthermore, even if the solar neutrino problem appears resolved and many experiments have shown a clear evidence in favour of neutrino oscillations, there still remain many interesting questions to address. Oscillations only give access to the mass differences between neutrino mass eigenstates but it is crucial to define their absolute values, also for judging the role neutrinos play in astrophysical processes and cosmology. The questions of CP violation in the leptonic sector, dipole moments, mass hierarchy schemes and decay modes remain open. And the fundamental issue of whether the neutrino is of Dirac or Majorana nature still needs to be resolved.

Chapter 2

The Borexino Detector

2.1 Overview

The "next generation" solar neutrino detectors are expected to produce high statistics neutrino signals and thus provide precious information for the understanding of the solar neutrino physics. Among them, Borexino is a real-time detector specifically designed to measure the 866 keV ^{7}Be contribution to the solar neutrino flux.

The detector construction has been completed at the Gran Sasso National Laboratories (LNGS) in central Italy, under the Italian Apennines, at a depth of 3800 mwe. The main institutions responsible for Borexino come from Italy, U.S.A. and Germany, but the collaboration also includes people from Russia, France, Hungary, Poland and Canada. In the original proposal by R. Raghavan in 1987, Borex would be a detector for neutral and charged current interactions of ^{8}B solar neutrinos on ^{11}B nuclei. The name of the project derived from the use of a Boron compound, trimethylborate, as the liquid scintillator. The design for Borex required a very large fiducial mass, of about 1000 tons, and Borexino was planned as a "small-scale" prototype. However, it was realized that as long as the low energy background could be reduced, the smaller mass of Borexino would be sufficient to detect the more intense flux from ^{7}Be neutrinos. The ^{7}Be neutrino detection did not require boron, so the scintillator was changed to pseudocumene, and the focus of the experiment became the reduction of all the possible backgrounds, in particular the unshieldable intrinsic scintillator contamination.

The Counting Test Facility (CTF), a 5-ton prototype detector, was built and operated in Gran Sasso in order to test the most crucial aspects of the Borexino design, in particular the scintillator radiopurity for which the required level was orders of magnitude below the sensitivity of the methods available at the time. On the basis of the results from CTF, the construction of Borexino in Hall C of the LNGS started in 1996 (Figure 2.1).

The detection reaction for ^{7}Be solar neutrinos in Borexino is elastic scattering off electrons:

$$\nu + e^- \rightarrow \nu + e^- \tag{2.1}$$

Figure 2.1: The underground laboratories at Gran Sasso.

in an active target consisting of 300 tons of liquid scintillator. This reaction proceeds via neutral and charged current interactions, so it is sensitive not only to electron-neutrinos (ν_e), but also to muon or tau-neutrinos (ν_μ and ν_τ). The scintillation light produced by the recoil electrons is detected by an array of 2200 photomultipliers. The high light yield of the liquid scintillation technique allows the detection in Borexino of electrons with energies as low as a few tens of keV. However, the low energy background limits the effective threshold for the neutrino-recoiled electrons at 250 keV.

The separation of signal and background relies on the identification of the Compton-like edge in the recoil electron energy spectrum at 667 keV due to the fact that ^{7}Be neutrinos are monoenergetic. No event-by-event neutrino signature is possible in Borexino and the fluorescence light production is not directional, so that the signal extraction from the background must be made statistically. There is also a temporal signature for the solar neutrino flux: the eccentricity of Earth's orbit provokes a 7% annual variation of the neutrino rate ($1/R^2$ effect).

The lack of an event-by-event signature makes the accuracy of the background control the main priority for the Borexino experiment. In fact, Borexino has the most challenging background requirements for a large volume underground experiment. For a signal/noise ratio of 1, a maximum background rate of 0.5 events/day/ton or 5×10^{-8} Bq/kg in the energy range 250-800 keV (also known as the "neutrino energy window") is required.

2.2 The structure of the detector

The Borexino detector structure is organized in concentric regions as shown in Figure 2.2. The structure consists in the active liquid scintillator target contained in a thin nylon vessel and surrounded by a shielding (buffer) liquid. The PMT's are supported by a stainless steel sphere which contains both the scintillator and the buffer liquid. A water buffer provides the last shielding shell, as well as the active volume for the muon detector.

The design was driven by the balanced optimization of three main parameters:

- *Solar neutrinos statistic.* The low cross sections for neutrino interactions impose a maximization of the count rate by the increasing of the target mass. In order to reach a SSM-LMA count rate of $\sim$ 40 ev/day, the detector fiducial mass must be at least equal to 100 tons.

- *Signal-to-background ratio.* The strict requirements on the radioactive background rate have driven the choices of the scintillator composition and of other detector materials. Moreover, the concentric structure, a succession of increasingly pure shells, shields the active volume. It also led to the inclusion in the detector of a muon veto system, and to the addition of a light quencher to the buffer liquid, in order to make it a really passive shield.

- *Detector resolution.* Maximizing the light collection efficiency leads to improve the energy resolution, fundamental for the recognition of the ^{7}Be neutrino edge, as well as the position resolution and the particle identification efficiency, important for background discrimination. This implied a major requirement in the choice of the scintillator, that should maximize the light yield and minimize the attenuation, of the nylon vessels, that must be as transparent as possible and of the PMT's, with a large collection area, further improved by the use of optical concentrators.

In this paragraph, I give a brief description of the fundamental detector components. For a detailed description of the design goals of Borexino, see ref. [48, 49].

The active target of the detector consists of 300 tons of organic liquid scintillator; this is a 1.5 g/l solution of 2,5-dipheniyloxazole ($C_{15}H_{11}NO$, PPO) in 1,2,4-trymethyl-benzene or pseudocumene (PC) solvent ($C_6H_3(CH_3)_3$) [50, 51]. PC is characterized by a high transparency (5-10 m mean free path), and a fast decay time of the scintillation light ($\sim$ 4 ns), essential for good spatial resolution of the detector. The peak emission wavelength is equal to 430 ns (see Figure 2.4), well above the sensitivity threshold of the phototubes. The primary excitation efficiency depends on the solvent only and is of the order of 5 %, corresponding to an average fluorescence yield of about 10^4 optical photons/MeV. However, the fraction of excitation energy converted into scintillation photons, the fluorescence quantum efficiency, increases from 40 % to 82 % with the addition of PPO to the pseudocumene. Furthermore, the PPO additive to

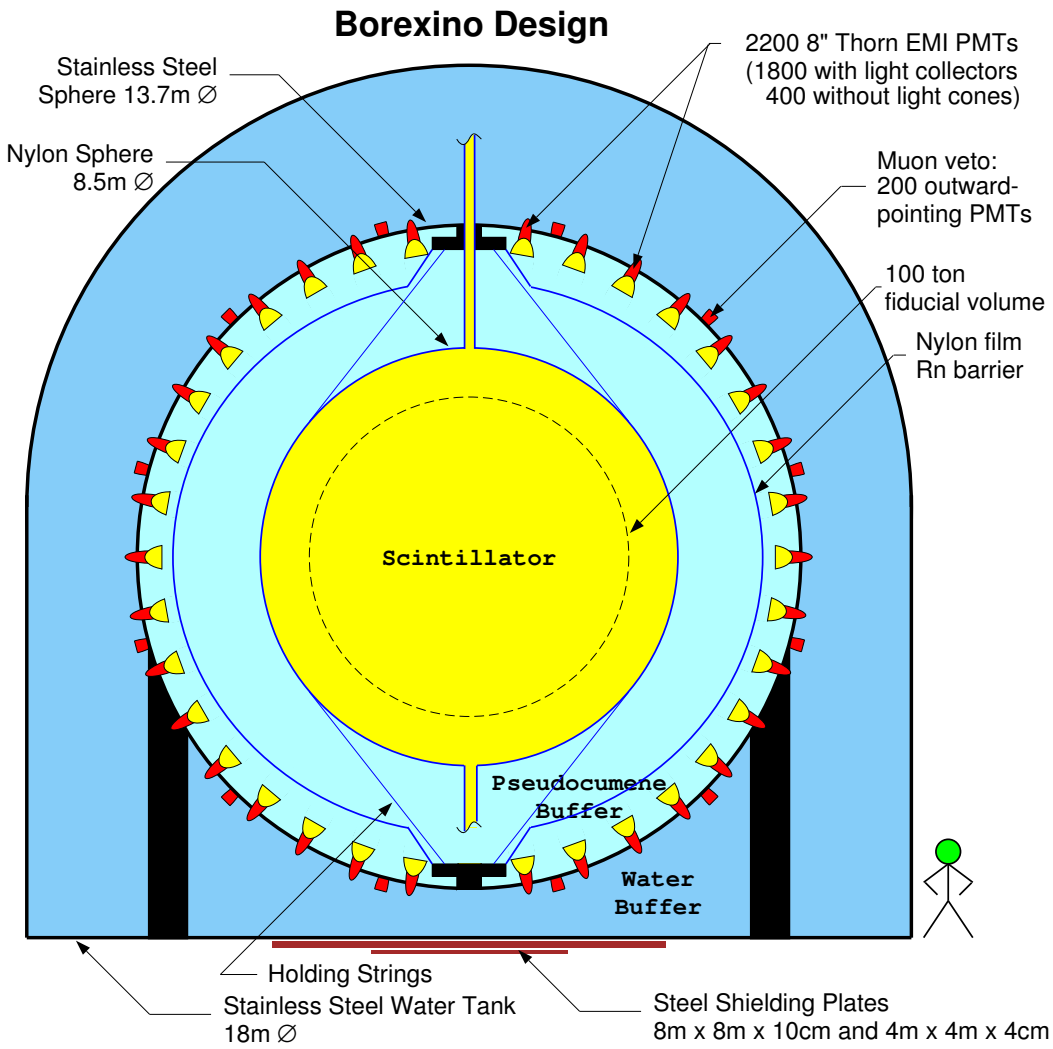

Figure 2.2: Schematics of the Borexino detector at Gran Sasso.

the scintillator works as a wavelength shifter to fine tune the scintillation light to the spectral response of the PMT's. The scintillation spectrum of the PC+PPO scintillator versus that of pure PC is shown in Figure 2.4.

The scintillator is mechanically confined by a nylon spherical "balloon", referred as the Inner Vessel (IV), with 8.5 m diameter and 125 μm thick. The material of construction for the IV must meet stringent requirements of cleanliness, since it is the only component in direct contact with the scintillator (optical clarity, mechanical strength and chemical resistance to the scintillator). A second nylon vessel is installed outside the inner vessel in order to insulate it from ^{222}Rn and other impurities that might otherwise diffuse into the vicinity of the sensitive volume from outer regions of the detector.

The buffer liquid fills the region between the IV and the stainless steel sphere (SSS). The

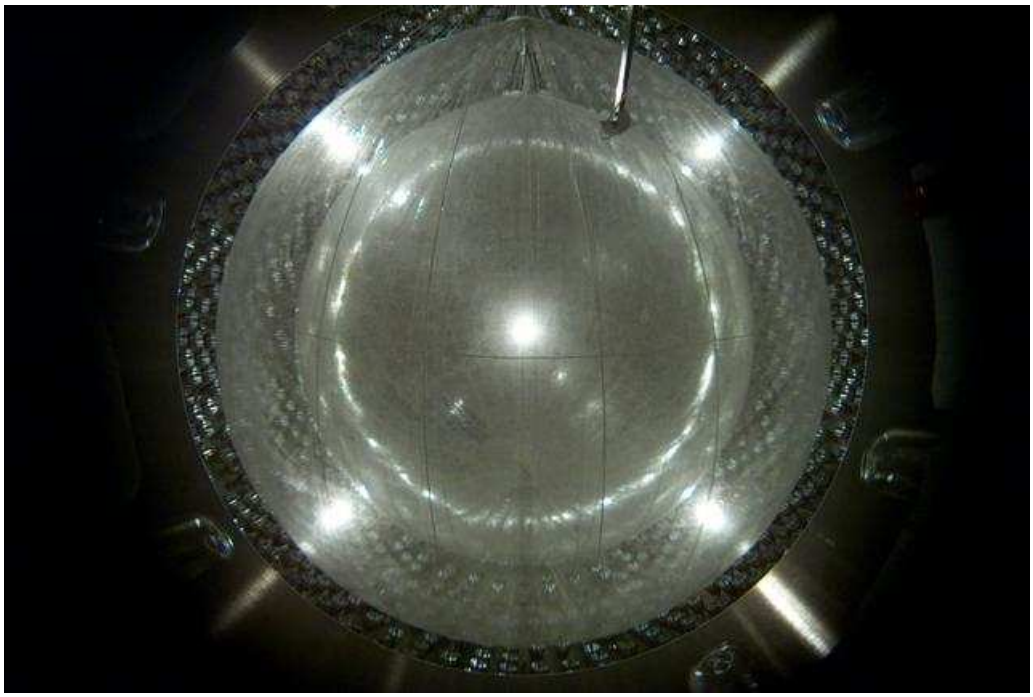

Figure 2.3: A look inside the Borexino Stainless Steel Sphere (SSS). Clearly visible are the inner and outer vessels.

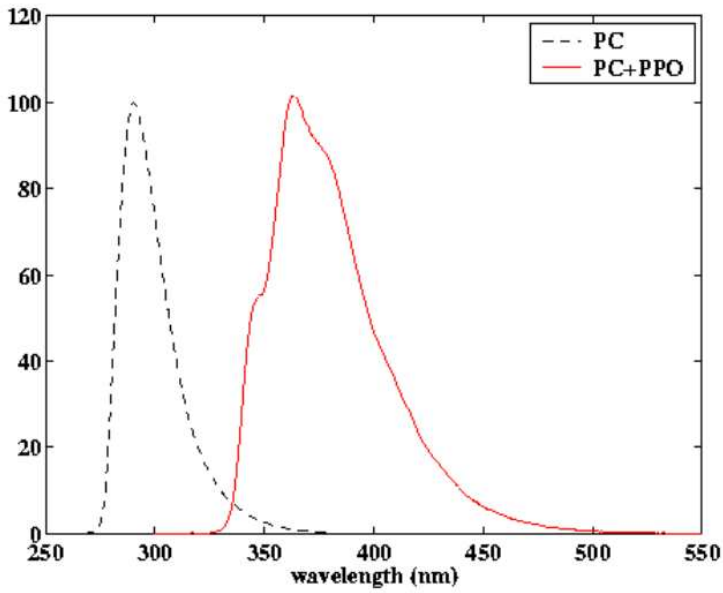

Figure 2.4: Scintillation spectrum of the PC+PPO scintillator versus that of pure PC.

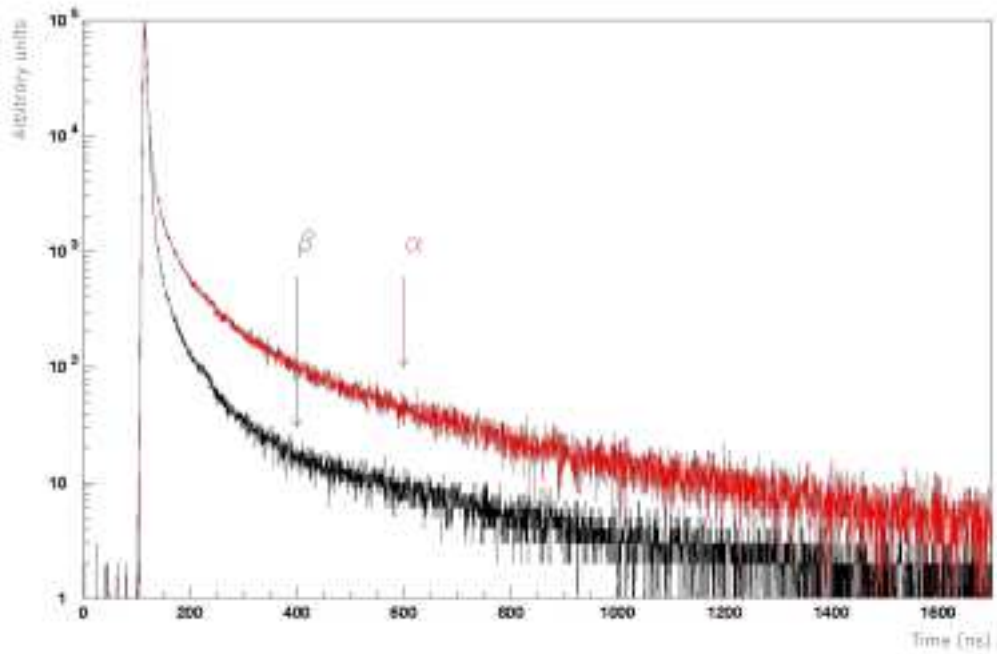

Figure 2.5: The different decay time of the scintillation light produced by α (red) and β (black) particles. From a laboratory measurement [59].

buffer liquid consists of pseudocumene as well as the scintillator. Such choice presents a series of advantages. First of all, its density matches the scintillator one within 0.1% in order to minimize the mechanical stresses of the inner vessel. Its index of refraction is very similar to the scintillator (within 1%) to avoid optical effects to the scintillation light. The light attenuation length and the scattering mean free path length exceed 5 m at the scintillation light wavelength (430 nm). Finally, PC, without fluors, has a scintillation light yield $\sim$ 20 times lower than that of the scintillator solution. The addition of the DMP quencher (5 g/l dimethylphthalate) to the buffer fluid drastically reduces scintillation light by a factor of $\sim$ 10. This way, the inner buffer is really a passive shield and the detected events can only have taken place inside the scintillator.

The light mean free path lengths and the Cerenkov light emission yield, important for the muon veto, are not affected by the presence of the DMP quencher in the buffer.

The stainless steel sphere, with 13.7 m diameter, separates the buffer from the external 2 m shield of ultrapure water (Figure 2.6). It also sustains the structure for the 2200 phototubes, directly mounted on its internal surface. On the sphere's outside, 200 additional PMT's are mounted for detecting the Cerenkov radiation produced by cosmic rays in water, as a part of the muon veto system. The internal SSS surface has been pickled and passivated in order to assure a high level of cleanliness. The result is a matte finish that diffusely reflects $\sim$ 40 % of the incident light.

The most external shell in Borexino is the water tank, a stainless steel domed cylinder with 18 m diameter and 16.5 m high. The internal walls are covered by Tyvek sheets which diffusely reflect the Cerenkov light radiated by cosmic rays crossing the water buffer [132, 54]. The ultrapure water adsorbs the γ and the neutron flux emanated from the rocks of the experimental hall.

The phototubes are 20 cm diameter Thorn-EMI 9351 (Figure 2.7). They have been developed together with the manufacturer to contain very low amounts of residual radioactivity in the glass. The PMT's and read out electronics are appropriately chosen to be able to detect very small amounts of light, typical of recoil electrons below 1 MeV. The PMT's are suitable for single photoelectron count [55] and the dynamic range of the electronics is optimized for low energy counting [56, 57]. Their sensitivity threshold is 350 nm and the peak quantum efficiency is at 420 nm. Furthermore, the timing jitter (transit time spread) is 1 ns and the dark noise rate is about 1 kHz. Precise timing of the PMT's is crucial for the spatial reconstruction of each event inside the detector. The read out electronics will also provide very efficient discrimination ($>$ 90%) of αs and βs, exploiting the large difference on the tail of the decay time distributions for α and β excitation modes (as shown in Figure 2.5 [58, 59, 60, 61]). Approximately 1800 of them are equipped with aluminum light concentrators designed to capture the light of events inside the IV. Taking into account the concentrator aperture diameter of 32 cm and a its reflectivity of 90% and averaging over the scintillator emission spectrum, the

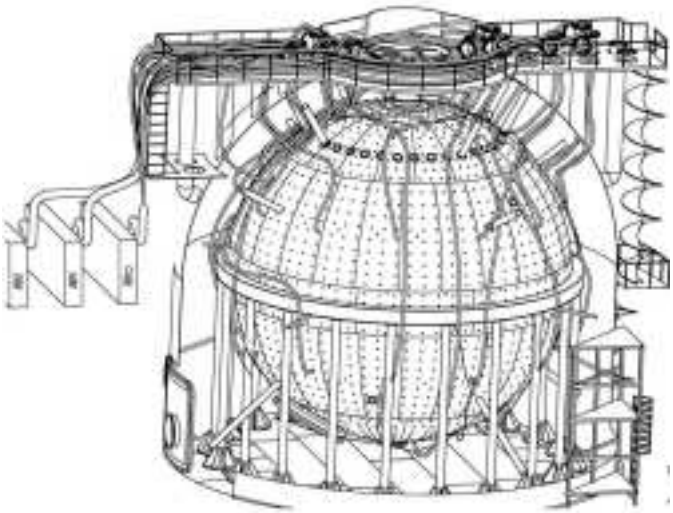

Figure 2.6: Stainless Steel Sphere inside the Water Tank. The SSS support structure, the PMT ports and cables are shown.

effective light collection area of the PMT is increased by a factor of 2.4. So the total fraction of solid angle covered by the 2214 PMT's is 32 %. The PMT's without concentrators will also capture the light from the buffer region. In addition to residual scintillation, they will detect Cerenkov light associated with the passage of a muon, and are therefore complementary to the Borexino muon detector. A close view of the Borexino PMT's, with and without concentrators is displayed in Figure 2.7.

Several auxiliary plants are devoted to the overall fluid handling and circulation and to the purification of the scintillator, buffer solution, and water. Water is purified by reverse osmosis deionization and nitrogen stripping to eliminate gaseous radioactive species and oxygen. The purification processes for pseudocumene include nitrogen stripping, counter current water extraction, vacuum distillation and filtration system, to remove suspended dust particles larger than 0.05 μm. Nitrogen stripping has proved effective in removing radioactive gaseous species as well as oxygen. The water extraction process is effective for ionic impurity removal, such as metals like uranium. The vacuum distillation, finally, is focused on low volatility and non ionic contaminants, such as dust particles and degraded solvent molecules. An extensive description of the Borexino detector and its auxiliary plants is found in [62].

The calibration program for Borexino [63] covers the energy and time response of the detector using built-in systems, active tags of trace impurities in the scintillator and the insertion of known radioactive sources. The pulse time and gain of each PMT is calibrated by a laser system [64]. Photons from a laser are carried by thin quartz fibers to each optical concentrator with a light yield corresponding to single photoelectron signals. The external muon veto is calibrated by a set of blue light LEDs. Optical sources are also exploited for

Figure 2.7: A closeup view of the Borexino photomultiplier tubes (PMT's). On the PMT's equipped with the light concentrator is visible the thin fiber for the calibration of the pulse time and gain response.

monitoring the transparency of the scintillator and the buffer liquid.

Natural calibration sources like ^{14}C and 2.2 MeV γs emitted by the capture of neutron on protons, can be used for monitoring the energy response. An artificial point-like source, like the ^{222}Rn source used in CTF [65], located at a known position, is necessary in order to interpret the signal strength and to calibrate the position reconstruction algorithm. An unambiguous test of the overall detector response will be provided by a calibration with an artificial sub-MeV neutrino source, as ^{51}Cr, with activities in the MCu range.

2.3 Radioactivity requirements and background rejection

The expected neutrino signal in Borexino in the 100 tons fiducial volume and in the neutrino energy window [250 - 800] keV (NW) is $\sim$ 10 events/day (assuming SSM and LMA oscillation scenario). In order to discriminate the signal, the experiment requires a signal-to-background ratio equal or less than 1. This constrains the total acceptable background to be on the order of 10^{-6} Bq/ton or better.

The Borexino collaboration has focused much effort on the reduction of the contamination intrinsic to the scintillator (as reported in Table 2.1) and of the radioactivity coming from the other materials of the detector.

Since organic liquid scintillator are predominantly composed of carbon, the intrinsic concentration of the radioisotope ^{14}C can constitute the main background at low energies. ^{14}C decays via β^- emitting an electron with 156 keV endpoint energy and with a long mean life of 8266 years. Because of finite detector energy resolution, events from this source could be

observed at higher energy inside the detector. The lower threshold of the neutrino window is set to 250 keV in order to contain the ^{12}C contamination. To limit the ^{14}C activity to than 1 c/d in the NW, the ^{14}C/^{12}C ratio must be less than 10^{-18}.

Borexino can tolerate level of ^{238}U and ^{232}Th contamination no greater than $\sim 10^{-16}$g/g of PC. The first CTF test has demonstrated the possibility to reach such a level of contamination. The presence of these species can be efficiently tagged by looking for short β-α delayed consecutive decays within their radioactive chains. In the ^{238}U chain, the ^{214}Bi-^{214}Po sequence has a mean lifetime of 235 μs while the ^{232}Th chain can be easily tagged by the ^{212}Bi-^{212}Po sequence (432 ns mean lifetime). Assuming secular equilibrium, it is possible to extrapolate the activity of ^{238}U and ^{232}Th chain in the scintillator from the measurement of the two fast sequences. In case of radon or thoron infiltration, the ^{238}U and ^{232}Th chains can be distinguished from the ^{222}Rn and ^{220}Rn "segments", respectively, by comparing the decay lifetime of detected short sequences.

Also ^{85}Kr can be tagged by the delayed coincidence exploiting the secondary decay channel to the metastable ^{85m}Rb (0.43% branching ratio) generating a β-γ delayed sequence with a 1.46 μs mean life.

Other dangerous background elements are ^{40}K and ^{39}Ar, both β emitters. The maximum acceptable contamination limit on the total potassium abundance is K_{nat} 10^{-14} g/g (K_{nat} indicates the overall potassium content including all isotopes with their natural abundance) while the limit for ^{39}Ar is 0.1 μBq/m^3. Decays without time coincidence patterns can be identified in different ways: α decays can be spotted by pulse shape discrimination, while a careful energy spectrum analysis can identify and separate individual, known sources which may then be statistically subtracted from the total energy spectrum.

The radioactivity originated in the materials of the external components of the detector (nylon, PMT's, pipes, fibers, etc) are generically considered to be as "external background". The external background is mainly composed by γ rays, but also comprises radon contamination from the buffer liquid and from the vessel. The size of the fiducial volume will depend on the residual activity from the external background leaking into the center of the detector. A larger fiducial target mass implies an increased physics potential of the experiment. The total expected rate in the 100 tons fiducial volume from external background in the NW is 0.11 ev/day.

The muon activity in the experimental hall, equal to 1 event/m^2/h, causes detectable Cerenkov light in the ultrapure water. Special pattern recognition algorithms were developed in order to identify such events. Highly efficient ($\sim$ 99%) muon veto has been included in Borexino to tag these events.

Isotope	Source	Typical conc.	Tolerable level	Strategy
^{14}C	cosmogenic (from ^{14}N)	$\frac{^{14}C}{^{12}C} \leq 10^{-12}$	$\frac{^{14}C}{^{12}C} \leq 10^{-18}$	use petroleum derivate (old carbon)
^{7}Be	cosmogenic (from ^{12}C)	3 x 10^{-2}Bq/ton	$<10^{-6}$Bq/ton	distillation or underground storage of scintillator
^{222}Rn	air and emanation from materials	100 ^{222}Rn atoms per cm^3 air	1 ^{222}Rn atoms per ton PC	nitrogen stripping
^{210}Po ^{210}Bi	^{210}Pb on the IV surface			minimum exposure, event position ident.
^{238}U ^{232}Th	suspended dust	2 x 10^{-6}g/g in dust	$< 10^{-6}$g/g in PC	water extraction, distillation
K_{nat}	dust or flour contamination	2 x 10^{-6}g/g in dust	$< 10^{-13}$g/g in scintillator	water extraction
^{39}Ar	air	1.4 Bq/m^3 in Ar	0.1 μBq/m^3 in PC	nitrogen stripping
^{85}Kr	air	1 MBq/m^3 in Kr	0.1 μBq/m^3 in PC	nitrogen stripping

Table 2.1: Radiopurity requirements for the Borexino scintillator [66].

2.4 Detection mechanism and physics potential

The Borexino detection mechanism relies on the neutrino elastic scattering off the electrons of the scintillator. The interaction energy of the incoming solar neutrinos is much higher than the typical electronic molecular binding energies (few keV) so that in the scattering reaction the electron can be considered free. In the scattering off protons or nuclei, instead, the transfered momentum, is too low for producing detectable charged particles.

As is clearly visible from the first order Feynman diagrams for the ν-e scattering in Figure 2.8, ν_e scatters off electrons via the charged and neutral current while ν_μ and ν_τ interacts only via neutral currents. Because of the extra term in the scattering amplitude, ν_e-e scattering is 4.5 times larger than for other flavours, in the energy region around 1 MeV.

The differential cross section $\frac{d\sigma}{dT}$ for neutrino-electron elastic was originally derived at first order by 't Hooft [68]:

$$\frac{d\sigma}{dT} = \frac{2\,G_F^2\,m_e^2}{\pi\hbar^4}\left[g_L^2 + g_R^2\left(1-\frac{T}{E_\nu}\right)^2 - g_L\,g_R\frac{m_e\,T}{E_\nu^2}\right], \tag{2.2}$$

where and T and E_ν are the kinetic energies of the electron and the neutrino, respectively, G_F is the Fermi constant of weak interaction, m_e the electron mass and $g_R = sin^2\theta_W$ (θ_W is the Weinberg angle). $g_L = +\frac{1}{2} + sin^2\theta_W$ for the ν_e-e interaction while $g_L = -\frac{1}{2} + sin^2\theta_W$ for the $\nu_{\mu,\tau}$-e interaction. Radiative corrections are not included. They would modify the

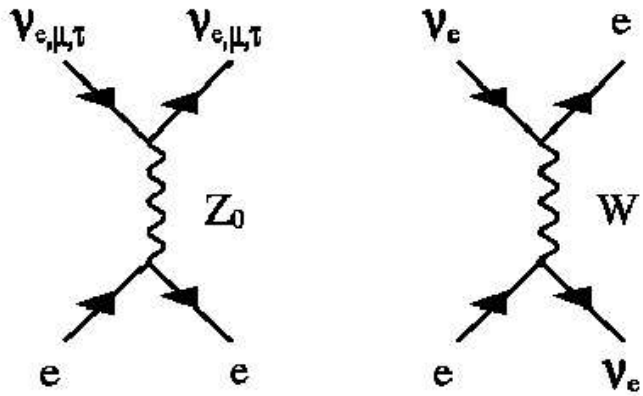

Figure 2.8: Feynman diagrams for the neutrino scattering off electron.

differential cross section based on the tree level approximation by less than 2%.

The total cross section is the integral of Eq 2.2:

$$\sigma = \int_0^{T_{max}} \frac{d\sigma}{dt} dt = \frac{2\,G_F^2\,m_e^2\,T_{max}}{\pi\hbar^4} \left[(g_L^2 + g_R^2) - \left(\frac{g_R^2}{E_\nu} - g_L\,g_R \frac{m_e}{E_\nu^2} \right) T_{max} + g_E^2 \frac{T_{max}^2}{2E_\nu^2} \right], \quad (2.3)$$

where

$$T_{max} = \frac{E_\nu}{1 + \frac{m_e}{2E_\nu}} \quad (2.4)$$

is the maximum kinetic energy of the scattered electron. From Eq 2.4, the signal from the monochromatic ^{7}Be solar neutrinos (862 keV) shows then a distinctive Compton-like edge of the scattered electron at 667 keV as shown in Figure 2.10. The total cross section for the ^{7}Be-ν interaction is thus

$$\sigma(^7Be) = 88.1 \cdot 10^{-46} cm^2. \quad (2.5)$$

2.4.1 The solar neutrino physics from Borexino

The interaction rate for neutrino electron scattering is given by:

$$R = N_e \int_0^{E_\nu} \Phi(q) \left[P_{ee}(q) \int_0^{Tmax} \frac{d\sigma_e(q,t)}{dt} dt + (1 - P_{ee}(q)) \int_0^{Tmax} \frac{d\sigma_{\mu,\tau}(q,t)}{dt} dt \right] dq, \quad (2.6)$$

where N_e is the electron density in the scintillator target, Φ(q) the average neutrino flux on Earth and P_{ee} the electron neutrino survival probability. $\frac{d\sigma_e}{dt}$ and $\frac{d\sigma_{\mu,\tau}}{dt}$ are the differential cross

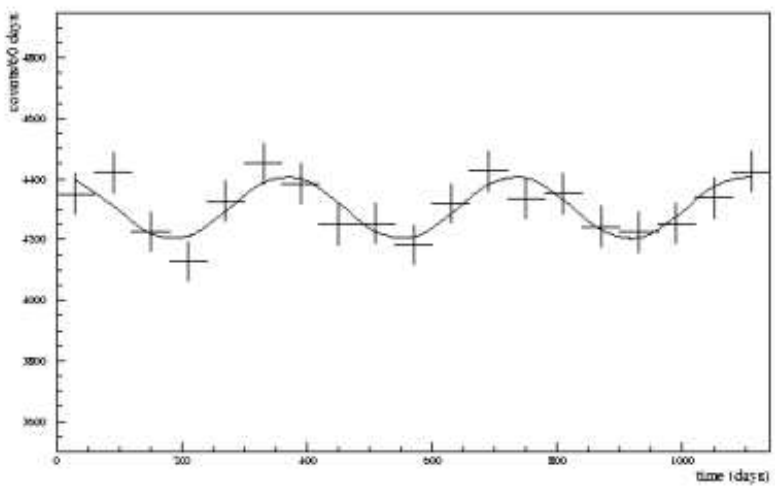

Figure 2.9: Simulated data showing the seasonal variation of the neutrino signal in the NW after three years of data taking. No oscillation scenario is assumed. The plot is taken from [69].

section for electron neutrinos (see Eq 2.2) and for muon and tauon neutrinos, respectively. The survival probability depends on the allowed Δm^2 and $tan^2\theta$ parameters. Consequently, the interaction rate depends on the oscillation scenario LMA that, as already mentioned in the previous chapter, is the only accepted solution at 3 σ. The prediction for the reduced ν_e-e scattering rate is:

$$f(^7Be) = \frac{\Phi(^7Be)}{\Phi_{BP04}(^7Be)} = 0.64 \pm 0.02. \tag{2.7}$$

The expected rate in Borexino is then no larger than 40 events/day, approximately 25 of which are from ^{7}Be neutrinos. For this solution, the predicted ^{7}Be day-night effect asymmetry, the flavours regeneration in the Earth, is too small to be observed.

The seasonal variation of the total measured rate as a function of the Earth's distance from the Sun along its orbit is the signature that confirms the solar origin of the neutrino flux. The solid angle differs by approximately 7% between aphelion and perihelion (Figure 2.9).

The sensitivity of Borexino to other solar neutrino sources, like CNO, *pep* and ^{8}B is limited, but might not be negligible, if the background rates are small enough. In Figure 2.10 the expected energy spectra of the all solar neutrinos in the Borexino fiducial volume are shown, assuming the SSM-LMA scenario and 3 years of data taking. The measurement of the CNO and *pep* neutrino rates beyond the ^{7}Be energy window, (in the range [0.8 - 1.6] MeV), depends especially on the ^{210}Bi, ^{214}Bi and muon induced ^{11}C contamination. While a strategy for reducing the ^{210}Bi, ^{214}Bi background has been widely studied in CTF, the strategy for tagging ^{11}C is still being investigated. In Chapter 5, I give a detailed description of the ^{11}C

rate measurement in CTF3. The possibility to discriminate the ^{11}C background efficiently will provide Borexino a powerful tool to open the window also to the *pep* and CNO spectroscopy.

2.4.2 Physics beyond the solar neutrinos

Borexino can detect electron antineutrinos via their capture on scintillator protons:

$$\overline{\nu_e} + p \rightarrow n + e^+, \tag{2.8}$$

which has an energy threshold at Q = 1.8 MeV. The total energy deposited by the positron in the scintillator is related to the energy of the antineutrino by:

$$E(e^+) = E(\overline{\nu_e}) - Q + 2m_e. \tag{2.9}$$

The neutron capture induces an emission of a 2.2 MeV γ after $\sim$ 200 μs. The delayed coincidence between e^+ and γ provides a signature of $\overline{\nu_e}$ with a sensitivity of a few events per year.

The main sources of antineutrinos are the nuclear power plants locate in Germany, France and Switzerland. These $\overline{\nu_e}$ are produced with a known flux and spectrum and at energies up to 8 MeV are expected at the rate of 30 events/year. Evidence for oscillation would come from their disappearance and from spectral distortion [86].

A measurement of $\overline{\nu_e}$ emitted by the radioactive elements in the mantle and the crust of the Earth, provides information about the radiochemical composition of Earth. The expected $\overline{\nu_e}$ rate is of the order of several tents of events per year, in the energy range [0 - 3.3] MeV [71, 72].

Intense neutrino and antineutrino fluxes of all flavours are emitted in supernovae collapses, with average energies 10-30 MeV. The dominant channel for detection of supernovae neutrinos is again the antineutrino capture on protons. Approximately 80 events are expected from a supernova collapse in the center of our galaxy [73, 74].

Finally, solar antineutrino detection, excluded by solar astrophysics, can provide an interesting window on a non standard physics. The current upper limit on the $\overline{\nu_e}$ flux from the Sun (5×10^{-4} cm^{-2} s^{-1}, corresponding to approximately 100 events/ year [75]) could be significantly improved by Borexino.

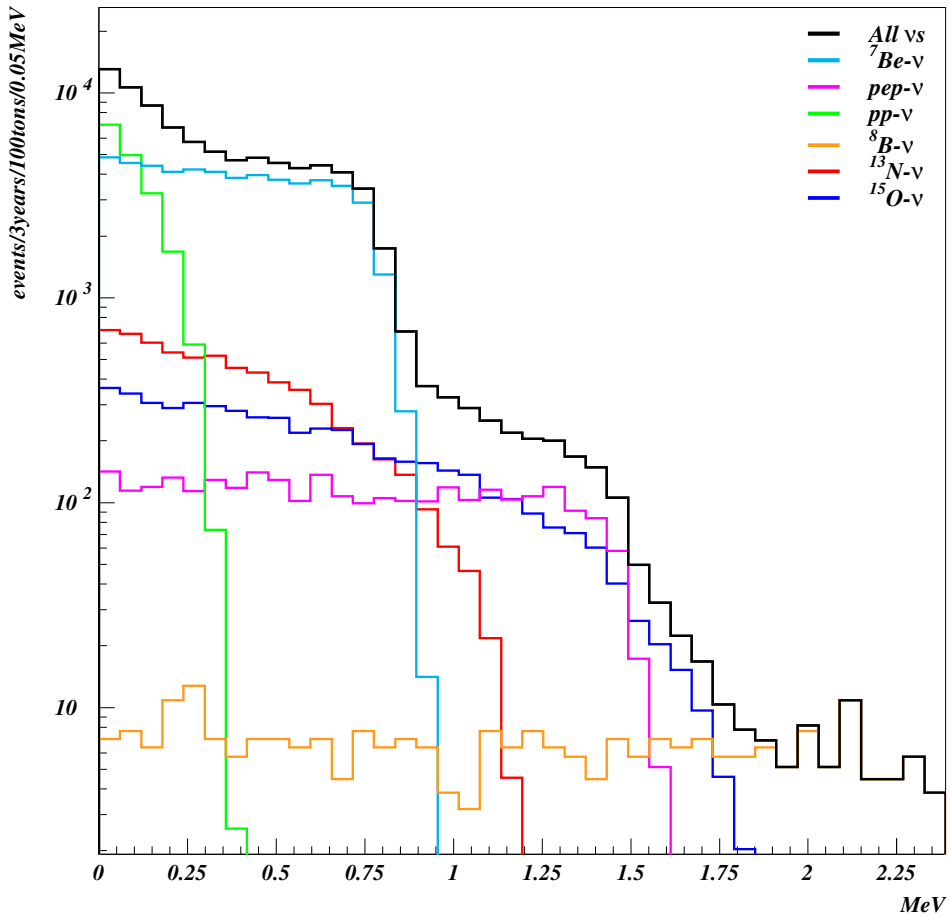

Figure 2.10: Expected neutrino spectra in the fiducial volume after 3 years of data-taking assuming the SSM-LMA scenario. The histogram in black is the sum of the all signals.

Chapter 3

Low Argon and Krypton Nitrogen

3.1 Introduction

Nitrogen plays a fundamental role in the Borexino experiment. It is widely used to remove gaseous contaminants from the scintillator, water and buffer liquid and to flush the large volume supporting components such as storage tanks, columns, pipes etc.. Nitrogen is produced in liquid phase by fractional distillation of air, which is used to separate mixtures of miscible liquids. The process depends on the components of the mixture having different boiling points. The liquid is heated so that it turns into a gas. The vapours pass through a fractionating column where they are gradually cooled. As each of the components of the mixture cools to its boiling point, it turns back into a liquid. The different components of the mixture condense at different levels in the fractionating column and thus may be separated.

Air contains radioactive nuclides, which are mostly noble gases. Nitrogen produced from air contains, thus, radioactive nuclides which can contaminate Borexino in the sparging purification step.

The rare-gas radioisotopes ^{39}Ar and ^{85}Kr are much less abundant in the atmosphere then ^{222}Rn, on which the Borexino collaboration has spent a great deal of effort to control it. Nevertheless,^{85}Kr was identified as a background source through CTF measurements. Both the nuclides, ^{39}Ar and ^{85}Kr, are crucial for the experiment because of their long lifetime and of the β particles emission with energies falling in the energy range of the neutrino signal (250 - 800 keV):

- ^{39}Ar β-decays to the ground-state of ^{39}K (no γ-ray emissions, $\tau_{1/2} = 269$ y) with endpoint Q = 0.565 MeV;

- ^{85}Kr β-decays with a 99.56% branch to the ground-state of ^{85}Rb ($\tau_{1/2} = 10.76$ y, endpoint Q = 0.687) and a weak 0.43% branch to a metastable level followed after 1.46 μs by a 514 keV γ-ray emission.

	^{39}Ar	^{85}Kr
Activity in air	1.4 Bq/m^3 in Ar	1 MBq/m^3 in Kr
Solubility N_2/PC	4.4	1.4
Requested activity in PC	0.1 μBq/m^3	0.1 μBq/m^3
Requested activity in N_2	0.44 μBq/m^3	0.14 μBq/m^3

Table 3.1: Activity of ^{39}Ar and ^{85}Kr in air and their requested limits in PC and N_2. The correspondent concentrations of natural Ar and Kr in N_2 are 0.31 ppm and 0.14 ppt, respectively.

The feasibility of the experiment imposes a threshold on the activity for both nuclides equal to 1 cpd (A = 0.1 μBq/m^3 in PC) over the entire Borexino fiducial volume (100 ton). To obtain a high purity nitrogen, we have investigated two options:

- developing a technique to purify in-situ nitrogen from argon and krypton;
- looking for pure enough nitrogen on the market.

In this chapter I provide a detailed description of methodologies and results for both the options.

3.2 ^{39}Ar and ^{85}Kr activities in Borexino

In nature ^{39}Ar is mainly produced by cosmic-ray induced reactions in the atmosphere and by reactions due to secondary cosmic-rays (neutrons and muons) at the surface of the lithosphere. Relative concentration of ^{39}Ar in atmosphere, as reported in the literature [76], is at the level of $(8.1\pm0.3)\times10^{-16}$ compare to stable Ar. The correspondent activity is equal to about 1.4 Bq/m^3 in Ar. To determine the amount of ^{39}Ar in the scintillator after the sparging, we assume that an infinite amount of nitrogen gas is in contact with the scintillator so that the equilibrium between the scintillator liquid phase and the nitrogen gas phase is established. The relative solubility coefficient between nitrogen and PC (S) is 4.4. The requested limit for ^{39}Ar activity in nitrogen is then

$$A \times S = 0.44\,\mu Bq/m^3 \tag{3.1}$$

which corresponds to a concentration of 0.36 ppm[1] of Ar in N_2.

^{85}Kr is anthropogenic produced from fission of uranium and plutonium in nuclear reactors and released into the atmosphere due to reprocessing of spent nuclear fuel rods. Its concentration in the atmosphere relative to stable Kr is about $\sim$ 2x10^{-11} and its correspondent activity

[1] In literature, ppm, ppt or ppb can be defined as volumetric, molecular or mass ratios. In this thesis, I will always refer to them as volumetric ratio, thus: $1\,ppm = 10^{-6}\,\frac{m^3}{m^3}$.

is 1 Bq/m^3 in air (1 MBq/m^3 in Kr). Assuming the same hypothesis as in the Ar case, and given its relative solubility between the gas phase (N_2) and the liquid phase (PC) $S = 1.4$, the requested limit for ^{85}Kr activity in nitrogen is then

$$A \times S = 0.14\,\mu Bq/m^3 \tag{3.2}$$

which corresponds to a concentration of 0.14 ppt of Kr in N_2.

There are only very limited possibilities to measure such low ^{39}Ar and ^{85}Kr concentrations in nitrogen. The easiest possibility is offered by specially tuned mass spectrometry.

^{39}Ar and ^{85}Kr concentrations are determined in nitrogen indirectly by measuring the natural Ar and Kr and taking into account the well known specific Ar and Kr concentrations of both isotopes in the atmosphere. We used the VG3600 spectrometer [83, 84], a very sensitive device able to measure krypton down to 10^{-13} cm^3 and argon down to 5x10^{-10} cm^3 [85]. Typically the nitrogen samples were about 1 cm^3, resulting a detectable krypton concentration of $\sim$ 0.1 ppt and $\sim$ 0.5 ppb for argon. Both limits are derived by assuming the signal-to-background ratio to be 1. Since the background of the system is measured with an uncertainty of about 10% for Ar and 20% for Kr, the measurements have uncertainties of about 25% and 45% for Ar and Kr, respectively. If necessary, the volume of the sample can be increased to 10-15 cm^3. Possible deviations from the natural (air-like) isotopic abundance in the sample are cross-checked by measuring the ^{36}Ar/^{38}Ar/^{40}Ar and ^{82}Kr/^{83}Kr/^{84}Kr/^{86}Kr ratios.

3.3 Krypton adsorption on carbon-based adsorbers

The process of adsorption occurs when liquid or gaseous molecules come into contact with and adhere to a solid surface. Adsorption processes can be classified as physical or chemical. Adsorption is physical (*physisorption*) when the only forces which are involved in the bonding between molecule and the solid substrate are the London-Van Der Waals forces. Chemical bonding, or *chemisorption*, occurs when a molecule interacts with the surface to form covalent or ionic bond. These bonds lead to a change in the chemical form of the adsorbed compounds, and it is therefore irreversible. On the other hand, molecules physically adsorbed onto a solid can be released by applying heat, and therefore the process is reversible. The distinction between the two processes is usually classified according to the enthalpy of adsorption. In general, if the enthalpy of adsorption is similar to the energy of condensation (less then 25 kcal/mol), the interaction is regarded as physisorption while chemisorption occurs when enthalpy is bigger then 40 kcal/mol.

Several kinds of adsorbent are commonly used. The most common is activated carbon. *Activation* is the process that produces the porous structure essential for effective adsorption.

Activated carbon can attract non-polar molecules and they have typical surface areas between 300 and 1500 m^2/g. We have concentrated our studies not only on carbon-based adsorbers but also on zeolites (AlSiO-based) which have uncommon properties: they are crystalline and the micro-pores are uniform in dimension. Furthermore, they can discriminate between nearly identically sized molecules.

3.3.1 The Langmuir model and the Henry constant

Many models have been proposed to describe and characterize the adsorption process. The simplest is the Langmuir Isotherm [77]. It assumes that each unit of surface area consists of n_{mono} sites and each site can adsorb one molecule. All the sites are energetically equivalent and molecules are adsorbed in one single layer (mono-layer). Moreover, the model assumes no interaction among the adsorbed molecules, and a thermodynamic equilibrium between the adsorption and desorption rate.

The fractional surface coverage θ is defined as the fraction of sites (n) that are occupied:

$$\theta = \frac{n}{n_{mono}}. \tag{3.3}$$

The rate, R_{ads}, of adsorbed molecules is proportional to the fraction of the surface which is not occupied (1 - θ) and to the rate R_s of striking molecules to the surface. R_s is defined as:

$$R_s = \frac{p}{\sqrt{2\pi mRT}} \tag{3.4}$$

where p is the vapor pressure at the equilibrium, m the molecular weight of the adsorptive, T the temperature and R the gas constant. Thus,

$$R_{ads} = k_{ads} \cdot R_s \cdot (1 - \theta) \tag{3.5}$$

where k_{ads} is the proportional constant.

Assuming constant temperature, the rate at which species desorb is proportional to the fraction of surface occupied by the adsorbate (θ):

$$R_{des} = k_{des} \cdot \theta. \tag{3.6}$$

At any temperature, the adsorbate and the surface come to a dynamic equilibrium. This means that the adsorption rate is equal to the desorption one. Then

$$\theta = \frac{K_L \cdot p}{1 + K_L \cdot p} \tag{3.7}$$

with the Langmuir parameter K_L defined as:

$$K_L = \frac{k_{ads}}{k_{des}} \cdot \frac{1}{\sqrt{2\pi mRT}}. \tag{3.8}$$

In the low pressure regime ($K_L\ p << 1$), the Langmuir equation reduces to the Henry isotherm:

$$\theta = K_L \cdot p \tag{3.9}$$

or, substituting θ in Eq 3.3, becomes:

$$n = n_{mono} \cdot K_L \cdot p = H \cdot p \tag{3.10}$$

where H is called *Henry's coefficient.*

Henry's coefficient depends on temperature as well as on the interaction energy ϕ (defined negative in case of attraction) of adsorbate molecules with the solid surface. Neglecting adsorbate-adsorbate interactions and treating all the molecules as spheres, we can assume the gas as ideal and in thermodynamic equilibrium with its adsorbate phase. Under these statements, the Henry coefficient can be expressed as:

$$H(T,\phi) = \frac{n}{p} = \frac{1}{p}\int_0^n dn = \frac{1}{RT}\int_0^{V_s}\left[exp\left(\frac{-\phi}{kT}\right) - 1\right] dV_s \tag{3.11}$$

where V_s is the specific volume element of the adsorbate and R and k the gas and the Boltzmann constants, respectively.

3.3.2 The BET model

The Langmuir model is an adequate approximation for uniform surfaces, however, it does not account for multilayer adsorbate growth. The BET model [78] is based on the same principles as the Langmuir model, but it also includes the possibility of multilayer adsorption. It assumes that only the first monoatomic layer is bound to the substrate surface. The first layer of adsorbate becomes then a site available for the second layer and the second layer of adsorbate is a site available for the third layer, and so forth (as shown in Figure 3.1). As for

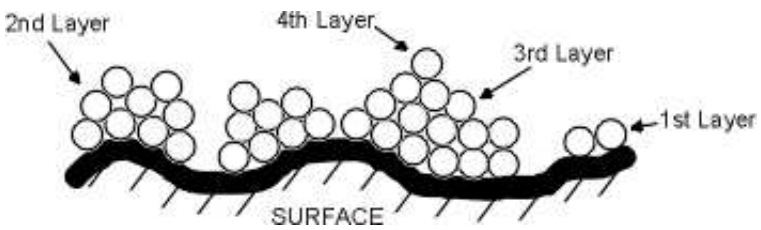

Figure 3.1: Multilayer adsorption on the surface.

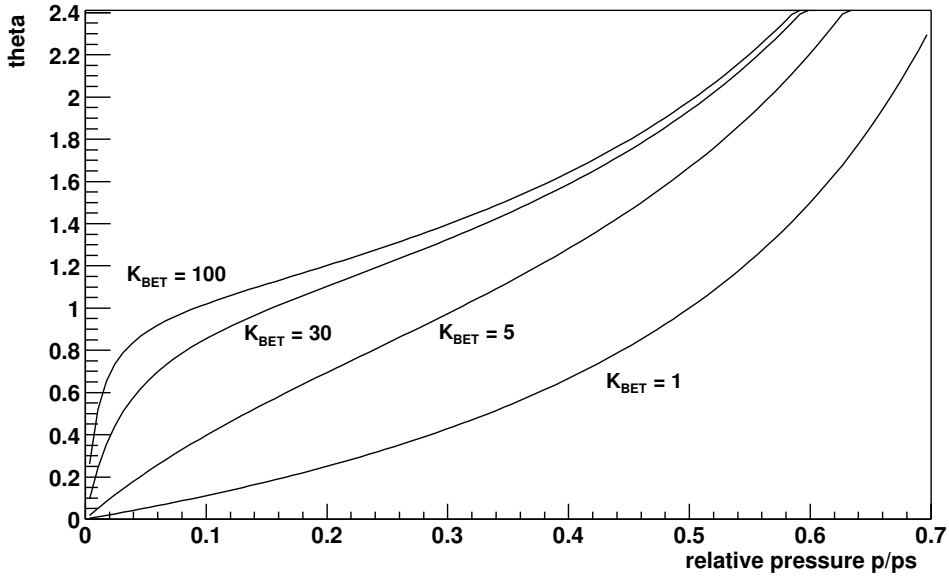

Figure 3.2: BET isotherm for different K_{BET} values.

the Langmuir model it is assumed that particles don't interact within the same layer. The BET isotherm has the form:

$$\theta = \frac{n}{n_{mono}} = \frac{\frac{p}{p_s}}{1 - \frac{p}{p_s}} \frac{K_{BET}}{1 + (K_{BET} - 1)\frac{p}{p_s}} \tag{3.12}$$

where p_s is the vapor pressure of the adsorptive at temperature T and K_{BET} is the BET constant (Figure 3.2).

The BET isotherm has an important application in the determination of the specific surface of the adsorbent (S_{BET}) [79]. The model, indeed, even if it fails to represent observations at low or high coverage, describes accurately the physisorption at intermediate coverage ($\theta = 0.8$ - 2.0). S_{BET} is derived measuring the number of molecules of adsorbate when $\theta = 1$ (n = n_{mono}):

$$S_{BET} = n_{mono} \cdot b \cdot N_a \tag{3.13}$$

where b is the cross section area of the adsorbate-adsorbent interaction and N_a is Avogadro's constant.

For a planar and energetically homogeneous solid surface, the specific volume element dV_s of the adsorbate may be expressed as:

$$dV_s = S_{BET}\, dz \tag{3.14}$$

where z is the distance from the surface. Substituting (3.14) in (3.11):

$$H(T,\phi) = \frac{S_{BET}}{RT}\int_0^{Z_{max}}\left[exp\left(\frac{-\phi(z)}{kT}\right)-1\right]dz, \tag{3.15}$$

with z_{max} depending on the solid structure: for a flat surface z_{max} goes to infinity and for a porous adsorber it is equal to the pore size. Equation (3.15) is theoretically exact only for monoatomic adsorbates.

W. A. Steele [81] has introduced a model predicting the potential *$\phi(z)$* for the adsorption of unpolar particles to an unpolar wall. The binding energy between the molecule and any atom of the adsorber is modeled by a Lennard-Jones-like potential:

$$\phi(z) = 2\rho\cdot\sigma^2\cdot\varepsilon\cdot\left[\frac{2}{5}\left(\frac{\sigma}{z}\right)^{10}-\left(\frac{\sigma}{z}\right)^4-\frac{\sigma^4}{3d(z+d\cdot p)^3}\right] \tag{3.16}$$

where ρ is the surface density of the adsorber atom, d the distance between the adsorber layers and p a correction parameter fitted from experimental data ($p = 0.61$). The parameters ϵ and σ are derived from the Lorentz-Berthelot rules:

$$\sigma = \frac{1}{2}\left(\sigma_{adsorber}+\sigma_{gas}\right) \tag{3.17}$$

$$\varepsilon = \sqrt{\varepsilon_{adsorber}\ \varepsilon_{gas}} \tag{3.18}$$

which mixes the Lennard-Jones energy well depths (ϵ_i) and molecule diameters (σ_i) of the adsorber and gas. The potential becomes negligible at large distances so that the adsorption is due only to the first atomic layers. The first two terms of Eq 3.16 are the repulsive and attractive energies related to the surface plane, while the third one describes the overall attractive interaction with the subsequent planes.

In case of porous adsorbers, the model can be extended assuming the pore as two opposing parallel walls at a distance b. The pore potential is thus a combination of the two wall potentials:

$$\phi_{pore}(z) = \phi(z+\frac{b}{2})+\phi(z-\frac{b}{2}). \tag{3.19}$$

and it has been calculated using parameters measured by [80] (reported in Table 3.2) for the krypton case on carbon-based adsorbers with different slit widths, as shown in Figure 3.3.

The Henry constant is derived substituting the Lennard-Jones-like potential in Eq 3.15. In Figure 3.4, H is derived for krypton, argon and nitrogen assuming T = 77 K and S_{BET} = 1000 m^2/g. These parameters represent a typical BET surface for activated carbon.

Even if the model is unable to provide the absolute value of the Henry constant in a multi-component systems, the comparison of H_{N_2} and H_{Ar} shows almost identical adsorption

Element	σ [$\dot{A}$]	ϵ [$10^{-22}J$]
Carbon	3.40	3.9
Argon	3.41	16.5
Krypton	3.60	23.6
Nitrogen	3.70	13.1

Table 3.2: Parameters for the Steele model of adsorption of nitrogen, argon and krypton on carbon based adsorbers in order to predict Henry's constant [80].

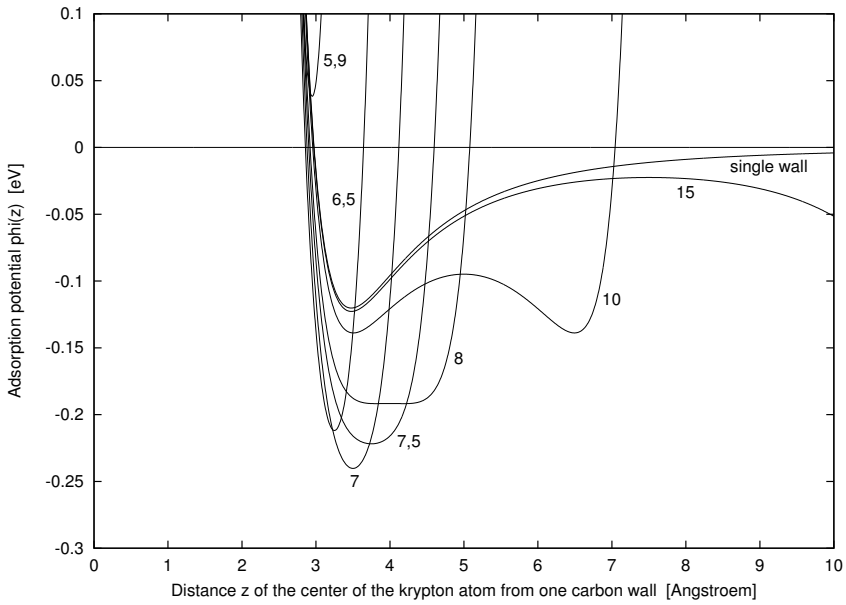

Figure 3.3: Adsorption Steele potential (3.16) of krypton in slit-like carbon pores for different pore widths (in angstrom) and for the case b $\rightarrow \infty$ (single wall). The parameters used for the Steele model are: $S_{BET} = 1000\ m^2$ (typical value for activated carbon), $T = 77$ K, $\rho = 3.81 \cdot 10^{19} m^{-2}$, $\varepsilon = 23.6 \cdot 10^{-22} J$ and $\sigma = 3.7\dot{A}$ (Table 3.2).

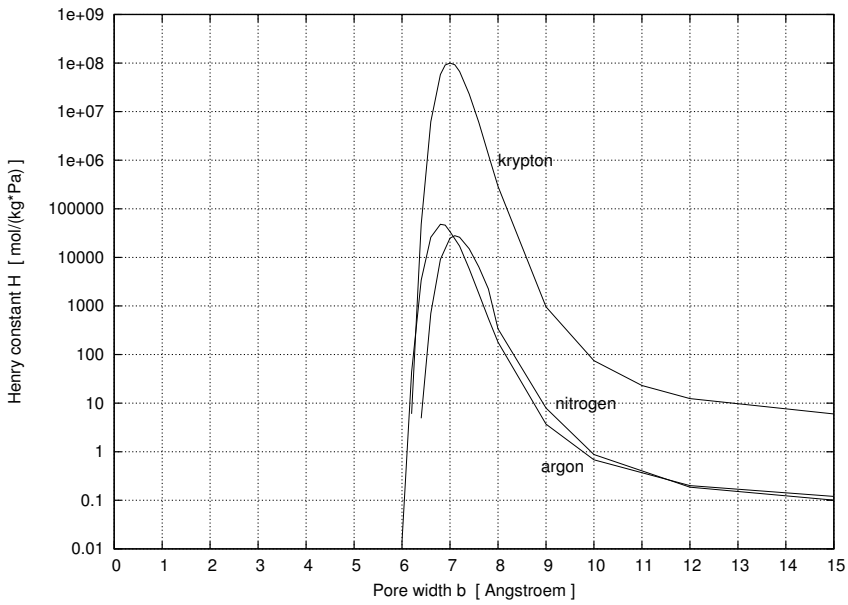

Figure 3.4: Henry constant (H) in single-component systems for argon, krypton and nitrogen in function of the pore width b. The similarity of $H_{N_2}$with H_{Ar} indicates clearly that adsorption process can not remove argon from nitrogen in a binary system while in the krypton case adsorption is possible thanks to a larger H_{Kr}.

behaviour. This is due to the similar dimensions of argon atom (mass number 40) and nitrogen bi-atomic molecule (mass number 28) which do not allow using the adsorption process to discriminate argon from nitrogen.

For the krypton case, instead, H_{Kr} is much larger than H_{N_2} (Figure 3.4) so that krypton adsorption in a binary krypton-nitrogen system is possible. The adsorber is suitable to the krypton adsorption if the pore structure is optimized for the krypton size and has no internal polarity. If the adsorber has a permanent internal polarity, indeed, the forces which induce the gas binding to the surface are twofold: the Van Der Waals (induced-dipole/induced-dipole) interaction and the stronger permanent-dipole/induced-dipole force which is proportional to the polarizability of the gas molecules. In general, poly-atomic gases have higher polarizability than mono-atomic ones and, as consequence, nitrogen has a higher probability to be adsorbed by the surface than krypton.

Eq 3.15 shows that Henry's constant increases when the temperature decreases. The low limit temperature depends on the liquification temperature of nitrogen. The gas phase has, in fact, two advantages compared to the liquid phase: high mobility of the adsorbate in the diffusion process to reach the adsorbent pore, and no attraction between adsorbate particles. The nitrogen temperature thus has been chosen a few degrees above the liquification temperature.

3.3.3 Chromatography

In gas chromatography, the carrier gas (in our case nitrogen) continuously flows through a column. The carrier gas transports the trace elements (contaminants) through the column, but this motion is inhibited by adsorption of the molecules onto packing materials in the column. The rate at which the molecules progress along the column depends on the strength of adsorption, which in turn depends on the type of molecule and on the column material. Since each type of molecule has a different rate of progression, the various components of the sample mixture are separated as they progress along the column and reach the end of the column at different times. The "plate model" gives a quantitative description of the efficiency of the column in gas separation.

The plate theory requires that the gas, when it passes through the adsorber in the column, is in equilibrium between the mobile and stationary phases. A global equilibrium between the phases never occurs in the entire volume. However, it is possible to assume a local equilibrium considering the column divided into a discrete number of plates N. The size of the plate (HETP, *Height Equivalent to a Theoretical Plate*) is chosen in order to provide sufficient residence time for the gas to establish equilibrium with the two phases:

$$HETP = \frac{L}{N}. \tag{3.20}$$

where L is the column length. Thus, decreasing the plate size, faster is the equilibrium and more plates are present in the column. Consequently, the number of theoretical plates contained in a column will be directly related to the equilibrium rate and so to the column efficiency in separating contaminants from the carrier gas.

The concentration (c_N) of the contaminants in the carrier gas at the end of the column depends on the retention volume, V_{ret} and on the number of plates N. It is defined as the volume of carrier gas admitted to the column between the injection of the sample and the emergence of the peak maximum of the contaminant. Assuming that the entering carrier gas has a constant concentration of contaminants c_0, c_N can be expressed as:

$$c_N(V) = c_0(1 - \sum_{r=0}^{N-1} \phi_r^{\frac{N \cdot V}{V_{ret}}}) = c_0 \sum_{r=N}^{\infty} \phi_r^{\frac{N \cdot V}{V_{ret}}}) \tag{3.21}$$

where

$$\phi_r^x = e^{-x} \cdot \frac{x^r}{r\,!} \tag{3.22}$$

is the Poisson distribution and V is the volume of the carrier gas passing through the column [82]. For $N \rightarrow \infty$,

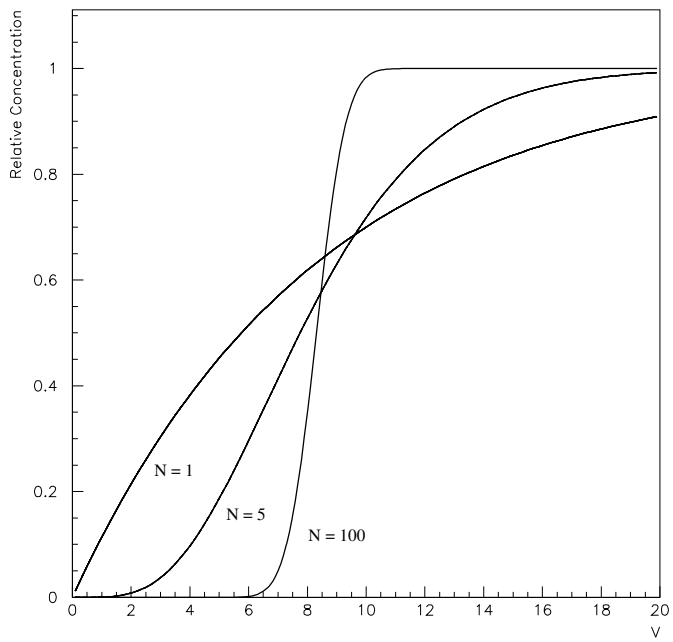

Figure 3.5: Behaviour of the relative concentration of the contaminant in the carrier gas versus the volume passing through the column (Eq 3.21 and 3.23) assuming V_{ret} constant

$$c_N(V) = c_0(1 - \frac{1}{\sqrt{2\pi}} \cdot \int_t^{\infty} e^{-\frac{y^2}{2}} dy) \tag{3.23}$$

with

$$t = \sqrt{N} \cdot (\frac{V}{V_{ret}} - 1). \tag{3.24}$$

Equations 3.21 and 3.23 are plotted in Figure 3.5 for different values of N. The plot emphasizes that a low number of theoretical plates implies an immediate "breakthrough" of the contaminant concentration. Increasing N, the column separation becomes more efficient maintaining the contamination low until a sudden and steep "breakthrough". For high N, the retention volume can be also defined as the volume of carrier gas where the concentration of a contaminant reaches the 50% of its initial value. In the law partial pressure regime, which corresponds to the Henry law region, the retention volume may be expressed as function of H:

$$V_{ret} = H \cdot R \cdot T \cdot m_{ads} \tag{3.25}$$

where R is the gas constant and m_{ads} is the mass of the adsorber in the column. Eq 3.25

provides the link between chromatography and adsorption capability.

Scanning experimentally the "breakthrough" curve in function of the carrier gas volume passing through the column, it is possible to characterize the adsorber and the column measuring Henry's constant H and the number of theoretical stages N (Figure 3.6).

3.3.4 Experimental setup

Nitrogen used to test the purification system was highly pure liquid nitrogen artificially doped by the supplier (Westfalen AG) up to 400 ppt of krypton. This gave us a high dynamic range in the mass spectrometric observation of the Kr reduction factor for each investigated adsorption method. As shown in Figure 3.7, nitrogen, once evaporated, flows through a cold trap filled with the adsorber we want to investigate. As already observed from the BET theoretical model, the purification efficiency increases if nitrogen is kept at the lowest temperature above the liquification point. For studying the dynamic purification, nitrogen samples are stored in time sequence in four pipettes. For each pipette, a getter pump removes nitrogen and reactive trace contaminants from the samples. Finally, an aliquot of residual noble gases is transferred to the spectrometer and analysed.

The volume (30, 100, 300 cm^3) of the cold-traps used in the system varies in function of the different shape and density of the adsorbers. Sintered metal filters enclose the adsorber in the trap and a 3 nm teflon filter protects the spectrometer from adsorber debris.

Before starting each measurement, all the lines and the adsorber are baked out for 2-3 days at T $\sim$ 200 °C whit permanent nitrogen flow, in order to remove all the contaminants released from the surfaces. After that, the krypton concentration is measured twice: when nitrogen is flowed through the heated trap and through its by-pass (blank test). The trap is assumed to be sufficiently purified if there is agreement between the two measurements. If this condition is fulfilled, the adsorption test can start and a cryogenic bath cools down the trap. The nitrogen is led through it with a constant flow rate (between 120 and 250 l/h) depending on the trap and on the the adsorber. A nitrogen sample is stored, and then measured, in a pipette every 3 hours in order to scan the profile of the breakthrough curve. At the end of the run, a new blank test is performed and results are compared with ones at the beginning of the run.

3.3.5 Tested adsorber and results

The investigated carbon-based and zeolite adsorbers (and their main properties) are listed in Table 3.3 .

To purify krypton, as already mentioned, we need unpolar adsorbers with a relative large pore size of the same order of magnitude of the krypton atom dimension. Zeolites are usually strongly polar since they are composed in a large fraction of aluminium. Aluminium is required to stabilize structures with large pore channels. A sub-class of zeolites, the so-called

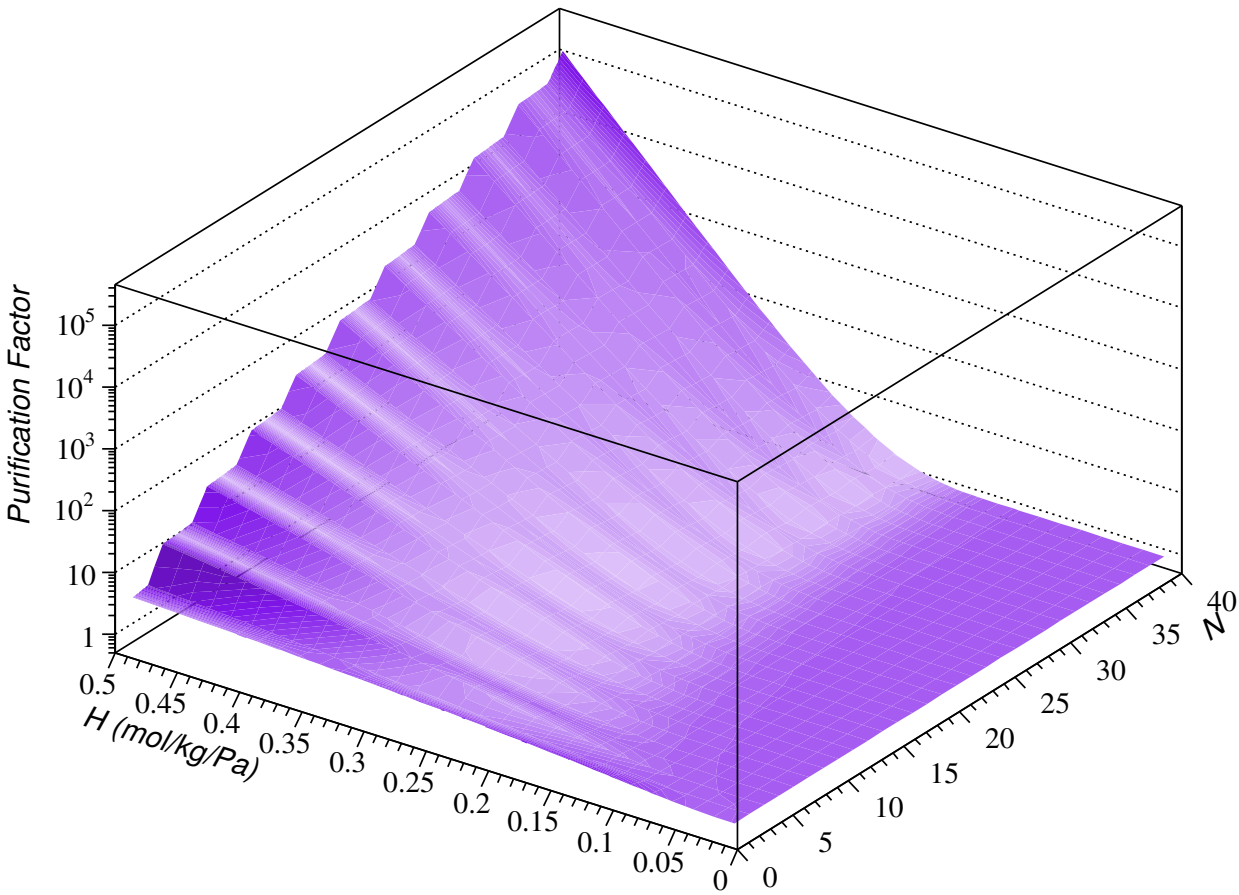

Figure 3.6: Nitrogen purification factor from krypton as function of H and N (Eq 3.21) after a volume of 2000 m^3 flowed in a trap filled with m_{ads} = 12 kg at temperature T = 98 K (Borexino-like conditions for 3-4 days of continuous purification at the rate of 30 m^3/h).

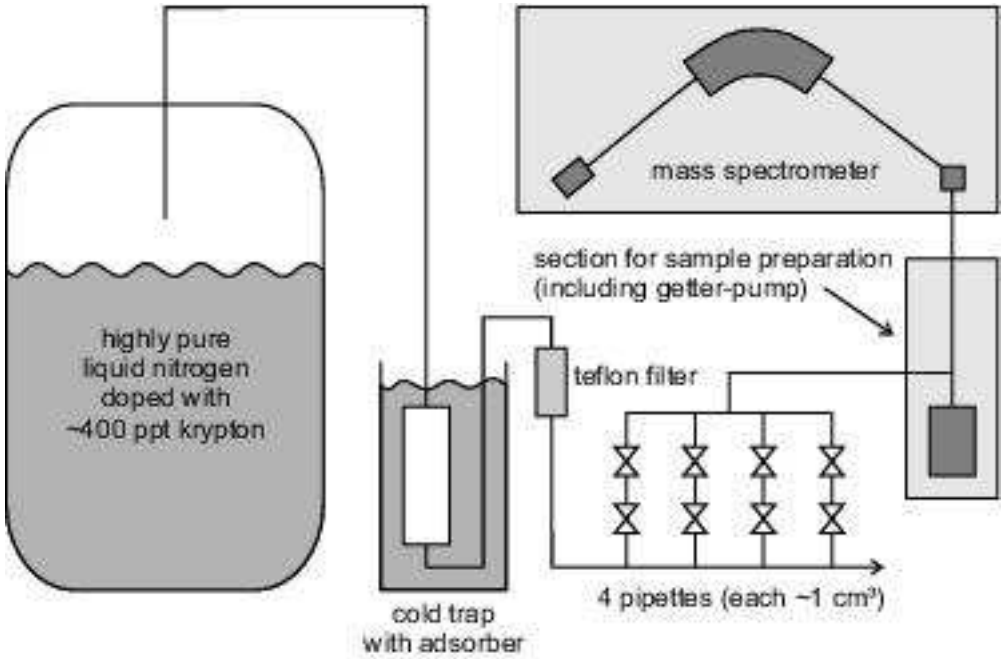

Figure 3.7: Sketch of the experimental setup for nitrogen purification.

hydrophobic zeolites, are depleted in aluminium and thus have a smaller polarity but also a very small pore structure.

The zeolites we have investigated have a very low aluminium concentration. The Si/Al ratio for the MFI adsorber is ~ 200 while for the Zeocat BEA is ~ 70. The polarity is than highly reduced but the pore size is smaller than 7 $\dot{A}$. However, a krypton atom has a diameter around 7.3 $\dot{A}$. We have tested zeolites cooling the trap at LN_2 temperature, observing, as expected, a very little (if any) ability to remove krypton from nitrogen (Figure 3.8). For both zeolites, the measured Henry's constant is only $6 \cdot 10^{-3}$mol/kg/Pa as reported in Table 3.4. The measurements on the zeolites suggest that the pore size distribution plays a relevant role in the krypton adsorption. Since it is not possible to produce zeolites with a pore size bigger than the krypton atom, we decided to focus our efforts only on the carbon-based adsorbers which are free of internal polarity and can have a wide range of pore size distribution.

CarboAct F3/F4 has been successfully used in the radon removal from nitrogen at LN_2 temperature. It is characterized by a very low ^{226}Ra contamination, corresponding to a ^{222}Rn emanation rate of (0.3 ± 0.1) mBq/kg. Its pore size distribution is wide, typical of the "standard" activated carbons. C38/2 is frequently used for solvent recovery. According to the manufacturer, it is classifiable as a "standard" activated carbon but with a larger fraction of pores around 7$\dot{A}$. Also FM 1-250 has a significant pore fraction in the range of 7$\dot{A}$, however the peak is around 20 $\dot{A}$. It is fabric made, therefore the trap may not be homogeneously filled up. Carbosieve SIII is a product with a narrow pore size distribution between 10 and

40 $\dot{A}$. It is mainly used for trapping volatile organic compounds.

Figures 3.8 and 3.9 shows the breakthrough curves, normalized for m_{ads}, for each adsorber, at LN_2 and LAr temperatures, respectively. The curves are obtained fitting with Eq 3.21 and 3.23 the measured relative concentration of krypton as function of the purified nitrogen volume.

The results, summarized in Tables 3.4 and 3.5, emphasise an increasing of the purification efficiency when the trap is cooled with LAr. Nitrogen gas, indeed, passing through the trap cooled in LN_2 partly liquefies and covers the adsorber surface. Some pores therefore can be obstructed and trace contaminants like krypton have an enhanced probability to be not adsorbed. Moreover, also the mobility of krypton in LN_2, much smaller than in gaseous phase, contributes to a loss of purification efficiency.

However, as already mentioned describing the theoretical model, the adsorption process increases at the decreasing of the temperature. Cooling with LAr (87 K at standard conditions) avoids the liquification of nitrogen in the trap, and, at the same time, guarantees a still enough low temperature. The Henry constants obtained in the pure gas phase adsorption are, in fact, significantly larger for all tested adsorbers. The theoretical model predicted that H is expected to be significantly smaller at $\sim$ 10 K higher temperature (see Eq 3.15). The krypton mobility in the gas phase compensates this effect. This confirms that when liquid nitrogen is present inside the trap, krypton can not reach the pore and the adsorption efficiency is drastically reduced. Also the *HETP* is higher in the gas phase and therefore the breakthrough curves are steeper. The only exception is Cloth FM 1-250, which suggests that the fabric behaves different than grains.

The results accentuate the importance of the pore size distribution in the adsorption process. Zeolites have pore sizes too small compare to the krypton atoms and are not able to purify nitrogen from Kr. The "standard" activated carbons, with a wide range of pore sizes, have very similar retention ability while Carbosieve SIII, which has a very narrow distribution close to krypton atom size, is the most efficient.

The statistics error provided by the mass spectrometer is of the order of magnitude of 1/10000. The error of the measurement results is dominated by systematic effects we have not already derived.

The lower limits of the maximum purification factors that carbon-based adsorbers can reach are reported in Table 3.6. In gas phase, purification factors increase for each carbon-based adsorber. All the adsorbers has reached the factor ($\sim$ 50) we expect to require. The criterion for choosing the best adsorber depends on the time it is able to maintain the maximum purification factor.

The best candidate for Borexino is the Carbosieve SIII. Borexino requires a continuous supply of krypton-free nitrogen at a flow rate of 30 m^3/h. A column filled with 12 kg of Carbosieve SIII can be operative for 3-4 days (Figure 3.10). After that time, the adsorber is no larger able to purify and has to be cleaned. A second identical column should thus be

Product	***F3/F4***	***C38/2***	***FM 1-250***	***Carbosieve SIII***	***Zeocat BEA***	***Zeolite MFI***
Company	CarbonAct	CarboTech	Charcoal Cloth Int.	Supelco	Zeochem	Sud-chemie Muenchen
Type	Carbon	Carbon	Carbon	Carbon	Zeolite	Zeolite
Pore-size distribution	unknown	wide peaked in 7$\dot{A}$	wide peaked in 20$\dot{A}$	narrow 15 - 40 $\dot{A}$	6.6 $\dot{A}$	5.3 $\dot{A}$
Shape	grains	pressed cylinders	fabric	grains	powder	pressed cylinder
Size	0.85 - 2.8 mm	L: 2-7 mm D: 2 mm	Thickness 1.2-1.4 mm	60-80 μm	0.1-0.5 mm	L: 5 mm D: 1 mm
Density	0.1 g/cm^3	0.65 g/cm^3	210 g/m^2	0.61 g/cm^3	0.56 g/cm^3	0.47 g/cm^3
Surface area	1200 m^2/g	1300 m^2/g	1000-1200 m^2/g	820 m^2/g	unknown	unknown

Table 3.3: Main properties of the investigated carbon-based and zeolite adsorbers. The first three products are "standard" activated carbons with a wide pore size distributions. Carbosieve III has a narrow distribution around the krypton atom dimension. The two zeolites have pore size slightly smaller then the krypton atom size.

operative in order to assure the purification phase while the first column is backing out. 24 kg of adsorber would be needed for guarantee a continuous supply of purified nitrogen. Such device is an optimal candidate for the krypton removal in Borexino. However, it does not solve the argon problem. The mass spectrometer, indeed, measures simultaneously krypton and argon concentrations. As expected, argon is almost totally unaffected by the carbon-based adsorption process. A further investigation on commercially available Ar and Kr free nitrogen is described in the next section.

3.4 Investigation of Ar and Kr in commercially available nitrogen

The contamination of nitrogen by noble gases can occurs in two ways: during the production and during the delivery. During the fractional distillation process, nitrogen can be extracted from the fractionating column at different levels. It depends on the required level of purity. The contamination level N is defined as

$$N = -Log_{10}\frac{m_{impurities}}{m_{nitrogen}}. \tag{3.26}$$

The most pure availably nitrogen is level-7.0 which corresponds to 0.1 ppm of contamination concentration. In this limit are considered contaminants like O_2, CO_2 but usually

Adsorber	HETP [mm]	H [10^{-2} mol/Pa/kg]	V_{ret}/m_{ads} [m^3/kg]	Number of stages
F3/F4	275	2.4	17	1
C38/2	34	1.6	12	8
FM 1-250	21	2.9	21	13
Carbosieve SIII	110	8.3	60	2
Zeocat BEA	69	0.6	5	4
Zeolite MFI	275	0.6	5	1

Table 3.4: Results from the krypton adsorption from nitrogen for different carbon-based adsorbers cooled by LN_2.

Adsorber	HETP [mm]	H [10^{-2} mol/Pa/kg]	V_{ret}/m_{ads} [m^3/kg]	Number of stages
F3/F4	15	21	183	6
C38/2	17	19	158	13
FM 1-250	24	16	125	7
Carbosieve SIII	10	34	282	27

Table 3.5: Results from the krypton adsorption from nitrogen for different carbon-based adsorbers cooled by LAr. Statistical errors are of the order of magnitude of 1/1000. The systematics have to be studied.

Carbon-based adsorber	Cooling media	
	LN_2	***LAr***
F3/F4	> 3	> 96
C38/2	> 12	> 1768
FM 1-250	> 18	> 1982
Carbosieve III	> 59	> 98

Table 3.6: Purification factor low limits for carbon-based adsorbers. They have been measured cooling the trap with LN_2 and LAr. Statistical errors are of the order of magnitude of 1/1000. Systematics have to be studied.

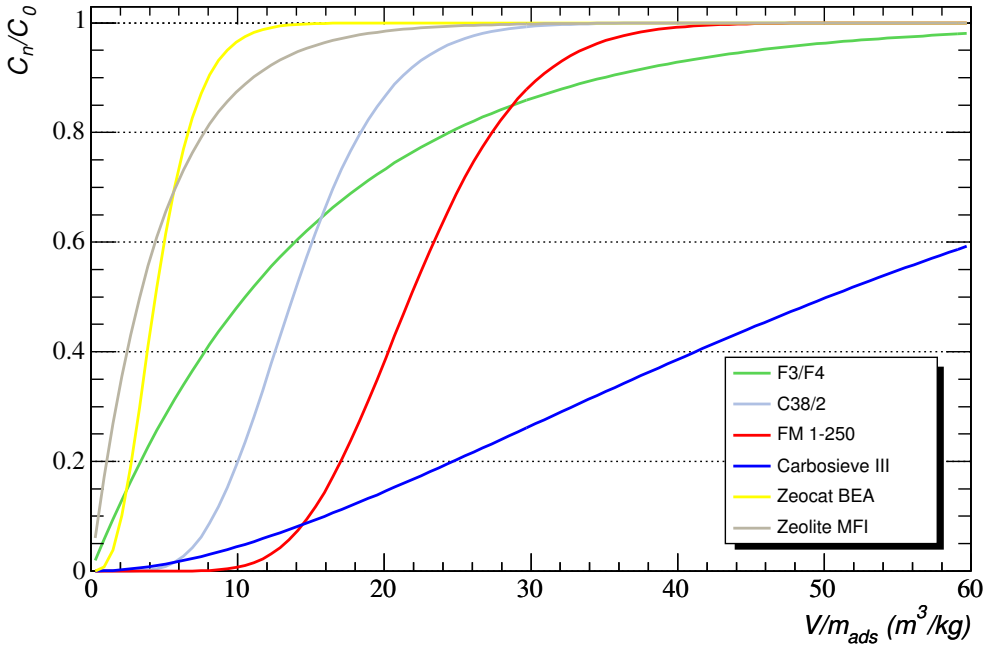

Figure 3.8: Measured breakthrough curves for krypton adsorption from nitrogen on different carbon-based and zeolite adsorbers cooled by LN_2.

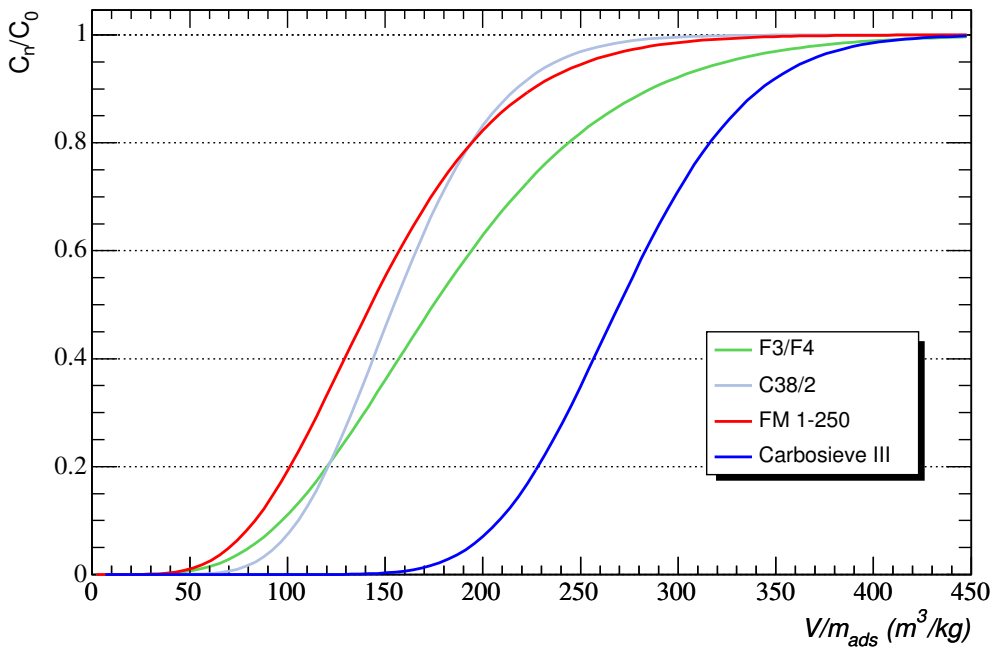

Figure 3.9: Measured breakthrough curves for krypton adsorption from nitrogen on different carbon-based adsorbers cooled by LAr.

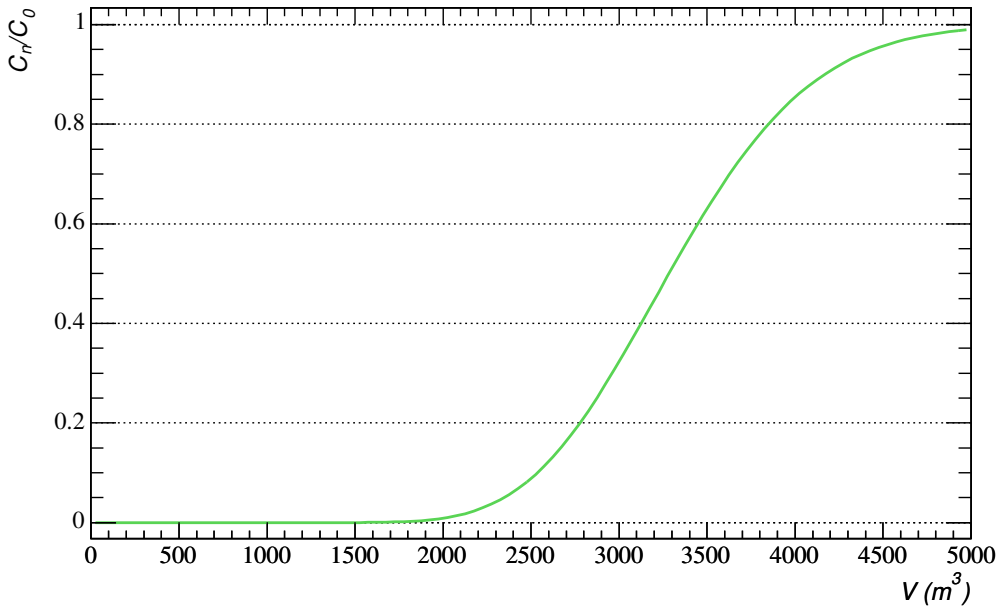

Figure 3.10: Nitrogen purification of krypton with the Carbosieve SIII adsorber (12 kg of adsorber, n = 27 and H = 0.34 mol/kg/Pa). It can purify more than 2000 m^3 of nitrogen by a factor 50. In Borexino we required an adsorber able to purify a continuous flow rate of 30 m^3/h for 3-4 days ($>$ 2000 m^3) with a factor $>$ 50.

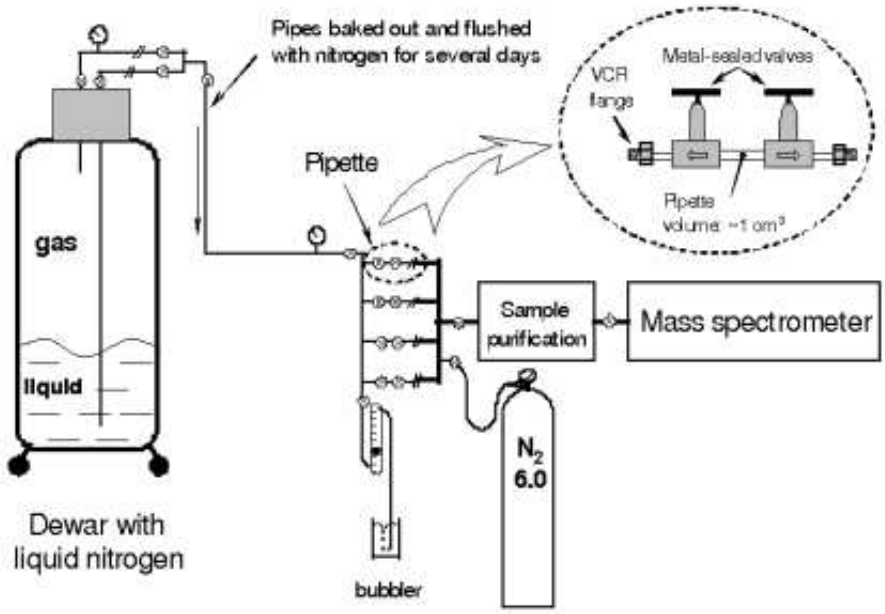

Figure 3.11: Liquid sample container connected to the sample preparation section of the mass spectrometer.

suppliers don't take into account the presence of noble gases. On the other hand, the pouring of nitrogen, for instance into the transportation tank, has a certain risk to introduce air contamination. Companies, generally, don't give detailed information about presence of noble gases because they are not able to measure at such low levels.

We investigated mainly on level-6.0 and level-7.0 nitrogen samples from German and Italian suppliers. We analyzed also the nitrogen used in standard activities at the Heidelberg Max Planck Institute and at the Gran Sasso Lab (both level-4.0 nitrogen)

Liquid samples of 180-600 l volume are collected directly at the production plant. This minimizes interference with air contamination and enables to reproduce the same conditions in several tests.

We do not use container tanks with pressure built-up systems. They are difficult to be purified from atmospheric contamination prior to the liquid nitrogen filling: flushing with nitrogen does not guarantee the impurity removal inside the pressure build-up system.

The liquid container is connected to the sample preparation section of the spectrometer as shown in Figure 3.11. The sample is introduced in the sample section once evaporated from the liquid phase. After a flushing period of several days, an aliquot of nitrogen sample is enclosed in one of the pipettes with known volume. The sample is released into the purification sector when vacuum behind the pipette has reached its nominal value of about 10^{-9} mbar. Before removing the nitrogen from the sample through the getter pump, we measure the pressure in

Nitrogen supplier	Ar (ppm)	Kr (ppt)
MESSER regular purity nitrogen (4.0)	200 ± 30	1680 ± 240
Air Liquide regular purity nitrogen (4.0)	11.0 ± 1.3	40± 5
Air Liquide high purity nitrogen (4.0)	10.4 ± 1.2	33 ± 4
Linde AG, Worms (7.0)	$(3.1\pm 0.4)\cdot 10^{-2}$	2.9 ± 0.4
SOL Mantova (6.0)	0.22 ± 0.03	8.8 ± 1.3
SOL Mantova (6.0 or better)	$(6.3 \pm 0.6)\cdot 10^{-3}$	$(4.0 \pm 1.0)\cdot 10^{-2}$
Westfalen AG, Hoerstel (6.0)	$(5.2 \pm 0.7)\cdot 10^{-3}$	5.2 ± 0.8
Westfalen AG, Hoerstel (6.0 or better)	$(5.0\pm 0.8)\cdot 10^{-4}$	$(6.0 \pm 2.0)\cdot 10^{-2}$
Goal	< 0.36	< 0.14

Table 3.7: Results of the analyzed commercial nitrogen. The first two samples are relative to nitrogen normally used at the MPI and LNGS, respectively. The samples from the same supplier differ in the procedure of filling the container tank.

Linde AG Nitrogen (7.0)	Ar (ppm)	Kr (ppt)
Gas Phase	$(7.0 \pm 0.7)\cdot 10^{-3}$	$(3 \pm 1)\cdot 10^{-2}$
Liquid Phase	$(13.2 \pm 1.3)\cdot 10^{-3}$	$(10 \pm 2)\cdot 10^{-2}$
~ 1.4 m^3 of LN_2 left in the tank	$(12.2 \pm 1.7)\cdot 10^{-3}$	$(5 \pm 1)\cdot 10^{-2}$
~ 0.3 m^3 of LN_2 left in the tank	$(17.5 \pm 2.4)\cdot 10^{-3}$	$(6 \pm 1)\cdot 10^{-2}$
only gas in the tank	$(19.4 \pm 1.8)\cdot 10^{-3}$	$(11 \pm 2)\cdot 10^{-2}$
Goal	< 0.36	< 0.14

Table 3.8: Results of a more accurate study on the Linde AG Nitrogen.

order to derive the total volume of the aliquot. Once the nitrogen is completely adsorbed, the remaining rare gases are transferred into the mass spectrometer and analyzed.

The obtained results for Ar and Kr concentrations are reported in Table 3.7. For two companies, SOL Mantova and Westfalen AG, we asked for a second sample with a different filling procedure. We realized that filling the container tank using pumps introduces a larger amount of contaminants respect to fill exploiting only the pressure difference.

The candidate who better fulfils the requirements of Borexino, concerning purity and cost, is Linde AG. However, since the level of krypton is over the requested limit, we need more accurate tests. In Borexino, the nitrogen is taken directly from the air separator plant by truck, carried to LNGS and poured into a storage tank. In order to reproduce similar conditions, we rented a mobile storage tank (6 m^3) with an integrated atmospheric evaporator from Linde AG, filled with level-7.0 nitrogen (same nitrogen already measured, whose results are reported in Table 3.7). Both the tank and the truck are subjected to stringent cleanliness requirements (only SS tubing and bellow SS valves, mostly electropolished, etc.).

We tested the purity of nitrogen in gas and liquid phases as function of the remaining volume of LN_2 in the tank. For the liquid phase test, a small dewar of 240 l has been filled and connected directly to the mass spectrometer. For the gas phase, the storage tank has been

connected to the mass spectrometer by a 60 m long copper tube (6 mm diameter). During the Ar and Kr measurement, we checked also the concentration level of radon which was always below the requirement of Borexino ($\sim$ 7 μBq/m^3) by a factor $\sim$7, apart when only gas is present in the tank (32 $\pm$ 2 μBq/m^3). The results for Ar and Kr for the last measurements reported in Table 3.8, shows a clear improvement in nitrogen purity by a factor $\sim$ 4 for Ar and $\sim$ 100 for Kr.

3.5 Conclusions

From the last measurements, we can claim that it is possible to achieve high purity commercial nitrogen and maintain its quality for a delivery "path" foreseen for the Borexino experiment. Ar and Kr concentration levels are always below the required limits even if the amount of the liquid nitrogen in the tank decreases. Some radon is probably frozen to the walls of the tank and released when the tank is almost empty. This could explain the high concentration when the tank is filled only with gas.

The Ar and Kr concentration obtained for the gas evaporated directly from the tank is slightly lower than corresponding results for the liquid phase from the small dewar. In the second case, the filling of the dewar can alter the nitrogen sample introducing a small amount of contamination. However, the effect is negligible for the Borexino purposes.

Kr purification by carbon-based adsorption has been tested successfully. We identified a carbon-based adsorber, Carbosieve III, able to reach to required purification factor. Moreover, we have verified qualitatively the BET model, emphasizing the relevance of the adsorber pore size distribution in the adsorption process. However, we confirm also our theoretical expectation that adsorption is inadequate in removing argon from nitrogen.

A further problem is related to the implementation of an adsorption column in the Borexino purification system. In this case we should install a system able to automatically switch between two columns: while the first is purifying, the second must be recovered. However, such modification is expansive, is time consuming and requires major modification of the nitrogen plant.

Taking into account all these considerations, the Borexino collaboration has indeed opted for the second solution: acquiring available commercial pure nitrogen.

Chapter 4

The Counting Test Facility

When Borexino was proposed, direct radiopurity measurements in scintillators were possible only for small samples and without the required sensitivity for the solar neutrino detection. The Counting Test Facility (CTF) is a Borexino detector prototype designed to verify experimentally the required purity of the organic liquid scintillator. Furthermore, several Borexino devices have been tested and optimized in the CTF detector. CTF was specifically projected to achieve the following goals:

- measurement of the ^{238}U and ^{232}Th contamination in the liquid scintillator with an upper limit of 5x10^{-16} g/g;
- measurement of the K_{nat} contamination in the liquid scintillator with an upper limit of 10^{-13} g/g;
- measurement of the ^{14}C contamination in the liquid scintillator with an upper limit of 10^{-18} for the relative concentration ^{14}C /^{12}C;
- radioactivity screening of the construction materials;
- test of the purification system of scintillator and buffer fluids;
- determination of the scintillator optical properties;
- implementation of cleaning methods during construction and installation of the detector and of the auxiliary plants.

The limited dimensions of the CTF do not allow us to define a fiducial volume or to measure the total internal counting rate at the level of ^{7}Be neutrino interactions (0.5 counts/day/ton). Nevertheless, during the running of CTF we developed analysis techniques to study the total background rate, overcoming as much as possible the lack of a fiducial volume definition. Exploiting the spatial reconstruction of the events, these techniques allowed the collaboration to push the CTF sensitivity to 15 times the neutrino interaction rate.

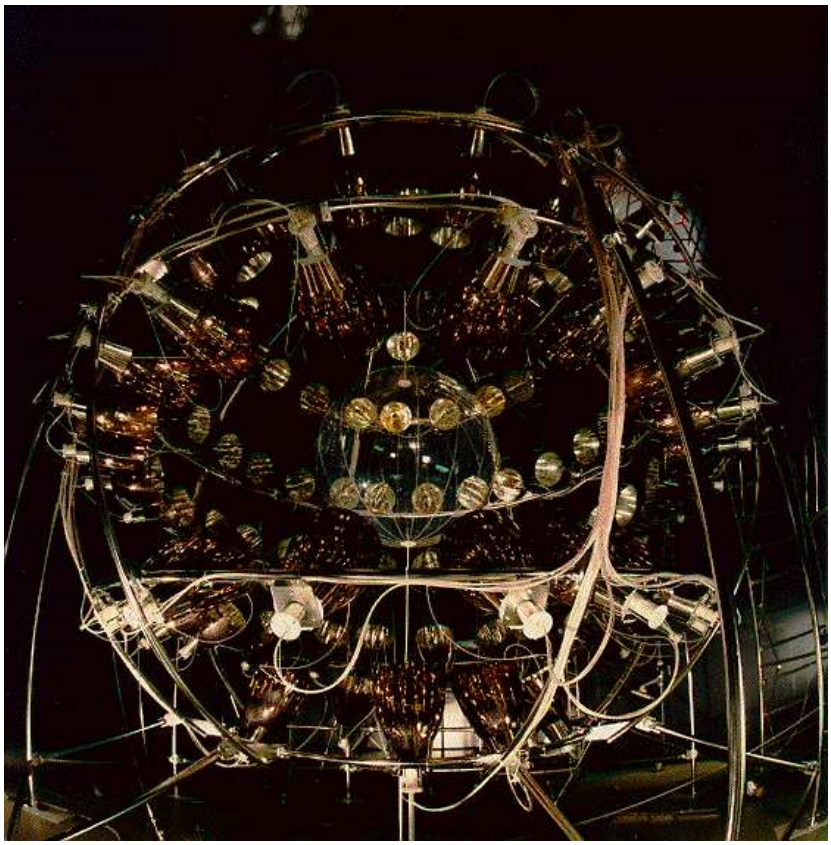

Figure 4.1: The open structure and the inner vessel of CTF.

The CTF installation began in 1993. The water shielding tank was filled in January 1995, and the scintillator was introduced for the first time in February 1995.

Until the present date, three campaigns of data taking have been performed. The first one known as CTF-1 ran until 1997 and focused on radioactive impurities in the scintillator material (PC+PPO) and on its optical response. CTF-2 ran from June to September 2000, testing a PXE-based scintillator (phenyl-o-xylylethane), characterized by a density close to that of water and a flash point of 145°C. The last campaign (CTF3), started at the end of 2001 and still ongoing, and it is intended to prove the efficiency of the on-line systems for purifying the PC-PPO scintillator.

4.1 The structure of the detector

The CTF detector structure is similar to Borexino. The active detector consists of $\sim$ 4 tons of the Borexino-like PC+PPO scintillator immersed in 1000 tons of pure water and viewed by an array of 100 Thorn EMI 9351 photomultipliers (same as in Borexino). An open structure of stainless steel tubes supports the PMT's (Figure 4.1). CTF differs from Borexino for the

lack of the PC buffer liquid and stainless steel sphere.

The external tank is a 10 m tall carbon steel cylinder, with 11 m diameter. Its internal walls are coated with Permatex, a black epoxy resin.

The scintillator is contained in a 0.5 mm thick nylon vessel (~1 m radius). The scintillator containment vessel confines the scintillator within the water buffer. Being in direct contact with water and scintillator simultaneously, the vessel must be chemically compatible with water and aromatic solvents as well. The vessel sustains the 570 kg buoyant force associated with the 12% density difference between pseudocumene and water; it must be optically transparent to transmit the scintillation light.

Given the larger surface/volume ratio, under certain aspects CTF is actually a more delicate experiment than Borexino, since the inner vessel surface contamination is a more critical issue and the water purity requirements are higher.

The ultra-pure water provides the equivalent of 4.5 m water shielding from the γ-rays on all sides, mainly from the rocks of the Hall C. The dominant γ-rays are emitted by ^{208}Tl (E_γ = 2.6 MeV). Since the minimum path in water is 4.5 m and the absorption length for the 2.6 MeV γ rays in water is 20 cm, the minimum reduction factor achieved by the buffer is 10^{-9}. In order to shield also the γ-rays flux from the phototubes (approximately 2% of the total flux) PMT's are moved 2.3 m away from the scintillator.

The PMT's are coupled to "truncated string cone" light concentrators which improves the light collection. They are 57 cm long and 50 cm diameter aperture, reaching the 20% of the total optical coverage.

After the first data campaign, 20 PMT's were placed on the bottom of the water tank to detect Cerenkov light produced by muons. Moreover, a second nylon membrane, as a Rn barrier, was deployed between the inner vessel and the PMT's (Figure 4.2).

4.2 Data acquisition electronics

The 100 PMT outputs are processed in 64 electronics channel: 28 linked to a single phototube and 72 PMT's are fanned together in pairs into 36 channels and added together. Each PMT assembly is equipped with a light guide which can be simultaneously triggered by a single laser pulse. Synchronizing on the rise time of the pulse allows to calibrate the transmission times with an accuracy of 1 ns.

For each channel, an ADC collects and digitizes the charge signal and a TDC measures the time between the trigger and the signal hit (the so-called "group 1" chain). The trigger signal is given by 6 photomultiplier hits within a time window of 20 ns which corresponds to a low-energy threshold of 25 keV. The ADC gate remains opened for 500 ns charge integration time. The total charge of an event is derived integrating the 64-fold analog sum for 500 ns after the trigger. The ratio between the integrated long time "tail" (32 - 500 ns) and the total

Figure 4.2: The inner and outer vessels in the CTF open structure.

integrated charge is used for discriminating α and β events.

The event trigger also starts a second separated TDC clock: if a second event occurs within 8 ms, it is processed through a second set of ADC's and long range TDC's ("group 2" chain). This feature allows the identification of the delayed coincidences such as ^{214}Bi-^{214}Po in the ^{238}U chain and ^{212}Bi-^{212}Po in the ^{232}Th. An exhaustive description of the CTF DAQ can be found in [50].

4.3 Achieved results

In the first data taking campaign (CTF-1) several promising results have been achieved in view of Borexino. I will summarize here only the main goals. A more detailed description can be found in [50, 87, 88, 91].

- The light yield in CTF-1 is equal to $\sim$ 300 photoelectrons per MeV, which corresponds to an energy resolution of 9% at 751 keV (^{214}Po) and, at the same energy, a spatial resolution of 12 cm.
- The α/β discrimination rejects α events with an efficiency of $\sim$ 97% and with $\sim$ 2.5% of β misidentification, at the ^{214}Po energy. At lower energy (300-600 keV), the α identification efficiency can decrease down to 90%, while β misidentification increases up to 10%.

- Several measurements have been carried out to investigate the main characteristics of the light propagation. Among them, the absorption and re-emission of light by the fluor (inelastic scattering) plays a crucial role because it involves $\sim 44\%$ of the detected light. The scintillation decay time, consequently, increases from the 3.5 ns measured in laboratory with a small-scale sample to 5.5 ns measured in CTF.

- The scintillator showed an intrinsic activity for ^{238}U and ^{232}Th at a level consistent with or below 5x10^{-16} g/g in PC and a ^{14}C/^{12}C ratio of about 10^{-18}.

- The purification techniques adopted were water extraction, nitrogen stripping and vacuum distillation. After the purifications, internal background decreased from $\sim$ 6000 events per day down to less than 30 per day. In particular, the nitrogen stripping purification reduced the ^{85}Kr activity (identified by the coincidence technique) from 1.1 ± 0.2 to 0.2 ± 0.2 ev/day.

The main source of background in CTF-1 after the purification phases, was identified as the ^{222}Rn concentration in the water shield, measured at the levels of 10 - 30 mBq/m^3. Such a concentration can be explained by ^{222}Rn diffusion through the nylon vessel and into the scintillator, at the level consistent with the measured ^{214}Bi-^{214}Po coincidence rate.

A second problem arisen in the CTF-1 campaign is related to the γs emitted by ^{222}Rn in water, which dominates the energy spectrum.

In the CTF-2 phase, a second nylon screen was installed between the scintillator vessel and the phototubes. This second vessel acts as a barrier against the ^{222}Rn that diffuses and emanates from the various detector components (Figure 4.2).

A second major upgrade consists in 20 PMT's placed on the bottom of the water tank to detect Cerenkov light produced by muons. The muon-veto efficiency is $\sim 100\%$,

CTF-2 tested a different scintillator: phenyl-ortho-xylylethane (PXE) as a solvent with para-Terphenyl (2 g/l) and bis-MSB (20 mg/l) as wavelength shifters. A complete description of the characteristics of PXE measured in CTF-2 can be found in reference [67]. Several analyses have been performed with CTF-2 putting new lower limits on the lifetime of some interesting non-standard processes [92, 93].

Chapter 5

Analysis of the CTF-3 data

The third campaign of the Counting Test Facility (CTF) has been devoted to measure the initial contamination of the scintillator from trace radioactive isotopes, like ^{238}U, ^{232}Th, ^{85}Kr and specifically to test the ^{14}C content of the Borexino scintillator delivery. Moreover, CTF evaluated the efficiency of the scintillator purification techniques for Borexino.

In this chapter I provide a detailed description of the analyses and of the results concerning the last three years of data taking.

5.1 The data-campaign

The third data-taking campaign started in May 2001 when the vessel was filled with water. During this phase, the electronics was commissioned and calibrated. At the end of November, CTF was filled with scintillator from the first pseudocumene batch delivered for Borexino. In the following 7 months, we performed purification tests and measurements of the intrinsic contamination of the scintillator:

- *^{14}C test.* The delivering of pseudocumene from the manufacturer (Enichem) to LNGS, follows standard procedures in agreement with the Borexino strict cleanliness requirements. Nevertheless, petroleum used in the pseudocumene production can have different origins and thus different ^{14}C contamination. In order to measure the intrinsic ^{14}C activity in the PC in all the delivered batches, a few hundreds liters of scintillator was removed from the CTF inner vessel and replaced with pure PC coming from the Enichem plant. This implied a decreasing of the PPO concentration in the scintillator.

- *Water extraction purification.* The water extraction purification (WE) has been applied twice. In the first WE, scintillator was purified in a continuous loop mode. In this phase, scintillator was also stripped of argon and krypton with nitrogen. In the second purification phase, nitric acid was added in order to improve the purification efficiency. In fact, a lower pH is expected to increase the possibility to capture ions in water.

Date	Runs	Operation	comments
2001 Feb		nylon vessel installed	
2001 May		water filling	
2001 Jul 21	2000	beginning of data taking	water runs
2001 Nov 22-28	2042-2047	scintillator loading	
2002 Jan 10-11	2074-2075	^{14}C test	
2002 Feb 6-11	2094-2103	silica gel column test	continuous loop mode
2002 Mar 20-28	2123-2130	water extraction test	continuous loop mode
2002 Apr 2	2150-2152	blank loop	
2002 Apr 26	2153	^{14}C test	
2002 May 9-23	2162-2173	water extraction	stop-and-go mode, acidic water
2002 Jun 3	2180	^{14}C test	
2002 Jun 9-20	2184-2187	silica gel column	batch mode
2002 Jun 21-date	2189-date	data taking	

Table 5.1: Dates and run numbers of the purification phases: Column Loop and Batch Test (CLT and CBT), Water Extraction (WE) and Blank Loop (BL).

Moreover, after each loop, the purification was stopped for a while in order to better mix purified and not-purified scintillator in the CTF inner vessel. This "stop and go" strategy increases the probability to purify all the scintillator mass.

- *Silica gel column.* Purification with the silica gel column was tested twice. In "Column Loop Test" (CLT) scintillator was continuously extracted from the IV, purified and re-poured in the IV. However, the loop mode, as in the first water extraction test, doesn't guarantee processing the entire scintillator mass. The problem was solved in the "Column Batch Test" (CBT), where all the scintillator mass was stored in the EPN module and, purified and then re-poured in the CTF vessel.

- *Blank loop* (BL). Scintillator circulated in the Module 0 and IV filter in order to check the cleanliness of such devices.

Table 5.1 reports dates and run numbers of all the operations and purification tests performed during the CTF-3 campaign.

The last 2 years of data taking were characterized by the impossibility to manipulate the scintillator. This was due to an incident that occurred on 16th of August 2002 which required the laboratory to stop all the operations involving liquids and to start a careful review of its hydraulic systems. We have exploited this very long period of data taking without any scintillator manipulation to better understand the CTF background, techniques of analysis and investigate strategies to be adopted in Borexino.

As will be described in the next chapter, several analyses require the inclusion of multiple data runs to increase statistics. Each run corresponds to a data taking interval of 1-3 days.

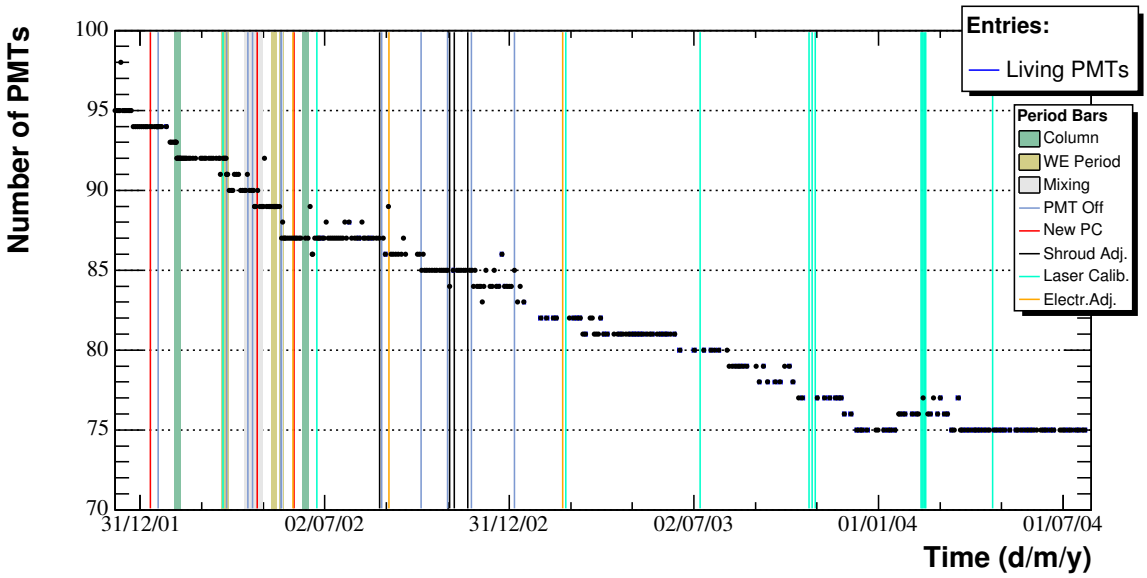

Figure 5.1: Number of the living PMT's in function of time. In the plot, the purification tests and the main operations are codified with different coloured vertical lines and boxes.

"Summing" runs together is allowed within homogeneous phases. Each phase is thus defined as corresponding to a stable detector configuration, usually related to a period between two sequential purification tests.

The stability of the detector depends mostly on the electronics stability. For example, at the end of several runs, some PMT's showed some unstable behaviour, like distorted spectra signals due to an excess of absorbed current. In order to avoid any systematic effects, we excluded their information from the reconstruction code and thus from the data analysis. Figure 5.1 shows the number of "living" PMT's as function of time. In 3 years, we lost about 20% of the PMT's. In order to maintain the homogeneity of the results, all the energy spectra or energy cuts are normalized to 100 PMT's.

5.2 Energy and position reconstruction

The reconstruction code has been developed in order to determine the energy and position of each scintillation event produced inside the scintillator, exploiting the charge and time information at the phototubes.

The energy of an event is derived from the number of photons collected by each PMT and hence from the corresponding total charge, defined as the integrated charge from the initial trigger up to 500 ns. The trigger occurs when 6 PMT's give signal within 30 ns (corresponding to a low energy threshold of 25 keV).

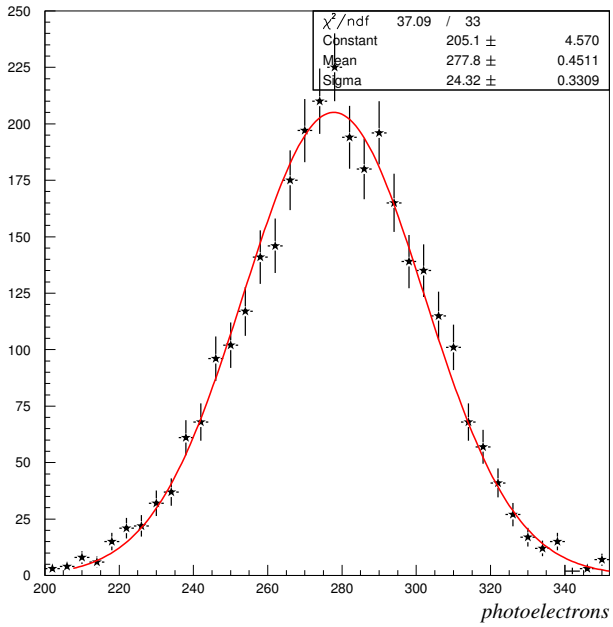

Figure 5.2: Fit the energy spectrum of ^{214}Po applying a radial cut of 0.6 m during radon infiltration after the first ^{14}C test.

The fit of the ^{214}Po energy spectrum (Figure 5.2) on the "group 2" chain (see Section 4.2) with a Gaussian provides a precise indication about the energy response of the detector. The energy resolution at the ^{214}Po energy is 9% . The peak, after the conversion to energy using the light yield S derived from the ^{14}C analysis (see next section), is found centered on 703 $\pm$ 2 keV corresponding to a quenching factor equal to 10.94 $\pm$ 0.03.

A good position fitter code is fundamental in order to perform fiducial volume cuts and thus external background reductions. The existing fitter is essentially a vertex reconstruction, based on the shape of the time signal distribution of the detected photons.

The event spatial reconstruction is based on the time information of each single photons. The arrival time t_a^i of the first photon of the ith electronic channel is equal to [89]:

$$t_a^i = t_0 + t_d^i + t_f^i + t_j^i \tag{5.1}$$

where t_0 is the absolute time of the event, t_d^i the scintillator decay time, t_f^i the time of flight, and t_j^i is the jitter time proper of the PMT. In the assumption that the propagation is linear, the time of flight, t_f^i is equal to:

$$t_f^i = \frac{r^i \times n}{c} \tag{5.2}$$

where r^i is the distance between the photon production point and the PMT photon, c is the speed of light and n is the index of refraction. However, deviations from the linearity of the photon propagation can take place because of effects like elastic scattering or absorption and re-emission, and total reflection in proximity to the vessel. In order to correct such deviations, an "effective index of refraction", n_{eff}, has been introduced.

Once r^i is calculated, it is possible to evaluate $t_d^i + t_j^i$:

$$t_d^i + t_j^i = t_a^i - t_0 - \frac{r^i \times n_{eff}}{c}. \tag{5.3}$$

The MINUIT code [90] maximizes the likelihood function defined by:

$$L(t_{ev}, \overrightarrow{r}_{ev}) = \prod_i f(t_d^i + t_j^i). \tag{5.4}$$

The probability density function $f(t_d^i + t_j^i)$ is defined as the Laplace convolution of the probability density functions for t_d^i and t_j^i. It describes the probability that a photon detected at time t_i by the *i-th* phototube has originated in the space-time coordinates $(t_{ev}; \overrightarrow{r}_{ev})$.

During the CTF-1 campaign, the detector was calibrated with a radon source positioned in the center of the vessel. This was useful to tune parameters of the reconstruction such as the effective index of refraction n_{eff}, and to test the performance of the reconstruction code itself: the difference between the nominal and the reconstructed position was found 0 with an error of 5 cm. The resolution decreases when the event occurs further from the geometric center and for increasing energies.

5.3 ^{14}C contamination of the scintillator

^{14}C is a long-lived radioactive isotope of carbon ($\tau_{1/2}$~5730 years). It is produced by cosmic rays in the atmosphere through the reaction ^{14}N(n,p)^{14}C. In living material, the ^{12}C/^{14}C ratio is about 10^{-12}. Oils and petroleum, from which pseudocumene is synthesized, are extracted from deep underground which offers a natural shielding against cosmic rays. The ratio thus decreases by 5-6 orders of magnitude. However, the ^{14}C is present in the pseudocumene molecule and it can not be removed with any purification technique.

^{14}C β-decays with a Q-value of $\sim$ 156 keV. In Borexino, as already mentioned, a ^{14}C contamination is admissible if the ratio ^{14}C/^{12}C ratio is of the order of magnitude of 10^{-18} or less.

The ^{14}C amount was measured with CTF in different samples taken during the scintillator delivery campaign. Table 5.2 shows the amount of PC introduced in the vessel and the correspondent mass of scintillator removed.

The ^{14}C activity $A_{^{14}C}$ is measured by fitting the energy spectrum with a theoretical function. The theoretical ^{14}C beta spectrum [94] is defined by:

Date	Sample	Run	Scintillator removed (kg)	PC added (kg)	PPO conc. (g/l)
11/1/02	2	2075	360	440	1.34
26/4/02	3	2153	359	405	1.19
3/6/02	4	2180	320	438	1.03

Table 5.2: During the ^{14}C tests scintillator is removed while PC is added. The initial scintillator mass (sample 1) in the inner vessel is equal to 3749 kg and the PPO concentration is 1.50 g/l.

$$\frac{dN}{dE}(T,Z) = A\left(2m_eT + T^2\right)^{1/2} \cdot (T + m_e) \cdot (T_0 - T)^2 \cdot C(T) \cdot F(T,Z) \tag{5.5}$$

where T is the kinetic energy, m_e the electron mass, T_0 the Q-values and A is a normalization factor.

F(T,Z) is the non-relativistic Fermi function that takes into account the Coulomb interaction between the β and the nucleus:

$$F\left(T', Z\right) = \frac{2\pi T'}{1 - e^{-2\pi T'}} \tag{5.6}$$

with

$$T' = \frac{Z\alpha \cdot (T + m_e)}{\sqrt{T^2 + 2m_eT}} \tag{5.7}$$

α, Z the fine structure constant and the effective atomic number, respectively.

C(T) is the "spectral shape factor" which contains departures from the allowed shape due to the presence of induced weak currents. The energy dependence adopted here, refers to the paper [97] by Wietfeldt et al. and is defined by:

$$C(T) = 1 - \alpha \cdot (T + m_e) \tag{5.8}$$

The largest uncertainty in the theoretical ^{14}C spectrum is correlated to a precise knowledge of the α parameter. From literature, we found several values arising from different theoretical models (α = 0.37 [94], 0.38 [96], 0.45 [97], 0.6 [98]). The fit itself of the energy spectrum suggests (with large errors) an α value compatible with the result of [97] (α = 0.38).

In order to take into account the non ideality of the detector, the energy resolution has to be included in the model by a convolution. Moreover the theoretical spectrum must be converted from energy to the correspondent number of photoelectrons (n) using the scale conversion (light yield S), which is a free parameter in the fit.

The spectrum function is thus defined by the convolution:

$$C(n) = \int_{-\infty}^{+\infty} \frac{dN}{dE}(E)\, g(n,E)\, dE \tag{5.9}$$

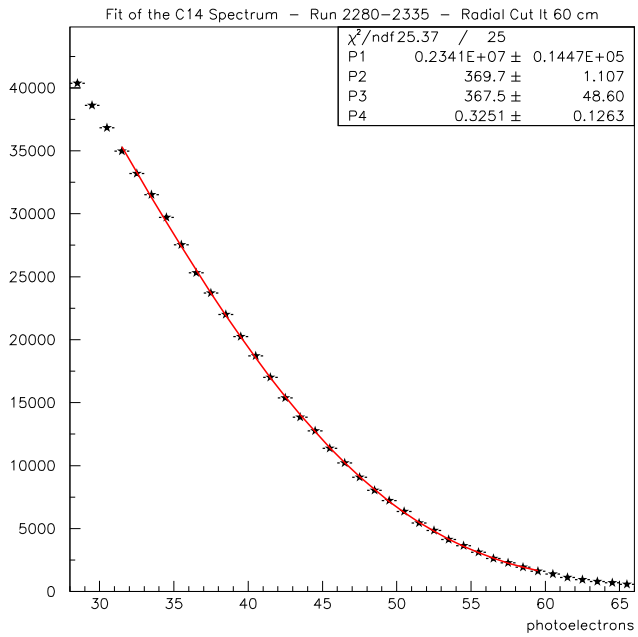

Figure 5.3: Fit of the ^{14}C energy spectrum.

where the energy resolution is:

$$g\left(n,E\right)=\frac{e^{-\frac{\left(E-\frac{n}{S}\right)^{2}}{2\sigma^{2}}}}{\sqrt{2\pi}\sigma} \tag{5.10}$$

and

$$\sigma=\sqrt{\frac{c\cdot E}{S}}. \tag{5.11}$$

The correction factor c takes into account the relative variance, among all the PMT's, of the single PMT gain (c $\sim$ 1.34 [95]). The normalization of the function is evaluated numerically.

The fit function (5.9) takes into account only the ^{14}C contamination. Other contaminants, like ^{210}Pb, contribute only a few percent to the low energy spectrum (50 - 100 keV).

A second systematics arises from the quenching effect which induces a non-linear distortion of the theoretical shape. Such an effect implies an estimated average loss of the light yield of only a few photoelectrons per MeV. Moreover the shape distortion is partially absorbed in the fit by letting the light yield S be a free parameter (Figure 5.3). Such systematics does not significantly affect the ^{14}C activity evaluation.

Let $N_{^{14}C}$ and $\tau_{^{14}C}$ be the total number of ^{14}C atoms in the CTF3 scintillator and its lifetime respectively. The ^{14}C/^{12}C mass ratio R is given by [99]:

Sample	$^{14}C/^{12}C$ (10^{-18})
1	1.60± 0.01
2	1.89± 0.07
3	4.90± 0.08
4	5.11± 0.08

Table 5.3: Measured ^{14}C concentration in each delivered batch.

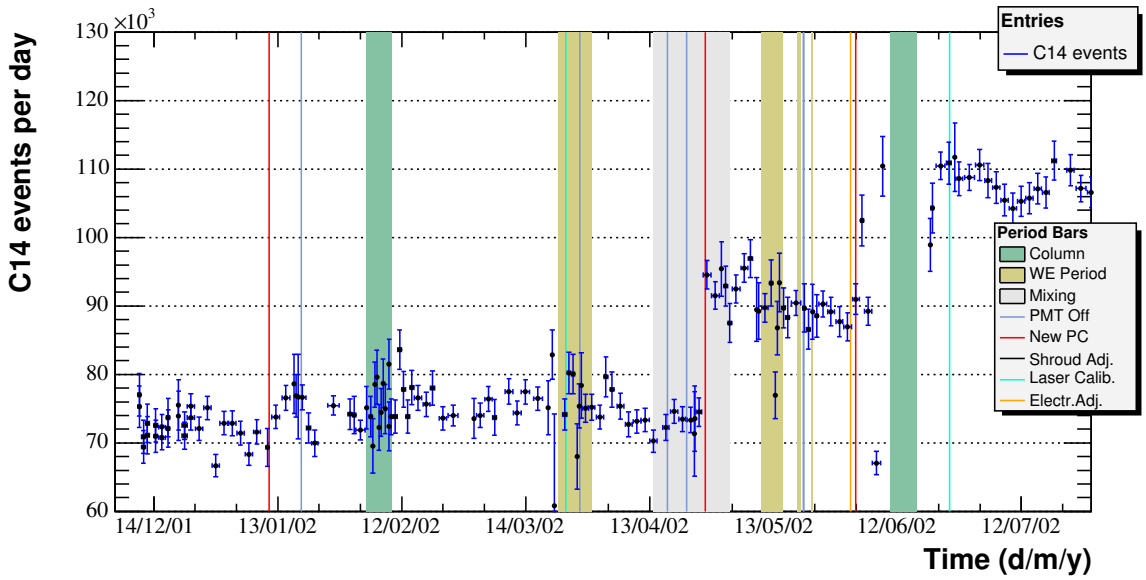

Figure 5.4: ^{14}C activity from energy fit. The spectrum is fitted day per day applying a 0.6 m radial cut in the range 50 - 100 photoelectrons. The red vertical lines identify the ^{14}C tests. The results are normalized to the whole detector mass and to the total energy spectrum.

$$R\left(\frac{^{14}C}{^{12}C}\right) = \frac{N_{^{14}C}}{N_{^{12}C}} = \frac{40}{3}\left(\frac{\tau_{^{14}C}}{m_{IV}N_A}\right)A_{^{14}C} \tag{5.12}$$

where N_A is Avogadro's number and m_{IV} is the mass of PC in the CTF-3 inner vessel.

The measurements and results for the various pseudocumene batches are summarized in Table 5.3, and the ^{14}C content are reported for each run in Figure 5.4.

The first two batches have a ^{14}C activity consistent with the one measured in CTF-1 (1.94 ± 0.09 x 10^{-18} [88]) while the last two show a contamination larger by a factor $\sim$ 2.5. The achieved results are still within the Borexino specification.

5.4 Energy calibration from the ^{14}C spectrum

For safety reasons, during the CTF-3 campaign, there has not been the possibility to calibrate the detector by deploying known sources. The energy calibration was thus performed by exploiting the most abundant contaminants present in the scintillator. Among them, ^{14}C fulfills the main requirements: it has a high activity, it is easy to be tagged and the other contaminants in the same energy region are negligible. On the other hand, the detector trigger imposes a low energy cut because of the rate being too high, so that the lower region of the energy spectrum is lost. Moreover, as already mentioned, a large uncertainty on energy scale arises from the quenching of β particle, which is small compared to the α particles, but is not negligible.

Therefore, the Birks model parametrizes the quenching effect by the empirical function [52, 100]:

$$Q\left(E\right) = \int_0^E \frac{dt}{1 + kB\frac{dE}{dt}\left(t\right)} \tag{5.13}$$

where dE/dX is the Bethe-Bloch equation for β particles [101] :

$$-\frac{dE}{dt} = 2\pi N_a r_e^2 m_e c^2 \rho \frac{Z}{A}\frac{1}{\beta^2}\left[ln\frac{\tau^2\left(\tau+2\right)}{2(I/m_e c^2)^2} + G\left(\tau\right) - \delta - 2\frac{C_s}{Z}\right] \tag{5.14}$$

with

$$G\left(\tau\right) = 1 - \beta^2 + \frac{\frac{\tau^2}{8} - \left(2r_e + 1\right) ln2}{\left(t+1\right)^2}, \tag{5.15}$$

τ is the kinetic energy in units of $m_e c^2$, C_s and δ the shell and the density correction, respectively.

The quenching function *Q(E)* (5.13) does not act on the theoretical spectrum but only on the energy response of the detector. The convolution (5.9) thus becomes:

$$C\left(n\right) = \int_{-\infty}^{+\infty} \frac{dN}{dE}\left(E\right) g\left(n, Q(E), S\right) dE \tag{5.16}$$

with

$$g\left(n, Q(E), S\right) = \frac{e^{-\frac{\left(Q(E)-\frac{n}{S}\right)^2}{2\sigma^2}}}{\sqrt{2\pi}\sigma} \tag{5.17}$$

where n is the number of photoelectrons, S the light yield and σ is defined in Eq 5.11.

The distorting effect is shown in Figure 5.5.

The fit of the energy spectrum has secondary minima if both S and kB are assumed as free parameters. It is thus impossible to evaluate simultaneously from the fit the light yield

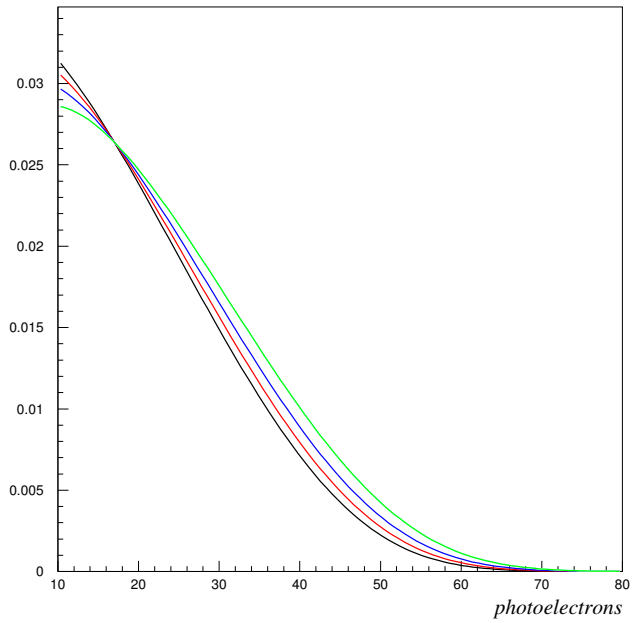

Figure 5.5: Theoretical ^{14}C energy spectrum distorted by the quenching effect for kB = 0.005 (blue), 0.010 (red), 0.015 (black) cm/MeV compares to no distortion (green).

and the quenching effect. The Birks parameter has been fixed to a reasonable value (kB = 0.01 cm/MeV). The systematics on S is estimated at 4.4% assuming a range for kB from 0 to 0.015 cm/MeV which is the maximum measured value for scintillators with characteristics similar to pseudocumene [52].

The time variation of the light yield measured from the ^{14}C energy spectrum is shown in Figure 5.6. In the following analyses, each spectrum and cut in photoelectrons is scaled by S achieved from the ^{14}C spectrum fit. The observed changes in light yield are mostly attributed to electronics instability and/or to possible small variations of the optical properties of the scintillator.

5.5 Radon contamination

^{222}Rn can contaminate the detector in different ways:

- directly from ^{238}U present in the scintillator;
- from air leaks in the pipes and in containers used during the scintillator purification or in the vessel filling;
- emanated from ^{226}Ra present in the vessel or in the walls of pipes and containers;

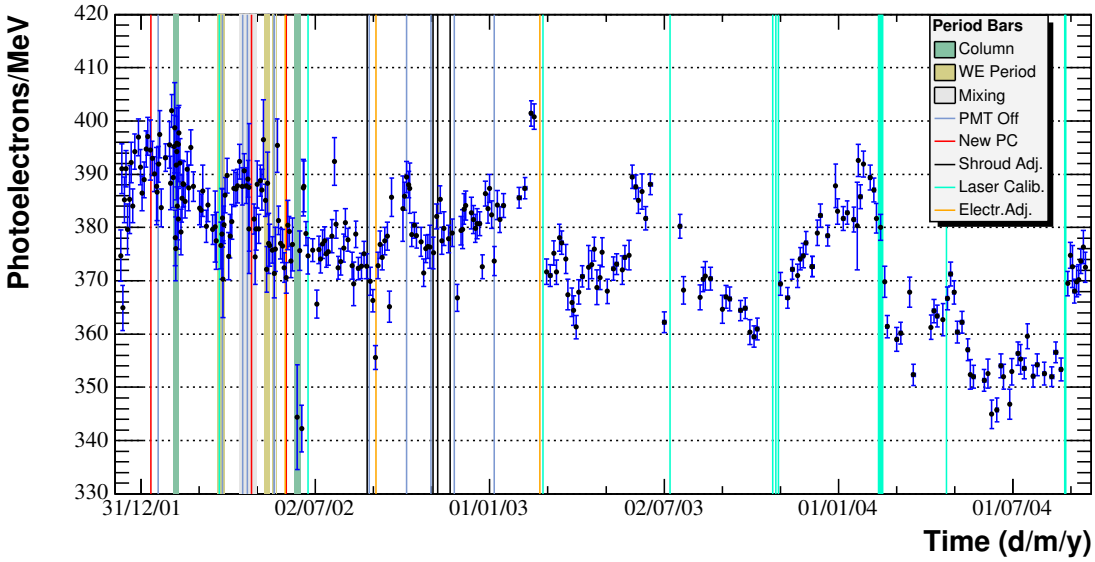

Figure 5.6: Time profile of the light yield S resulting from the run per run fit of the ^{14}C energy spectrum. The error bars represent the statistical error.

- from radon in the water buffer permeating the nylon membrane.

Radon itself has a relatively short mean life (5.5 days), and in small amount does not represent a real problem in CTF. More dangerous are its daughters, most of all ^{210}Pb which has a lifetime of 32 years. ^{210}Pb β-decays with energy below the threshold (Q-value $\sim$ 15 keV), while its daughters ^{210}Bi and ^{210}Po decay with energies in the neutrino window, once quenched.

^{222}Rn is tagged through the delayed coincidences, exploiting the fast β-α sequence of the ^{214}Bi-^{214}Po segment, which occurs in 232 μs.

The radon origin can be deduced by looking at the decay time of the tagged ^{214}Po, since all isotopes in the ^{238}U chain between ^{222}Rn and ^{214}Bi have a mean life of less than half an hour. If the time profile of such coincidence events follows the ^{222}Rn mean life, their origin can be attributed to radon out of secular equilibrium. Otherwise, if the ^{214}Bi-^{214}Po coincidence rate is constant in time, radon can be attributed to the presence of ^{226}Ra (2340 years mean life) or to possible radon leaks, like permeation through the nylon membrane. In case of no radon leaks and assuming secular equilibrium it could be due to the ^{238}U contamination.

Even though radon is a danger for the experiment, it also represents a powerful tool for monitoring the detector. The time profile of the tagged ^{214}Po, shown in Figure 5.7, emphasizes each radon infiltration, which occurs practically in any fluid operations. A large activity has been measured for the initial scintillator loading of the detector and for each following ^{14}C test. This is due to scintillator which collects radon passing through pipes and tanks.

Data Set	Phase	Count Rate (ev/d/m_{IV})	^{238}U (10^{-16} g/g)	^{226}Ra (10^{-22} g/g)
A: 2054 -2073	initial batch	6.0±1.0	14.9± 2.3	5.5±0.9
B: 2104-2122	after SG loop test	2.8±0.7	7.0± 1.6	2.6±1.4
C: 2130-2149	after first WE	2.0±0.1	5.0± 0.2	1.8±0.1
D: 2153-2173	after blank loop	unable to fit	unable to fit	unable to fit
E: 2153-2173	after SG batch test	2.0±0.2	5.0± 0.5	1.8±0.2
F: 2320-2450	after 1 year since SG in batch	1.1±0.1	2.8± 0.2	1.0±0.1

Table 5.4: Equivalent ^{238}U and ^{226}Ra derived from the ^{214}Bi-^{214}Po count rate. Period D is too short for a correct identification of a constant rate. No radial cut has been applied.

A leak was registered after the first ^{14}C test when the count rate increased up to thousands events per day. It turned out that the leak was due to a valve open towards the outside along one of the pseudocumene lines.

5.6 Uranium contamination

^{226}Ra (and ^{238}U if secular equilibrium is assumed) can be deduced from the ^{214}Bi-^{214}Po coincidence. The radon decay profile shown in Figure 5.7 is fitted in different periods with the ^{222}Rn decay function plus a constant B:

$$R = \frac{A}{\tau} e^{-t/\tau} + B \tag{5.18}$$

where τ is fixed to the ^{222}Rn mean life (5.52 days).

The efficiency of detecting the ^{214}Bi-^{214}Po delayed coincidence depends on the applied energy and time cuts:

- 1) cut in the number of photoelectrons for the second event: $200 < n < 400$ ($\varepsilon = 0.996$);
- 2) cut on the coincidence time: $2\ \mu s < t < 710\ \mu s$ ($\varepsilon = 0.944$).

The total detection efficiency is 94.0%.

Goal of the fit is measuring the rate of the constant term, which can be identified with ^{226}Ra (or ^{238}U) or to a constant permeation from the vessel or from the water buffer. I analyzed six periods (Figure 5.8):

- *Period A* - Initial batch of scintillator (run 2054-2073).
- *Period B* - After the test of the silica gel in loop mode (run 2104-2122).
- *Period C* - After the first water extraction test (run 2130-2149).

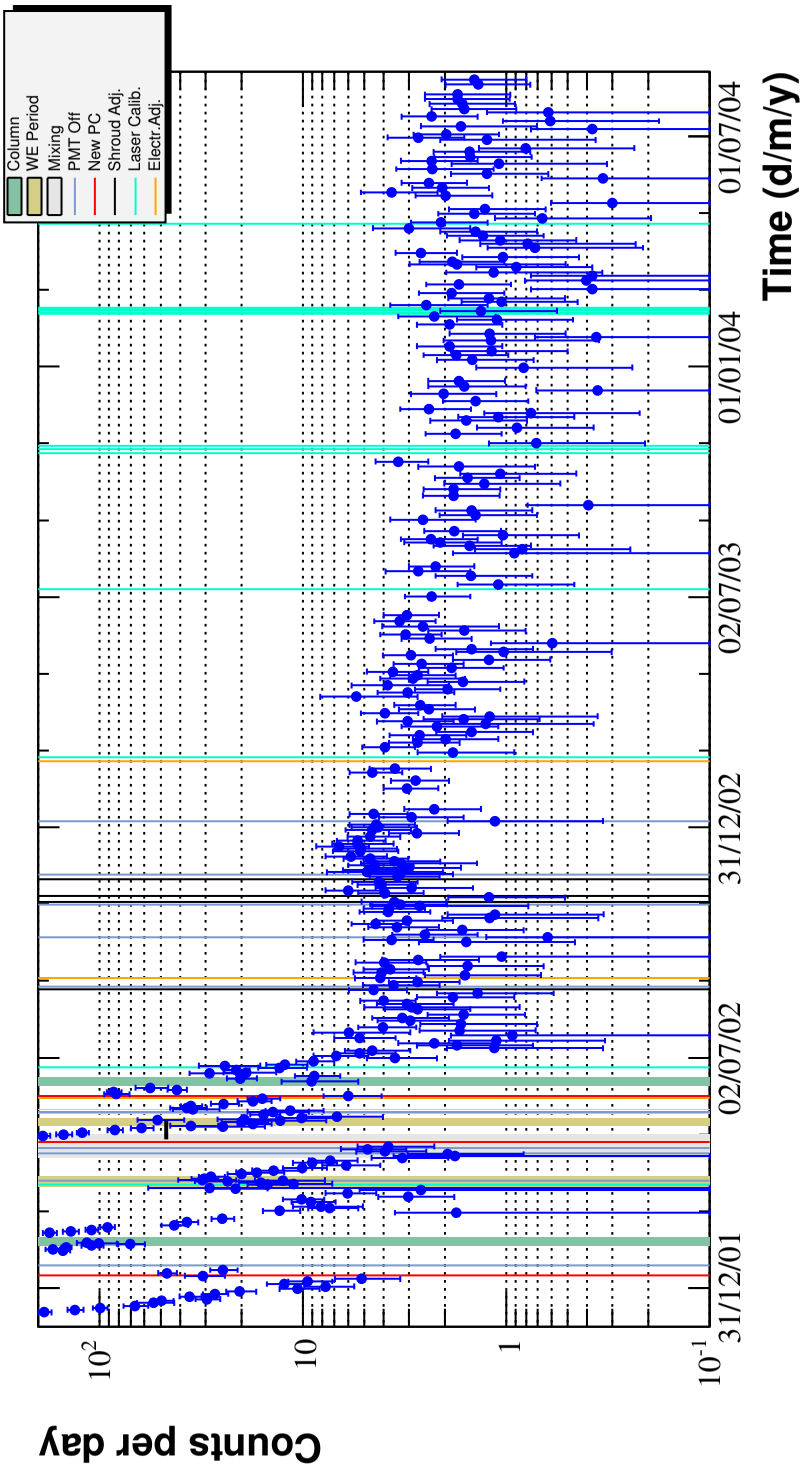

Figure 5.7: Time profile of the radon contamination in CTF.

- *Period D* - After the blank loop and during the second water extraction test (run 2153-2173).
- *Period E* - After the test of the silica gel in batch mode (run 2190 - 2220).
- *Period F*- After 1 year since the last manipulation of the scintillator (run 2320-2450).

Period D is too short for allowing a correct identification of the constant rate. All the results are reported in Table 5.4.

The silica gel column in loop mode reduced the constant rate by a factor ~ 2 while the water extraction purification seems, as expected, absolutely inefficient in ^{226}Ra (or ^{238}U) removal. Until now, the equivalent ^{238}U concentration is (2.8±0.2)x10^{-16}g/g.

Radon permeation from the water buffer is verified by comparing *Period E* and *Period F* when, at the beginning of November 2003, we realized that the "shroud" (the outer vessel) lost its spherical shape. Soon after the shroud adjustment (indicated as black lines in the bottom figure of 5.8), we noticed a radon infiltration, however the plateau decreased by a factor ~ 2 , after all the radon decayed. It is important to underline that the shroud is partially open for buoyancy reasons. A shape distortion can dilate the "holes" and therefore decrease the barrier efficiency against radon. At the present time, the shroud still has a non spherical shape.

5.7 Krypton contamination

As already described in Chapter 3, ^{85}Kr β-decays into ^{85}Rb with a 99.56% branching ratio and a Q-value of 687 keV. The half life is 10.76 years. 0.43% of the times it decays to a metastable level:

$$^{85}K \rightarrow {}^{85m}Rb \rightarrow {}^{85}Rb \tag{5.19}$$

emitting in sequence a β-particle (Q-value 173 keV) and a γ of 514 keV. The de-excitation of ^{85m}Rb occurs with a mean life of 146 μs. It is possible to measure the total activity of ^{85}Kr in CTF, by tagging the fast β-γ coincidence. Each identified coincidence corresponds to 231.5 β-events emitted via the dominant β-channel.

The efficiency of detecting the β-γ coincidence depends on the applied energy and time cuts:

- 1) energy cut on the β event: E $<$ 241 keV ($\varepsilon = 0.61$);
- 2) energy cut on the γ event: 300 keV $<$ E $<$ 600 keV ($\varepsilon = 0.83$);
- 3) cut on the coincidence time: 100 ns $<$ t $<$ 6 μs ($\varepsilon = 0.93$).

The total detection efficiency is 47%.

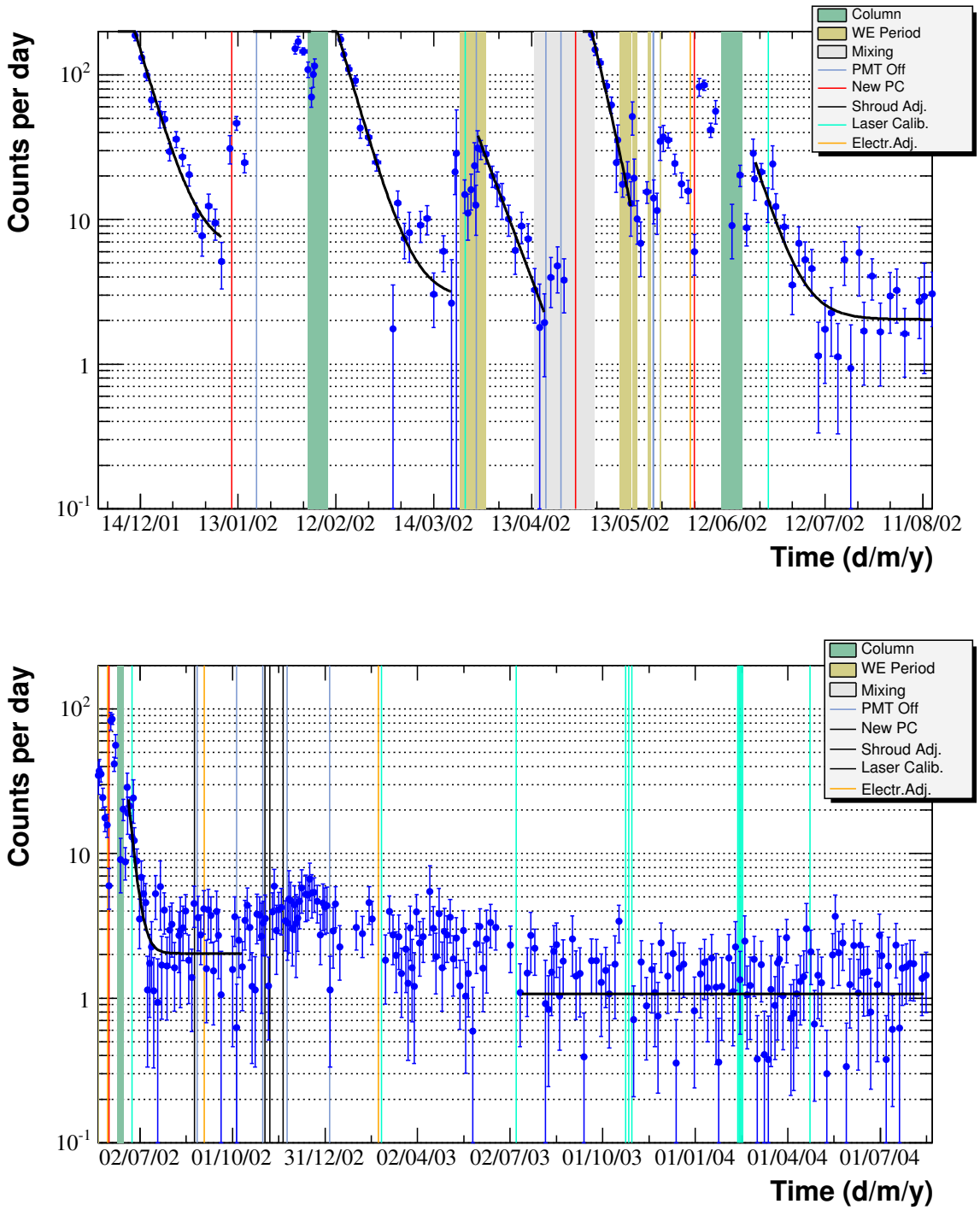

Figure 5.8: Fit of the radon profile with Eq. 5.18. The constant activity can be attributed to ^{226}Ra (^{238}U if secular equilibrium is assumed), to a permeation through the nylon membrane from radon in the water buffer or to emanation from ^{226}Ra on the vessel.

The first energy cut is limited by the trigger efficiency of the detector. The amount of light released at low energy, indeed, may be not sufficient for producing a trigger which needs six simultaneous hits.

The efficiency of the cut on γ energy peak is affected by the quenching effect. The peak is in fact shifted to lower energy by the quenching of the Compton electrons produced by the ionization shower following the γ interaction. The peak position from the fit of the energy spectrum is thus measured to be 471 $\pm$ 2 keV (Figure 5.9) .

The time cut is necessary in order to avoid bias due to the electronics in recording short time coincidences. A loss of efficiency has been observed for coincidence up to 75 ns [99].

Approximately 2.5% of the ^{214}Bi-^{214}Po coincidence (false event) occurs within the time gate used for selecting krypton. Nevertheless, energy cuts strongly reduce the possibility to misinterpret false event since the total probability to overlap ^{214}Bi-^{214}Po and ^{85}Kr-^{85m}Rb events is estimated to be 10^{-5}. This may represent a problem only if radon activity has a very significant rate.

The correctness of the selection technique is confirmed by fitting the coincidence time profile as shown in Figure 5.9. The measured coincidence time, in fact, is equal to 1.3 $\pm$ 0.2 μs in good agreement with the expected 1.46 μs.

The results are summarized in Table 5.5 and in Figure 5.10. The factor for scaling the rate to the neutrino energy window is 0.34.

The initial concentration was about $\sim$ 400 counts/day over the entire energy spectrum. The nitrogen stripping (see Chapter 3) before and during the first water extraction has reduced the total count rate by a factor $\sim$ 4-5. Moreover, analyzing a fiducial volume of 0.8 m radius (Table 5.5), the rate decreased by a factor $\sim$ 8-10. The selected coincidence events have, indeed, a spatial distribution more concentrate in proximity of the vessel, suggesting a contamination on the nylon membrane.

The combination of the CTF-3 results and the last results concerning low argon krypton nitrogen, described in Chapter 3, are very promising for the Borexino experiment. The efficiency of krypton removal with nitrogen stripping depends strongly on the krypton contamination in nitrogen. The ^{85}Kr contamination in the Borexino nitrogen will be $\sim$ 1000 times lower than the actual contamination (see Tables 3.7 and 3.8). In Borexino we expect to reduce krypton contamination down to 1 count/day, or less, over the entire fiducial mass.

5.8 Radial Analysis

One of the main issue of the data analysis is to discriminate the contamination present in the scintillator from the activity on the nylon vessel surface or from external sources. In Borexino such a problem will be minimized thanks to the low ratio ($\sim$ 0.7) between the surface of the vessel and the volume of the scintillator. In CTF on the other hand, the ratio is $\sim$ 4

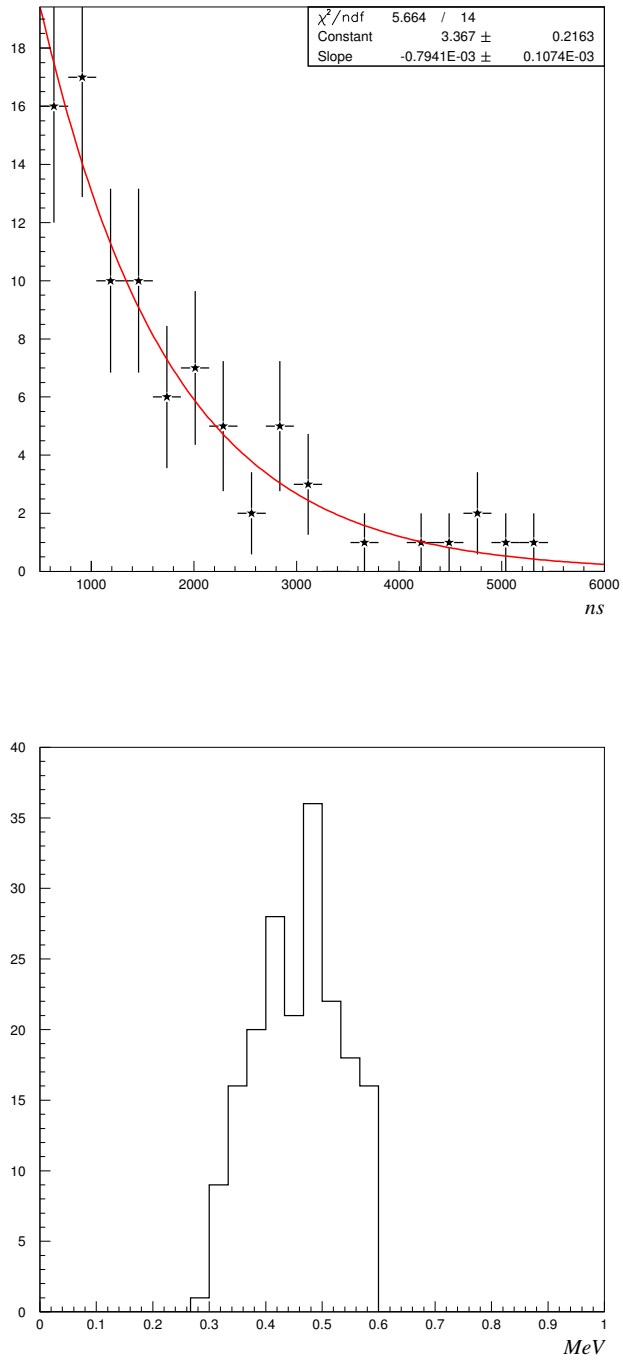

Figure 5.9: Coincidence time and energy distribution for selected krypton events. The fast decay $^{85}Kr \rightarrow {}^{85m}Rb \rightarrow {}^{85}Rb$ occurs with a mean life of 1.46 μs which is in agreement with the result of the fit (red line): 1.3 ± 0.2 μs.
The plot on the bottom shows the energy spectrum of the γ emitted by ^{85m}Rb at 514 keV. The peak is shifted to 471 ± 11 keV because of the quenching of the Compton electrons produced by the ionization shower following the γ interaction.

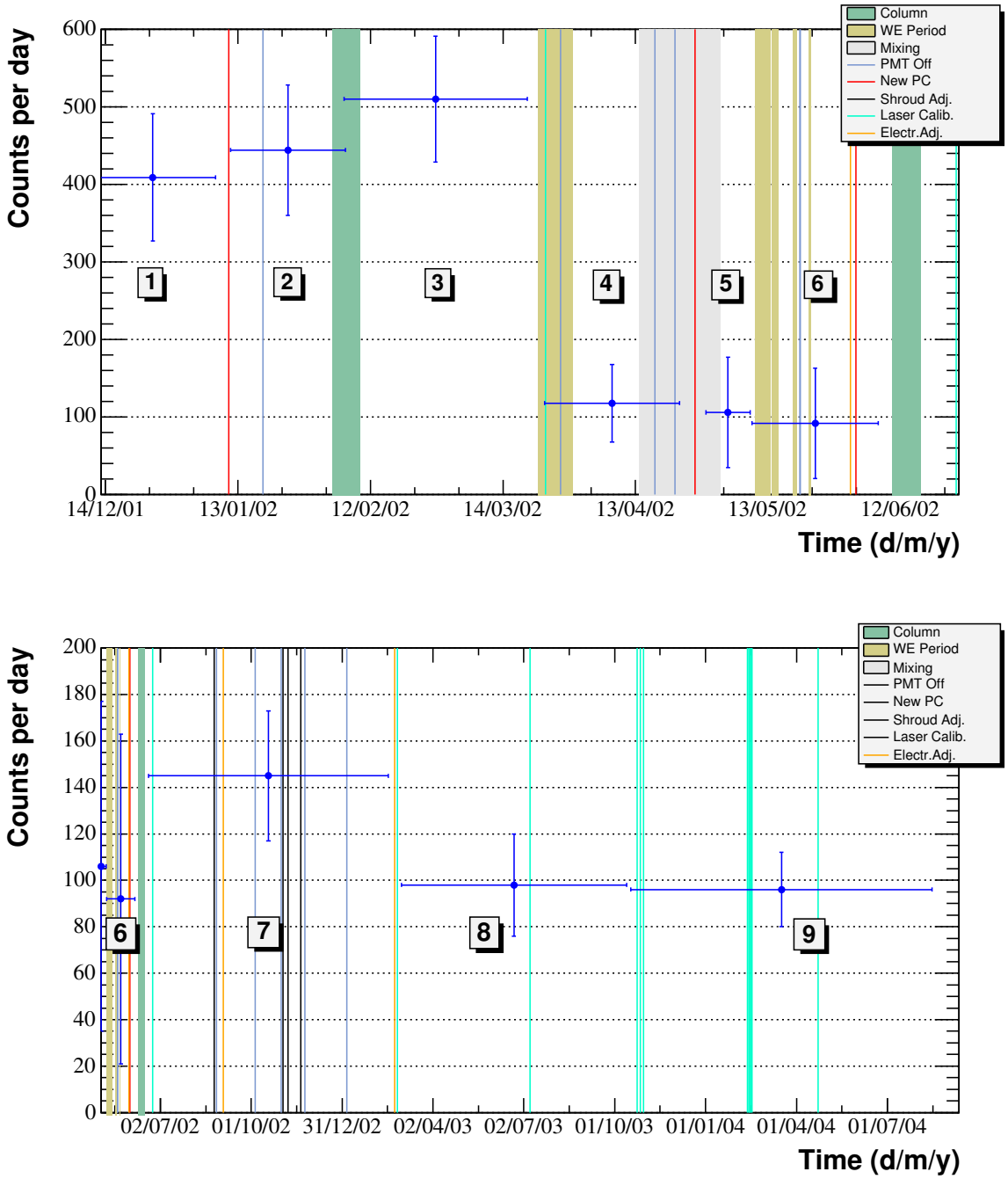

Figure 5.10: Krypton rate during and after the purification tests. The rate is scaled from the ^{85}Kr-^{85m}Rb coincidence selected in all the volume and in the entire energy range (Table 5.5). In the neutrino window fall ~34% of the events.

Data Set	Days	^{85}Kr-^{85m}Rb events (r < 2 m)	^{85}Kr activity (c/d/m$_{IV}$)	^{85}Kr-^{85m}Rb events (r < 0.8m)	^{85}Kr activity (c/d/m$_{IV}$)
1: 2056-2073	24.1	20±4	409±82	10±3	358±108
2: 2074-2093	21.1	19±4	443±84	7±3	287±123
3: 2094-2122	33.0	38±6	510±81	19±4	498±105
4: 2125-2149	26.3	7±3	118±50	0	< 91 (90%)
5: 2154-2161	12.5	3±2	106±71	0	< 191 (90%)
6: 2162-2183	24.1	5±2	92±71	0	< 99 (90%)
7: 2188-2281	94.6	31±6	145±28	2±1	18±9
8: 2282-2345	99.1	22±5	98±22	7±3	61±26
9: 2346-2434	165.8	36±6	96±16	9±3	47±16

Table 5.5: ^{85}Kr-^{85m}Rb coincidence events in all the volume and applying a radial cut of 0.8 m in 9 different periods. Each analyzed period is identifiable with the correspondent purification test looking at Figure 5.10. The krypton activity is deduced scaling the selected coincidence events for the metastable branching ratio (0.43%) and for the efficiency of detection (47%). The reported krypton rate is referred to the all energy spectrum: in the neutrino window fall only ~34% of the events.

times higher, and the nylon membrane itself is thicker by a factor > 2 than in Borexino. The contamination from the surface, as already demonstrated in CTF-1, is dominant respect to the internal activity. The external activity, which was a crucial problem in CTF-1, has been partially solved introducing the outer vessel barrier.

5.8.1 Theoretical aspects of the bulk and surface distributions

In order to define a radial distribution function, few assumptions are needed:

- the CTF vessel is spherical and centered on the origin of coordinates;
- the detector resolution σ is constant throughout the volume of the vessel;
- the reconstruction error is isotropic, which means $\sigma_x = \sigma_y = \sigma_z = \sigma$ at all points in the detector;
- the external contamination is negligible.

The resolution $R(\overline{x}_d, \overline{x}_r)$ is expected to be a Gaussian in $\overline{x}_d$, the observed position of the event, and centered at $\overline{x}_r$,the real position [103]:

$$R(\overline{x}_d, \overline{x}_r) = \frac{e^{-\frac{(\overline{x}_d - \overline{x}_r)^2}{2\sigma^2}}}{(2\pi\sigma^2)^{3/2}}. \tag{5.20}$$

Let be $\phi_r(\overline{x})$ the real spatial distribution, then, the probability that the reconstructed event will be observed within the volume element $d^3\overline{x}$ is given by:

$$\phi_d(\overline{x})d^3\overline{x} = \int_{\overline{x}'\epsilon\, IV} \phi_r(\overline{x})d^3\overline{x} \cdot R(\overline{x},\overline{x}') \cdot d^3\overline{x'}. \tag{5.21}$$

Inserting Eq 5.20, Eq 5.21, becomes:

$$\phi_d(\overline{x}) = \int_{\overline{x}'\epsilon\, IV} \phi_r(\overline{x}) \cdot \frac{e^{-\frac{(\overline{x}-\overline{x'})^2}{2\sigma^2}}}{(2\pi\sigma^2)^{3/2}} \cdot d^3\overline{x'}. \tag{5.22}$$

Defining $r = |\overline{x}|$, the argument of the exponential in Eq 5.22 can be expanded:

$$\left(\overline{x} - \overline{x'}\right)^2 = r^2 + r'^2 - 2r \cdot r' \cdot cos\theta \tag{5.23}$$

where θ is the angle between the vectors $\overline{x}$ and $\overline{x'}$.

Converting to spherical coordinates and recalling the assumption of a constant σ, the probability density function (Eq 5.22) becomes:

$$\phi_d(r) = \frac{1}{\sqrt{2\pi}\sigma r} \int_{-R}^{R} \phi_r(r') \cdot r' \cdot e^{-\frac{(r-r')^2}{2\sigma^2}} dr'. \tag{5.24}$$

Since the contamination in the vessel is assumed to be uniform, the true bulk distribution is constant and equal to 1/V, where V is the scintillator volume. The observed volumetric distribution is thus defined by:

$$V_d(r) = \frac{r^2}{V} \int_{\Omega} d\Omega \phi_d(r) = \frac{3}{R^3} \frac{r}{\sqrt{2\pi}\sigma} \int_{-R}^{R} r' \cdot e^{-\frac{(r-r')^2}{2\sigma^2}} dr' \tag{5.25}$$

where R is vessel radius.

The real surface distribution is defined as:

$$\phi_r(r) = \frac{\delta(|r| - R)}{4\pi R^2}. \tag{5.26}$$

Substituting Eq 5.26 in Eq 5.24, the observed surface distribution becomes:

$$S_d(r) = \frac{r}{R^2} \frac{1}{\sqrt{2\pi}\sigma} \left(e^{-\frac{(r-R)^2}{2\sigma^2}} - e^{-\frac{(r+R)^2}{2\sigma^2}} \right). \tag{5.27}$$

$V_d(r)$ and $S_d(r)$ are plotted in Figure 5.11 assuming a constant σ equal to 15 cm for both the distributions. A more detailed study about the radial distribution can be found in [103].

5.8.2 Results from the radial fit

A direct test of the radial distribution is given by the fit of the ^{214}Po spatial distribution. ^{214}Po emitted α's, selected via ^{214}Bi-^{214}Po coincidence, are mainly internal events so that the fit function requires only the bulk parametrization (Eq 5.25). The fitted radial spectrum is relative to the period of runs 2074-2090 when a significant contamination of radon guarantees

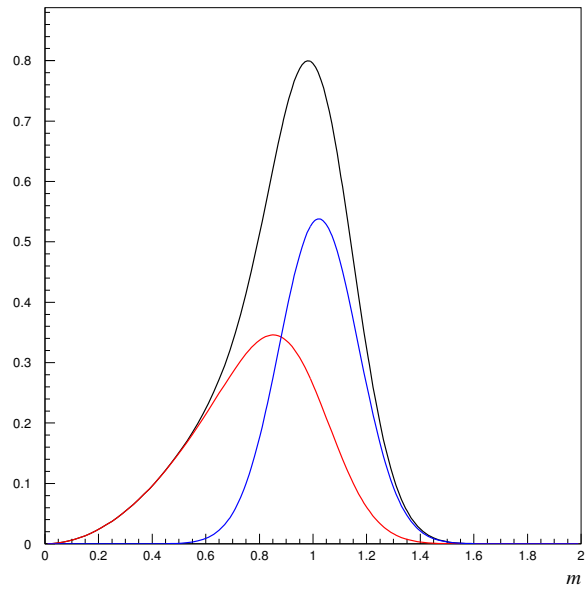

Figure 5.11: Theoretical radial distribution (black line), sum of the bulk (red) and the surface (blues) distributions, derived from Eq 5.25 and Eq 5.27, respectively. σ is assumed to be constant to 15 cm for both the distributions.

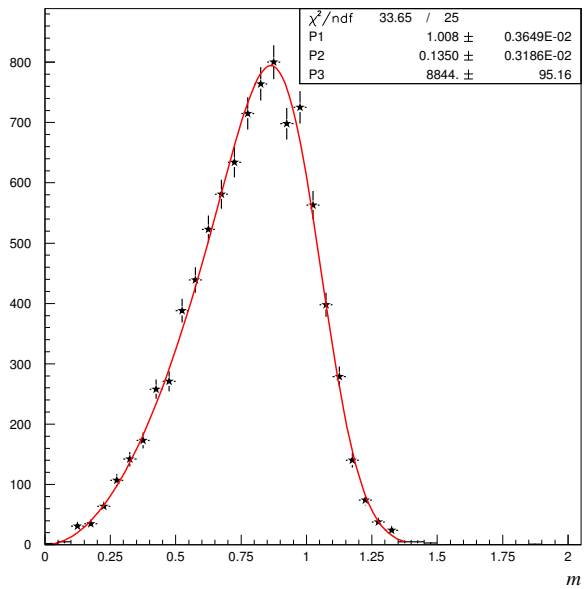

Figure 5.12: Fit of the ^{214}Po radial distribution with the bulk distribution (Eq 5.25). The resolution of the detector is equal to 13.5 $\pm$ 0.3 cm at the energy of the ^{214}Po α particle ($\sim$750 keV, after the).

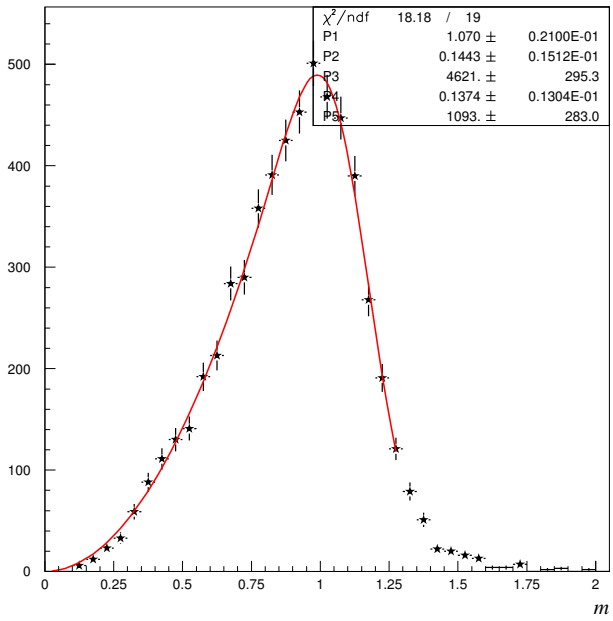

Figure 5.13: Radial fit of run 2074, assuming bulk and surface distributions.

very high statistics ($\sim$ 9000 events in 18 days). The fitted spectrum is shown in Figure 5.12. Fitted σ, equal to 13.5 $\pm$ 0.3 cm is in good agreement with the previous CTF-1 results, where σ was found to be $\sim$ 12.5 cm. The bulk distribution also provides precise information about the vessel radius, which from the fit equals to 100.8 $\pm$ 0.4 cm in the period after the first ^{14}C test.

Amplitudes and resolutions of the bulk and surface functions are free parameters in the radial fit. Both resolutions have to be considered averaged since there is no formalization which parametrizes spatial resolution as a function of the deposited energy. The only parameter in common between the two distributions is the vessel radius.

An example of a radial fit is shown in Figure 5.13, relative to run 2074. The fitted radius is equal to 107 $\pm$ 2 cm which is 2.6 σ from the 100.8$\pm$ 0.4 cm found in the ^{214}Po sample. This is due to the external background, neglected in our formalization, which shifts the spectrum.

The results of each run of the radial fit are plotted in Figure 5.14, for internal (blue points) and surface (red points) events, after subtraction from the bulk contamination of the radon segment deduced by the ^{214}Bi-^{214}Po coincidence.

The time profile of the surface rate shows a smooth decrease by a factor 0.7 in the whole data taking period. This could be due to ^{210}Po installed in the membrane which decays with τ = 199.6 days.

Comparing the purification phases, with coloured boxes and lines in Figure 5.14, we notice

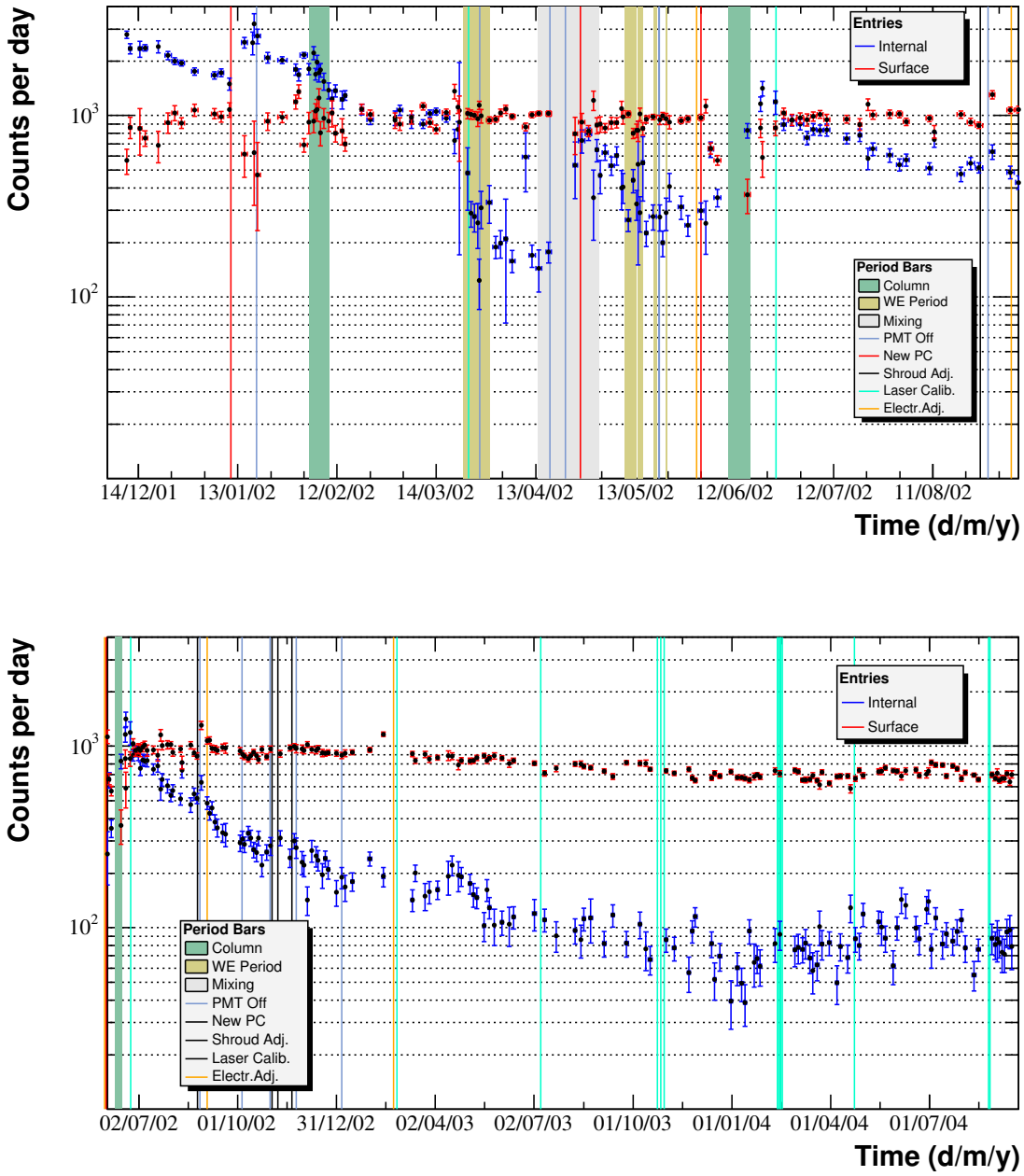

Figure 5.14: Time profile of the internal (blue points) and of the surface (red) events from the radial fit. In the top figure the purification phases are represented with coloured boxes and lines. In the bottom figure, relative to the second period of data taking in which there has been no manipulation of the scintillator, part of the internal events decays with the mean life of ^{210}Po.

Data Test (run)	Phase	Internal Events (c/d/m$_{IV}$)	External Events (c/d/m$_{IV}$)
2056-2074	1st batch of scintillator	1953±34	930±30
2974-2093	After 1st ^{14}C test	2074±43	819±35
2094-2122	During and after SG in loop	1102±19	941±17
2125-2149	During and after 1st WE	193±11	989±15
2154-2161	During blank loop	478±20	914±21
2162-2183	During and after 2nd WE	280±13	940±14
2188-2281	During and after SG in batch	566±25	967±10
2282-2301	8 months after SG in batch	257±23	972±12
2302-2345	10 months after SG in batch	178±12	917±15
2346-2382	16 months after SG in batch	121±15	822±12
2383-2434	20 months after SG in batch	87±9	757±10

Table 5.6: Average internal and surface activity during different phases of the data taking.

that the highest purification efficiency has been reached by the water extraction tests. The first test, in fact, reduced the total contamination by a factor ~ 5 while the second by a factor ~ 3. The use of nitric acid in water in the second test did not increase the efficiency contrary to expectations.

The silica gel test was efficient only in the loop mode reducing the total internal contamination by a factor ~ 2. After the batch mode, the radial fit recorded a spike-like increase of the bulk events. Analyzing the time profile of internal events after a transient of few months (Figure 5.14 bottom), the introduced contaminant seems to be compatible with the mean life of ^{210}Po, probably collected in the EPN module. Such theory is supported by the energy analysis, described in detail in the next section.

In Figure 5.14 (bottom), a smooth increasing of the internal events was recorded around April 2003. The comparison with Figure 5.8 relative to the radon time profile, suggest that the increasing is due to the radon contamination. The radon segment subtraction seems thus to be inefficient at the level of 10-15%.

Up to date, the internal count rate is about 80 events/day. The energy analysis can clarify the weight of each single contamination which contributes to the internal count rate.

5.9 Energy analysis

The energy distribution has been parametrized analytically for each contaminant.

The distribution, C_{obs}, has been formalized convolving the theoretical spectrum $C_{theo}(E)$ with the energy resolution of the detector $R(E)$:

$$C_{obs}(E) = \int_{-\infty}^{+\infty} C_{theo}(E - E')R(E')dE' \tag{5.28}$$

where

$$R(E) = \frac{e^{-\frac{(E-E_0)^2}{2\sigma(E_0)^2}}}{\sqrt{2\pi}\sigma(E_0)} \tag{5.29}$$

and, defining n as the number of photoelectrons correspondent to the energy deposition E_0,

$$\frac{\sigma(E_0)}{E_0} = \frac{\sqrt{n}}{n} \tag{5.30}$$

Introducing the light yield S, Eq 5.30 becomes:

$$\sigma(E_0) = \frac{E_0}{\sqrt{n}} = \frac{E_0}{\sqrt{S \cdot E_0}} = \sqrt{\frac{E_0}{S}}. \tag{5.31}$$

The internal background consists of α and α+γ events, that produce a discrete spectrum, and β or β+γ events, that produce a continuous spectrum.

The model function for α decays is a Dirac function. The convolution produces a simple Gaussian coincident with Eq 5.29, centered on the sum of the β-equivalent quenched energy of the specific α particle and the eventual contributions from the γ-rays.

For the β decays, we use the theoretical shape of the β-spectrum, including the corrections for Coulomb screening due to the high Z. The function, as for the β case, is shifted by the eventual contributions from the γ-rays. A complete description of the energy distribution formalization can be found in [104, 105].

The weights of each expected decay or of each segment of natural radioactive chain (when equilibrium is assumed) are free parameters in the fit. An example of the analytical function with arbitrary weights is plotted in Figure 5.15.

The analytical formalization, contrary to the Monte Carlo one, is a flexible approach that allows the method to better adapt itself to unexpected and not easily reproducible effects, first of all, the quenching effect. The quenching energy distortion is non linear and strongly differs for α and β particles. At least two known α sources are needed in order to calibrate the energy scale. The detector is calibrated on the ^{222}Rn,^{218}Po and ^{214}Po peaks with the experimental function:

$$q(E) = \frac{E}{A - B \cdot E} \tag{5.32}$$

where A and B are free parameters of the fit.

The energy analysis, however, is strongly limited by the necessity of high statistics. The optical distorting effects in proximity to the vessel, like total reflection, imposes a stringent software cut of the fiducial volume down to 0.6 m radius, which strongly reduces the statistics. Therefore the analyzed data must be collected for very long periods, averaging the measured rates even during the purification phases. As consequence, the approach looses the sensitivity

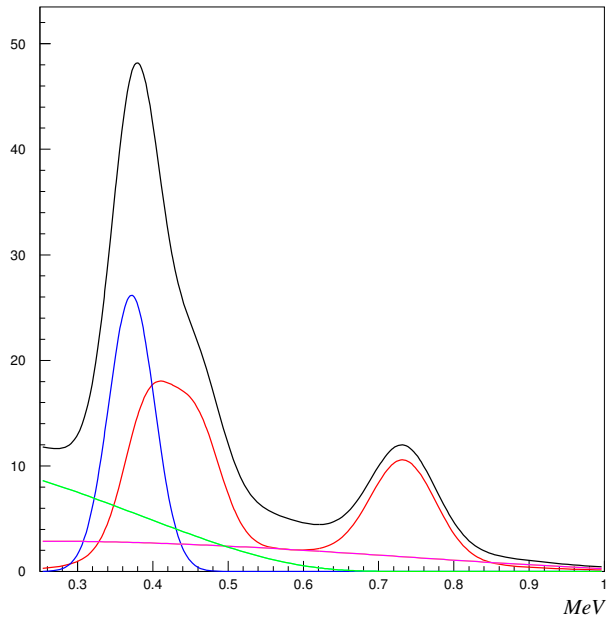

Figure 5.15: Analytical energy spectrum (black line). Superimposition of the single components: radon segment in equilibrium (^{222}Rn+^{218}Po+^{214}Bi+^{214}Pb+^{214}Po red line), ^{210}Po (blue) , ^{210}Bi (violet) and ^{85}Kr (green).

to observe the decay time of the contaminants. The analyzed spectra are shown in Figure 5.16.

A second limitation arises by the need for well identifiable feature of the spectral shapes. This means that the analytical function has the sensitivity to distinguish, and thus to fit, only the main spectral components. A typical case is provided by ^{85}Kr and ^{39}Ar, which are both pure β-decay with close Q-values, 632 keV and 565 keV, respectively. The smearing effect due to the energy resolution and the spectral overlapping by other contaminants make the fit unable to discriminate ^{85}Kr from ^{39}Ar. ^{85}Kr and ^{39}Ar are treated in the fit approach with only one β-spectrum with an averaged Q-value.

Despite such limitations, the analytical method in the energy analysis is a powerful tool. It can be considered as an alternative approach to the Monte Carlo or, where it is necessary, it can include specific Monte Carlo parametrization.

The analyzed energy range is [0.25 -1] MeV. The contaminant activities included in the fit are: ^{210}Po (see next subsection), ^{210}Bi, the radon segment in equilibrium (^{222}Rn + ^{218}Po + ^{214}Pb + ^{214}Po + ^{214}Bi) and ^{85}Kr (and/or ^{39}Ar). The results of the fits are summarized in Table 5.8. All the contribution are normalized to the entire energy spectrum. The factors for scaling the results to the neutrino energy window, [0.25 - 0.8] MeV, are listed in Table 5.7.

In the data set of runs 2346-2434, which corresponds to 162 days of effective data taking (last plot in Figure 5.16), the function was unable to fit properly the spectrum. In such period, the trace contaminants show a relative low activity while external background becomes more consistent (evident in the [0.7 - 1.0] MeV energy range). For a proper formalization of the external background, a Monte Carlo simulation would be required.

In period of relative low activity, when the ^{85}Kr (and/or ^{39}Ar) spectrum is completely dominated by other contaminants, the fit identify a ^{85}Kr component compatible with 0. In such cases, the ^{85}Kr activity has been neglected.

The resulting χ^2's from the fits are always in the range of [1.0 - 1.5] (93 degrees of freedom), confirming the correctness of the model. The main systematics source is due to the normalization on the fiducial mass and it has been evaluated at the level of 16% corresponding to 5 cm uncertainty on the vessel radius.

5.9.1 A ^{210}Po-compatible contamination

The energy plots in Figure 5.16, relative to different periods of the the data taking (refer to Table 5.6 for the phase identification), highlight the presence of a very high activity at low energy. The fit of the time profile of the internal events from the radial analysis suggests the presence of a long life element ($\tau >$ 130 days). The $\alpha - \beta$ analysis recognizes such contamination as an α-decay and the quenching function of Eq 5.32, calibrated on the radon segment consistent with an α-energy range of $\sim$ [5.0 - 5.5] MeV.

From the literature, the isotope which is most compatible with these features is ^{210}Po. The ^{210}Po mean life is 197 days and it decays emitting a 5.3 MeV α. Such contamination comes from the ^{210}Pb segment belonging to the ^{238}U chain. ^{210}Pb β-decays in ^{210}Bi with a mean life of 32.3 y and a Q-value $\sim$ 15 keV, not detectable by CTF. On the other hand, ^{210}Bi can be detected since it β-decays in ^{210}Po, in $\sim$ 7 days with a Q-value $\sim$ 1.2 MeV. ^{210}Po decays in ^{206}Pb which is a stable isotope.

We identified two possible causes which can justify the presence of ^{210}Po:

- *From ^{210}Pb.* ^{210}Pb builds up after exposure to radon or it can be collected by the scintillator passing through pipes or tanks. Such hypothesis can be supported by looking if the equilibrium between ^{210}Bi and ^{210}Po is established.

- *Direct ^{210}Po contamination.* ^{210}Po could be directly present in the scintillator and/or on the vessel. In such cases, we don't expect any equilibrium between ^{210}Bi and ^{210}Po, but we should observe a constant decay with the ^{210}Po mean life.

The results shown in Table 5.8 underline a non-equilibrium between ^{210}Bi and ^{210}Po in all the analyzed phases apart before the silica gel batch test and in the last period (run: 2282-2345). In particular, in the first scintillator batch we found a strong non-equilibrium from which we

Isotope/Segment	Relative weight in the NW
^{210}Po	1
^{210}Bi	0.61
Radon segment	3.87
^{85}Kr	0.35
^{39}Ar	0.28

Table 5.7: Isotope weights relative to the neutrino energy window [0.25 - 0.8] MeV. respect to the whole energy spectrum. The radon segment corresponds to ^{222}Rn,^{218}Po,^{214}Pb,^{214}Po and ^{214}Bi in equilibrium.

Data Set	**Activity in the whole energy spectrum**				**Activity in the NW**	
(run set)	^{210}Po	^{210}Bi	*Rn segment*	$^{85}Kr/^{39}Ar$	*Total*	*Total (no Rn)*
	(c/d/m$_{IV}$)	(c/d/m$_{IV}$)	(c/d/m$_{IV}$	(c/d/m$_{IV}$)	(c/d/m$_{IV}$)	(c/d/m$_{IV}$)
2056-2073	1592±23	287±23	38±5	352±42	2034±36	1883±30
2074-2093	1516±31	459±14	875±51	unable to fit	5269±205	1795±32
2094-2122	734±22	404±30	80±6	517±49	1469±41	1151±33
2125-2149	119±10	50±7	8±3	90±21	211±18	180±13
2154-2161	376±23	321±40	145±10	unable to fit	1148±52	572±33
2162-2183	216±9	167±15	21±3	unable to fit	401±18	318±13
2188-2281	282±5	102±4	5±1	77±12	389±8	370±7
2282-2345	40±3	34±7	∼0	125±11	102±6	102±6

Table 5.8: Single component rates from the energy fit. In the last two columns, the total rates are scaled to the neutrino window, [0.25 - 0.8]MeV using the coefficients in Table 5.7.

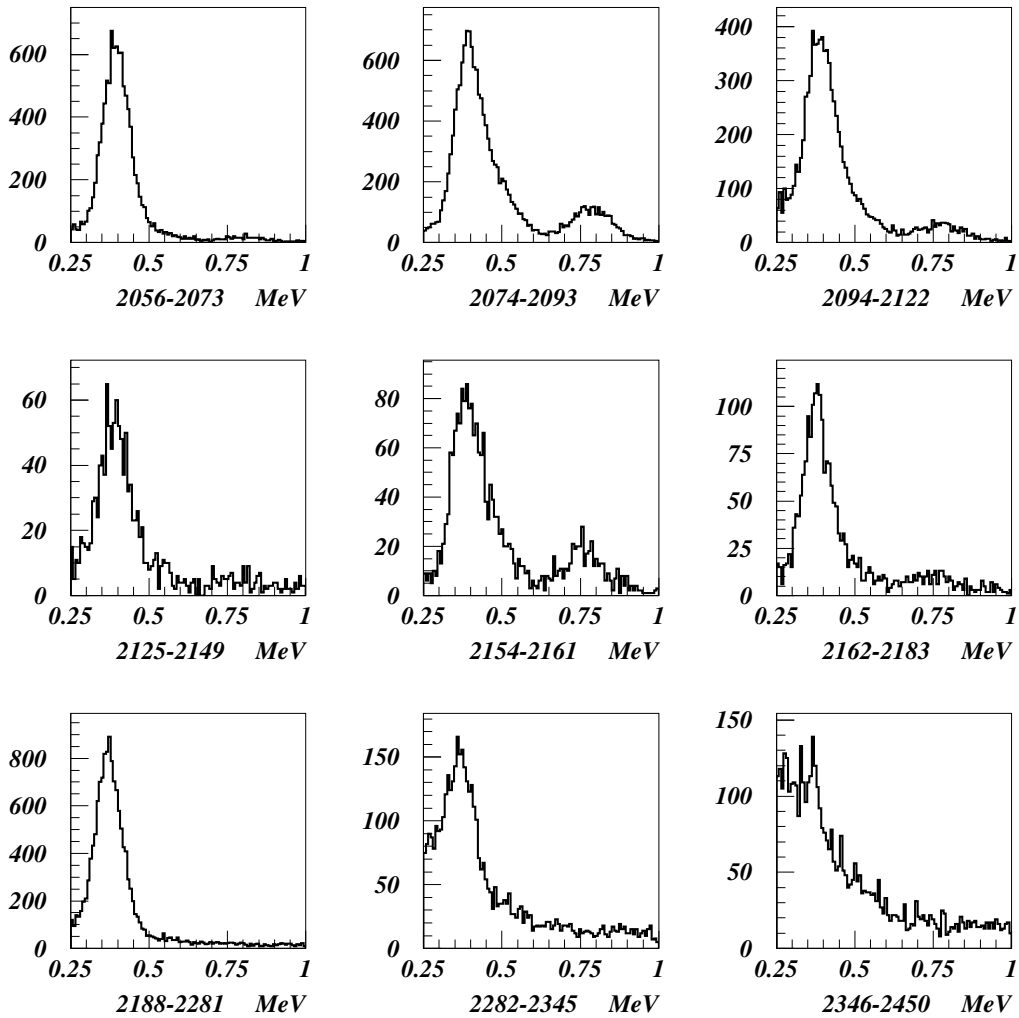

Figure 5.16: Energy spectra in 9 periods of the data taking in 0.6 m radius fiducial volume.

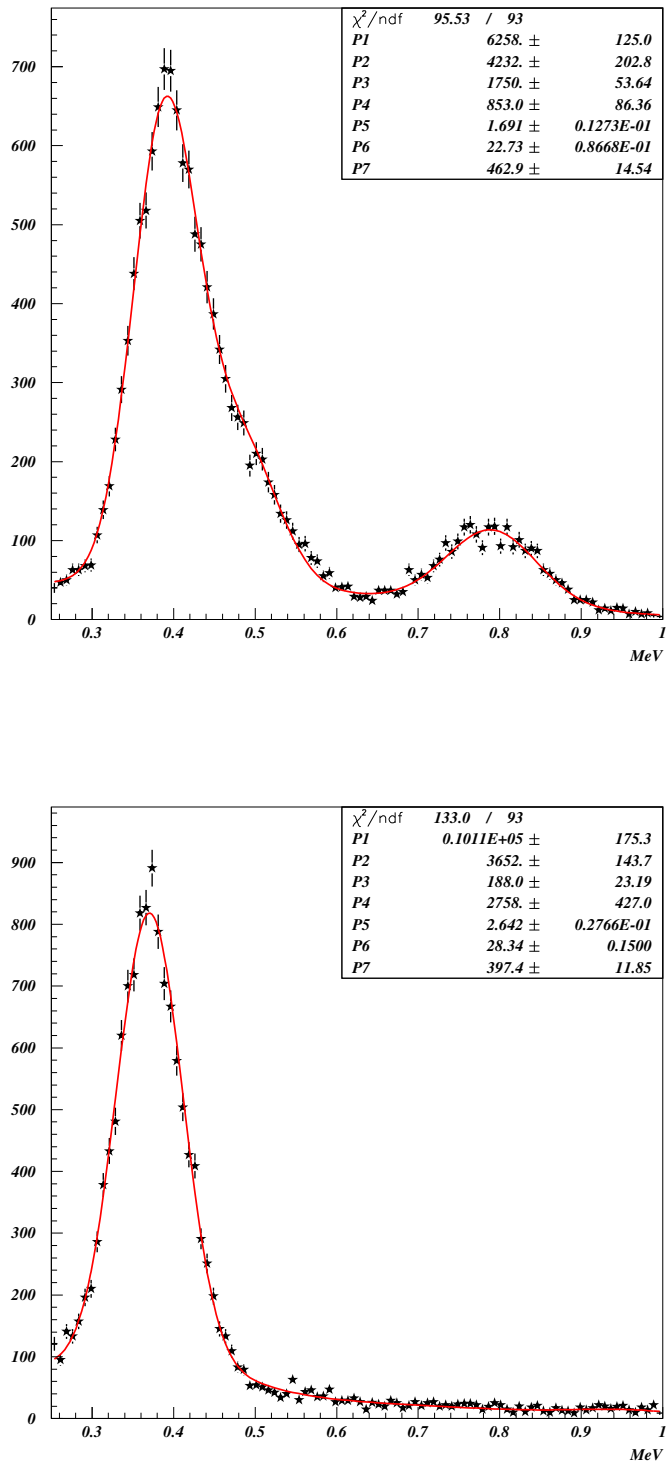

Figure 5.17: Fits of the energy spectra of period runs 2073-2094 (top) and 2188-2281 (bottom). The free parameters of the fits are the amplitudes related to ^{210}Po, ^{210}Bi, radon segment and ^{85}Kr.

can infer that the scintillator is directly contaminated by ^{210}Po rather than by its parent, ^{210}Pb.

After the blank loop we observed a possible increase of the ^{210}Pb activity. It can be related to a ^{210}Pb contamination of the walls of the pipes where the scintillator was circulated or on the nylon membrane that was "washed" during the operation. ^{210}Pb contamination is justified by the ^{210}Bi rate which increased as well up to the ^{210}Po activity, suggesting an equilibrium.

The origin of the ^{210}Po contamination after the silica gel batch test is still under study but we believe that tank which contained the scintillator for the purification was contaminated. The silica gel loop test, indeed, was efficient only by a factor ~ 2, and we expected an increased purification factor processing the whole mass in batch. In order to clarify what really happened, the collaboration intends to test a second time the column in batch mode.

Since we have not yet identified a proper strategy in order to reduce its activity, ^{210}Pb (and so ^{210}Po) is one of the most crucial contaminants in CTF. On the other hand, we have still to probe the distillation which we consider to be the most efficient purification test for such contamination.

5.9.2 Global results

The rates reported in the last column of Table 5.8, after the radon segment subtraction, can be directly compared to the internal results from the radial analysis in Table 5.6. The total activity is always consistent with the internal rate apart after the column batch test where we have already underlined an inefficiency in the radon subtraction.

The energy analysis confirms the stripping efficiency in ^{85}Kr and ^{39}Ar removal by a factor 5.74±0.04. ^{39}Ar activity is estimated by subtracting the ^{85}Kr internal activity, derived from the delayed coincidence (Table 5.5), from the ^{85}Kr/^{39}Ar rate. In the first batch we identified an activity < 348 counts/day (95% C.L.). In the data set after the column in batch (run 2188-2281) the contamination activity was equal to 59 ± 16 counts/day in the whole energy spectrum. It remained constant during the following 8 months (run 2282-2345) when we measured an activity less than 99 counts/day (95% C.L.).

As already turned out in the previous subsection, the column test in loop mode has reduced the ^{210}Po activity by a factor ~ 2. Nevertheless, it does not affect the ^{210}Bi contamination.

The water extraction tests, on the other hand, have demonstrated a similar efficiency in both the ^{210}Po and ^{210}Bi purifications. The reduction factors for the two isotopes, indeed, are in the first test ~ 6 and ~ 8, respectively and in the second test ~ 2 for both the isotopes. The strategy of introducing nitric acid in water, during the latter test, has turned out to be ineffective.

In next CTF activity, the Borexino collaboration has planned to repeat the column batch test and to try for the first time in this campaign the purification by distillation.

5.10 Conclusion

The goals of the analysis of the CTF-3 data campaign are twofold: to identify each contamination source and to study the purification efficiencies.

Analyses of the delayed coincidences have successfully quantified single isotope activity, even when it was less than 1 event per day (e. g. ^{226}Ra). The statistical analyses (energy and radial) have confirmed the coincidence results and allowed the identification of the ^{210}Po contamination, whose high activity was unexpected.

The measurement of the rates has given us the possibility to estimate the efficiencies in purifying single isotopes. When, on the other hand, the purification results were ambiguous, the analysis has addressed the collaboration to operate toward the correct solution.

Nevertheless, all the analyses I have reported in this Chapter can be strongly improved calibrating the detector with known sources in energy and spatial resolution. Furthermore, a calibration would allow a complete study of the all systematics of the detector. The Borexino collaboration will address this issue as soon as the operation on the CTF will restart.

Finally, all the analysis techniques presented and tested here will be adopted for the Borexino detector.

Chapter 6

The Borexino Potential in *pep* and CNO Neutrinos

With the recent progress in the field of neutrino physics, the astrophysics questions addressed by solar neutrino spectroscopy have moved into the focus of the current research. In particular direct measurements of the primary neutrino flux from pp (*pep*), ^{7}Be and CNO are of fundamental relevance.

Borexino's primary goal is to measure the solar ^{7}Be flux. However, beyond this objective, Borexino has the potential to probe solar neutrinos from the *pep* fusion process, from the CNO cycle as well as the low energy part of the ^{8}B branch.

The interaction rates for *pep* and CNO neutrinos in organic scintillator predicted by the latest BP2004 version of the standard solar model by Bahcall and Pinsonneault [8] in the currently preferred MSW LMA solution for the solar neutrino problem [47] are respectively 2.1 and 6.6 events per day in 100 metric tons of liquid scintillator. We should underline here that if the data recently released by the LUNA collaboration on the ^{14}N + p fusion cross section [9] are taken into consideration [8], the expected CNO rate significantly decreases down to 3.5 events per day in 100 tons.

The *pep* neutrino energy spectrum is distinctive, with a single 1.44 MeV monochromatic line. When detected via $\nu - e$ scattering, the resulting energy spectrum of the scattered electron presents a characteristic Compton-like edge at 1.22 MeV. We will focus our attention on the energy window for the recoil electron between 0.8 and 1.3 MeV: for sake of simplicity, all event rates cited from here on will be referred to this energy window, unless otherwise noted. The expected signal rate S in this window for *pep* and CNO neutrinos combined is 2.0 events per day in 100 tons, or equivalently 2.0×10^{-2} ton^{-1}d^{-1} (1.5×10^{-2} ton^{-1}d^{-1} when using the most recent report from LUNA for the ^{14}N + p cross section [8, 9]).

A first prerequisite for a successful measurement of the *pep* and CNO neutrinos in Borexino is a very low background from the long-lived radioactive chains. A ^{238}U and ^{232}Th contamination at the 10^{-17} g/g level, coupled with a ^{nat}K contamination of 10^{-15} g/g would translate

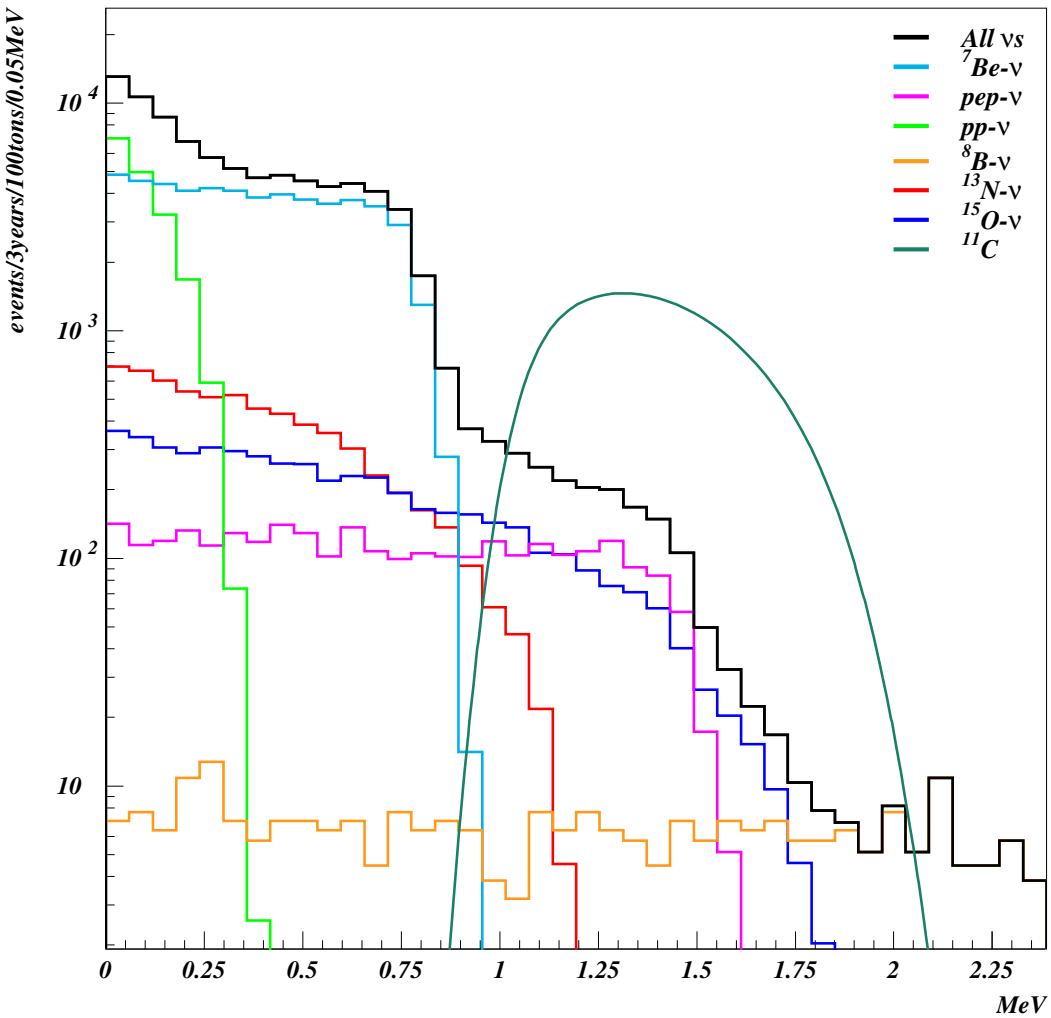

Figure 6.1: ν energy spectrum expected in Borexino (BP2004+LUNA+LMA, see Chapter 1) overlapped by the ^{11}C β^+-spectrum (dark green) assuming 3 years of data taking in 100 ton fiducial mass.

into 0.6 background events per day in 100 tons in the observation window [73], just below the event rate expected for *pep* neutrinos. Also, contamination from long-lived radon daughters out of secular equilibrium with ^{238}U (in particular from ^{210}Bi) must be reduced below one count per day in the window of interest.

A second prerequisite is a low external gamma-ray background from the construction materials of the detector and from the surrounding rocks. The general strategy to solve the problem is the use of pure buffer materials to screen environmental radioactivity present in underground laboratories and of extremely low radioactivity construction materials. The external background is also an important factor in detection of *pep* and CNO neutrinos. Typically, gamma induced background in the *pep* window [0.8-1.3 MeV] is larger than the corresponding background in the ^{7}Be window [0.25-0.8 MeV]. This fact may result in a redefinition of the fiducial mass for the observation of *pep* and CNO neutrinos. As an example, in 100 tons fiducial mass the external background in the [0.8-1.3 MeV] window is expected to be 1 events/day, compared with a neutrino signal of 2 events/day. Reducing the mass to 70 tons would bring the background down of a factor 10 while losing only 30% of the signal.

The third fundamental condition for the observation of *pep* and CNO neutrinos is a low internal cosmogenic background production. This topic is the main subject of this chapter.

6.1 Cosmogenic background in Borexino

Cosmogenic radioactive nuclides in Borexino are produced in reactions triggered by the residual muon flux. As originally pointed out in [131], the fundamental scale of the process is given by the rate of production of neutrons: neutrons are an important and ubiquitous by-product of cosmic ray-induced nuclear reactions.

A comprehensive review of the experimental results on neutron production in underground laboratories can be found in [130].

Martin Deutsch conjectured [132] that the underground production rate for all of the most significant cosmogenic nuclides out of a target mass composed of ^{12}C and ^{1}H could be guessed at from the neutron production rate alone. The list of cosmogenic nuclides produced by interactions with the target ^{12}C nuclide includes ^{8}Li, ^{9}Li, ^{11}Be, ^{8}B, ^{12}B and ^{9}C, all with mean lives below one minute and therefore they can be easily tagged with the parent muon. ^{7}Be is the cosmogenic radionuclide with the longest mean life, 77 days and ^{11}C also poses problems given its 30 minutes mean life.

The inclusive cross section for the production of several cosmogenic nuclides in muon-induced cascades was experimentally determined with a target experiment on a muon beam at CERN [107]. The muon shower was building up in 240 cm of concrete, followed by 200 cm of water and placed in front of the scintillator target. The use of two muon beams with energies 100 and 190 GeV allowed to extract information about the energy dependence of the inclusive

Isotopes	counts/day in the full energy range
^{11}C	14.6 ± 1.6
^{7}Be	(3.5 ± 0.4) x 10^{-1}
^{11}Be	< 0.027
^{10}C	1.9 ± 0.2
^{8}Li	(6.8 ± 1.6) x 10^{-2}
^{6}He	1.00 ± 0.03
^{8}B	(1.1 ± 0.2) x 10^{-1}
^{9}C	(7.6 ± 0.5) x 10^{-2}
$^{9}Li + ^{8}He$	(3.5 ± 0.5) x 10^{-2}

Table 6.1: Expected muon-induced background rates in Borexino (100 tons of scintillator), scaled from [107].

cross sections. The results in [107], reported in Table 6.1, shown that ^{7}Be is not among the most likely products of cosmic ray-induced reactions: its production rate at Gran Sasso depth is expected to be less than 0.1 events per day in 100 tons. Also, a precise measurement of the inclusive ^{11}C production rate was made available. At the mean energy of the muons at Gran Sasso Labs, the production rate would correspond to 14.6 events per day in 100 tons.

6.2 ^{11}C production in muon induced shower

^{11}C is a positron emitter with a 0.96 MeV end point; approximately 35% of its decays produce an energy deposit in the detector between 0.8 and 1.3 MeV.

Deutsch suggested that the only way to create ^{11}C is to knock a neutron off the ^{12}C nucleus, and highlighted the possibility of a three-fold coincidence to tag those ^{11}C events on a one-by-one basis. The detection technique basically consists in tagging in sequence cosmic muon, then in coincidence the induced neutron via capture on protons and finally, in coincidence with the neutron capture $\gamma_{2.2MeV}$, the positron emitted by the ^{11}C β^{+}-decay. However, there is also the possibility of creating a ^{11}C while ejecting a deuteron in a (p,d) exchange reaction. The (p,d) reaction would create an "invisible" channel for ^{11}C production since the nuclide produced through such process cannot be tagged with the three-fold coincidence. Similarly, reactions triggered by mesons can also produce decays in invisible channels, as noted later. Following is a list of the fundamental reactions that can produce ^{11}C, together with their cross section and references to specific studies. For all the reactions with a neutron in the final state, the energy threshold is 20MeV (i.e. the neutron binding energy in ^{12}C).

- ^{12}C(γ,n)^{11}C [108]: the cross section for the γ-ray induced process peaks at 7 mbarn around 23 MeV. The cross section value in the peak region, relatively large for an electromagnetic interaction, is due to the nuclear giant dipole resonance [109].

- ^{12}C(n,2n)^{11}C [110]: the cross section has a sharp peak (17 mbarn) around 33 MeV. At higher energies, we rely on the set of experimental data by Kim *et al.* [110] in the range 40-150 MeV, which is the only available for energies above 40 MeV.

- ^{12}C(p,p+n)^{11}C [112]: the cross section reaches a peak value of 98 mbarn at 40 MeV, and decreases to a plateau of 30 mbarn, constant up 1 GeV.

- ^{12}C(p,d)^{11}C [113]: the cross section has a threshold of 16 MeV and has been measured at 52 and 65 MeV (15 and 10 mbarn respectively). The only measurement available in the range above 100 MeV tells us that the cross section is in the range of a few μbarn, and therefore negligible.

- ^{12}C(π^-, π^-+n)^{11}C [114]: the cross sections exhibits a broad resonance peak, centered around the (3,3) resonance for the pion-nucleon interaction with a value of 70 mbarn at 190 MeV. Data are available up to 550 MeV, and show that the cross section reaches a plateau above 400 MeV. We assume that the cross section keeps a constant value at higher energies.

- ^{12}C(π^+, π+N)^{11}C [114]: the cross section exhibits a broad resonance peak in the same region, reaching 45 mbarn around 160 MeV. N in the final case stands for Nucleon and can be either a proton or a neutron. Data are available up to 470 MeV, and show that the cross section reaches a plateau above 350 MeV. We assume that the cross section keeps a constant value at higher energies.

- ^{12}C(e,e+n)^{11}C [115]: the direct interaction of electrons and positrons with a nucleus, through a virtual photon, is expected to have a small cross section, of the order of α (= 1/137) times the peak value of the cross section for real photons. The measured value of the cross section at 30 MeV is 15 μb.

- ^{12}C(μ,μ+n)^{11}C: the direct interaction of muons with a nucleus, through a virtual photon, is usually referred to as muon spallation. The cross section is equal to 58 μb for muons at 320 GeV. In the range 100-350 GeV the cross sections have values very close to the one just quoted, given the logarithmic dependence of the number of virtual photons N upon the energy E.

The cross sections for all the processes producing ^{11}C are shown in Figure 6.2. A more exhaustive description of the evaluation of the cross sections can be found in [116].

The relative weight of each reaction depends on the cross section but also on the number and type of prominent secondary particles produced in the μ-induced showers. Moreover, ^{12}C(p,d)^{11}C and ^{12}C(π^+, π+N)^{11}C reactions can not be tagged by the three-fold coincidence (invisible channels) since no neutron is emitted.

To evaluate the efficiency of the three-fold coincidence method, we simulated the production rates and ranges of all the secondary particles from the μ-induced showers. In the next section, I provide a full description of the simulation.

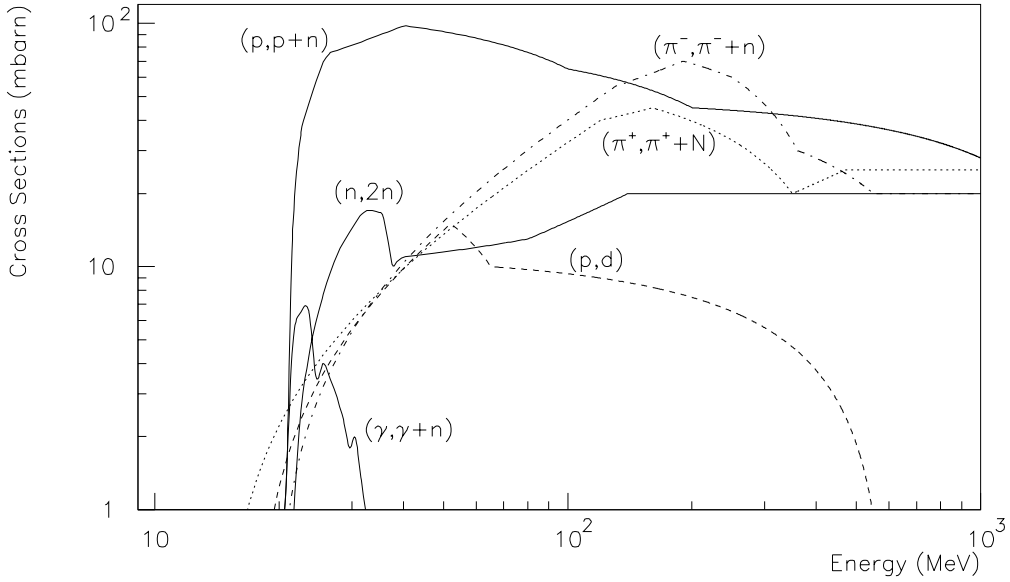

Figure 6.2: Cross sections for ^{11}C production as a function of energy.

6.3 The FLUKA simulation

FLUKA (version 2003.1b [126]) is the most complete code able to describe both hadronic and electromagnetic interactions up to 20 TeV.

The FLUKA code has been used by Wang et al. [130] to calculate the production rate of neutrons by muons in liquid scintillator at several depths, and has been found to reproduce very well experimental results. Recently, FLUKA has been used by Kudryavtsev et al. [129] to calculate the distance between the parent muon track and their point of capture on protons for neutrons produced in scintillator by muon-induced cascades at Gran Sasso depth, finding an excellent agreement with the experimental data from the LVD detector. In the context of this study, we use the particle transport code FLUKA to calculate the proton production rate, the neutron production rate and the range of neutrons - i.e. the distance between their origin and their capture point -. FLUKA also has the capability of calculating the cosmogenic nuclides production rate: the production of target associated particles and nuclear fragments in high-energy hadron-nucleus interaction is performed in FLUKA through one implementation of the Dual Parton Model for hadron-nucleus collisions, as described in [130].

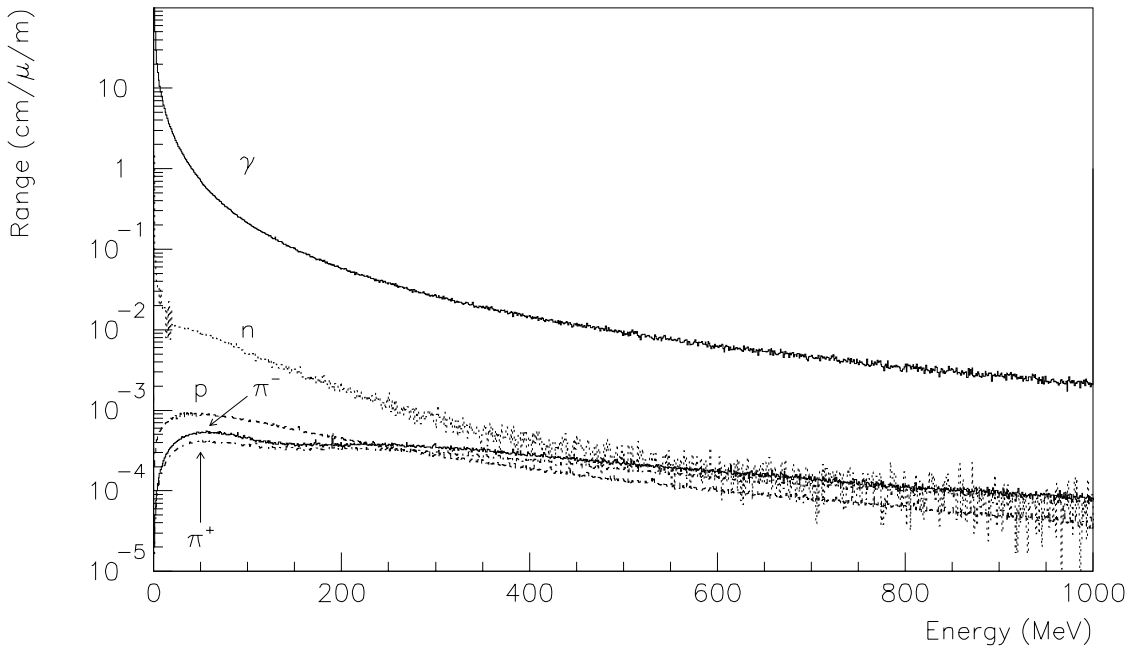

Figure 6.3: Cumulative range of secondaries generated in muon-induced showers. Results are quoted in cm of range per meter of μ track.

We compared successfully production rates for ^{11}C with the experimental values from Hagner et al [107].

The simulated geometry is simplified to a cylindrical water tank containing the vessel and the scintillator inside. The dimensions are the CTF ones.

The main processes which lead to the neutron production [130] at the depth of the Gran Sasso Laboratory are the following:

- muon-induced hadrons interacting with nuclei via a virtual photon producing a nuclear disintegration (usually referred to as *muon spallation*);
- muon elastic scattering with neutrons bound in nuclei;
- photonuclear reactions associated with electromagnetic cascades;
- secondary neutron produced following any of the above processes.

In ref. [129], V. A. Kudryavtsev et al. did not observe any significant difference in neutron production by positive and negative muons with energies above 10 GeV, proving the absence of the muon capture process.

We used FLUKA to calculate production rates and ranges of all the prominent secondaries, i.e. protons, neutrons, π mesons, and γ-rays. Moreover, we are interested in storing the

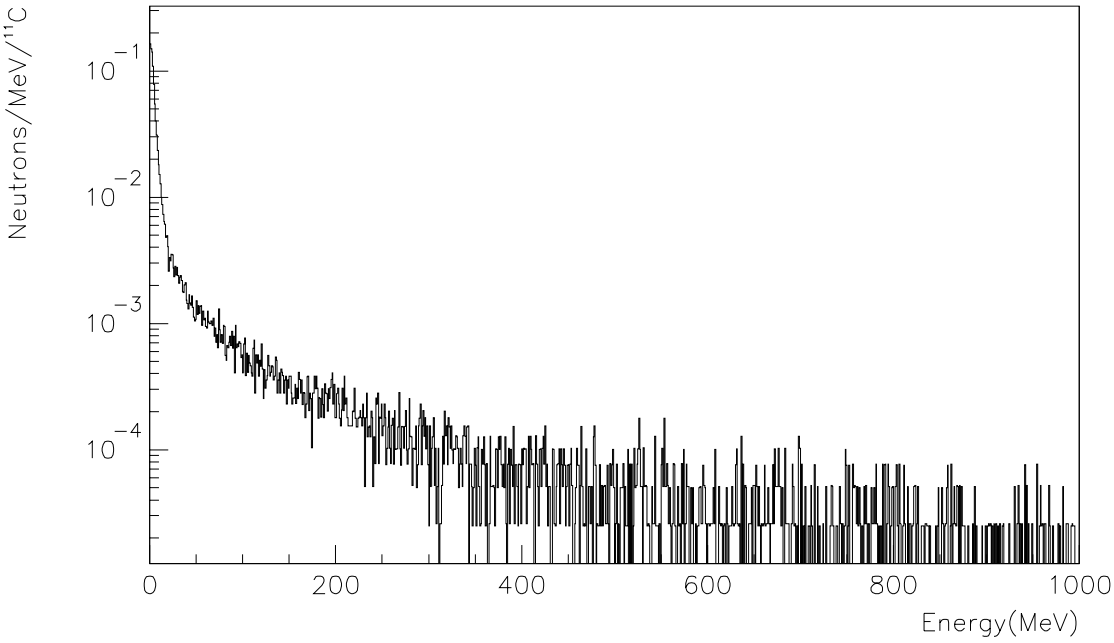

Figure 6.4: Energy distribution for neutrons produced in association with ^{11}C nuclides.

starting position of each produced neutron, the position and time of the neutron capture and the total deposited energy.

We simulated showers originating from 320 GeV negative and positive muons (average energy at Gran Sasso). The target material in the simulation was the solvent of the liquid scintillator for Borexino, trimethylbenzene (C9H12), with density 0.88 g/cm^3.

We tracked muons for 100 meters, and for each of the prominent secondaries we calculated the cumulative range of the particles as a function of the particle energy with a 10 GeV cutoff. The results are shown in Figure 6.3 for particles with energy below 1 GeV.

To check the reliability of the Monte Carlo we simulated the target experiment at CERN [107] with two μ-beams at 100 and 190 GeV and we successfully reproduced the measured cosmogenic nuclide rates.

6.4 Simulation results

We computed the ^{11}C production rate from each one of the interactions listed in Section 6.2. The production rate has been calculated by taking the energy convolution, for each of the possible interactions, of the cross sections with the range of the secondary particles responsible for inducing that particular interaction. Results are summarized in Table 6.2. The quoted production rate in the invisible channels rate has been calculated by adding the rate from

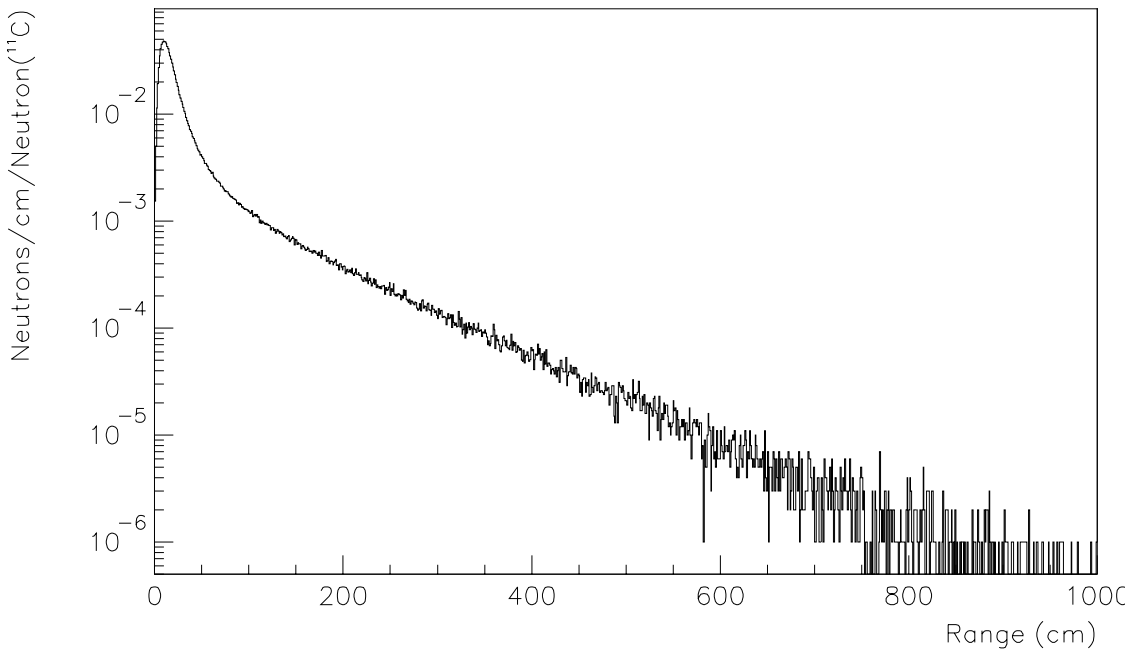

Figure 6.5: Range of neutrons produced in association with ^{11}C nuclides.

the ^{12}C(p,d)^{11}C reaction to 2/3 of the rate from the ^{12}C(π^+,π+N)^{11}C reaction. The error quoted in Table 6.2 accounts for the systematic error, which is dominated by the uncertainty in the knowledge of the cross section for the process ^{12}C(π^+,π+N)^{11}C. Our best estimate for the systematic error is 50% of the production rate in such channel, which is between 5% and 7% of the total production rate depending on the energy. The fractional statistical error associated with our Monte Carlo calculation is 0.6% and is negligible with respect to the systematic error.

We also calculated the production rates for positively charged muon (μ^+) at 320 GeV. The difference in the production of ^{11}C, for all of the channels in consideration, by μ^+ and μ^- at the energy of 320 GeV is within the statistical error of our Monte Carlo calculation. We conclude that the dependence of the cross section for ^{11}C production on the sign of the charge of the muons is negligible.

As shown in Figure 6.3, the particle content of μ-induced showers is, as expected, dominated by γ-rays. In particular, at the resonant energy for the giant dipole resonance of ^{12}C - 23 MeV - the cumulative range of γ-rays is three orders of magnitude larger than the corresponding values for neutrons, and five orders of magnitude larger than for other hadrons. As a consequence of this fact, the dominant process for the production of ^{11}C nuclides is the (γ,n) exchange reaction, accounting for 60% of the total production rate. Other channels with a neutron in the final state account for an additional 35% of the total production rate. The rate of ^{11}C production in the two invisible channels, corresponding to the (p,d) and the (π^+,π^0+p) exchange reactions, accounts for only about 5% of the total production rate.

E_μ (GeV)	100	190	285	320	350
Interaction		Rate ($10^{-4}/\mu$/m)			
^{12}C(p,p+n)^{11}C	1.8	3.2	4.9	5.6	5.7
^{12}C(p,d)^{11}C	0.2	0.4	0.5	0.6	0.6
^{12}C(γ,n)^{11}C	19.8	27.0	34.1	46.6	38.4
^{12}C(n,2n)^{11}C	1.4	2.6	3.8	4.4	4.6
^{12}C(π^+,π+N)^{11}C	1.0	1.8	2.8	3.2	3.3
^{12}C(π^-,π^-+n)^{11}C	1.3	2.3	3.6	4.1	4.2
Invisible	0.9	1.6	2.4	2.7	2.9
Total	25.4	37.3	49.7	54.4	57
Measured	22.9±1.8	36.0±2.3			
Extrapolated			47.8	51.8	55.1

Table 6.2: Production rates for ^{11}C in muon induced showers. The calculated total production rates are compared with the experimental values available at 100 and 190 GeV, and with the extrapolated values at the mean muon energy for several energy (320 GeV is the mean muon energy in Borexino). The invisible channels rate has been calculated by adding the rate from the ^{12}C(p,d)^{11}C reaction to 2/3 of the rate from the ^{12}C(π^+,π+N)^{11}C reaction.

Deutsch's idea of eliminating the ^{11}C events by looking at the three-fold coincidence turns out to be still valid even in presence of invisible channels, as the production rate of ^{11}C nuclides without a neutron in the final state accounts only for 1 over 20 of the nuclides produced. In the next section we will quantify the effectiveness of the ^{11}C background reduction technique based on the double muon+neutron tagging.

6.5 ^{11}C reduction techniques

At least one neutron is produced in association with 95% of the ^{11}C nuclides. This fraction of the ^{11}C background can be lowered with the muon+neutron tagging. The remaining 5% cannot be reduced with this technique.

In order to suppress ^{11}C background, one needs to identify the position and time of each neutron created by a muon-induced shower and then captured in the scintillator. Once the neutron capture time and position are known, one needs to apply a cut in space and time around every capture point. The event within a time Δt from the double muon+neutron coincidence and inside a sphere of radius r from the neutron capture point are rejected. The length of time Δt for which events are rejected must be set equal to a few times the mean life of ^{11}C. Note that the information carried by the neutron capture does not tell us about the position of the ^{11}C birthplace. Therefore, it is important to gauge the radius r of the spherical cut to a few times the average neutron range. For this reason, we calculated with Monte Carlo methods the energy distribution of the neutrons produced in association with ^{11}C nuclides.

The distribution shown in Figure 6.4 was used to source neutrons in a second FLUKA

simulation, which was used to compute the distribution of the range of neutrons produced in association with ^{11}C, as shown in Figure 6.5.

The average energy of neutrons produced in association with ^{11}C is much lower than the average energy of all neutrons produced in muon-induced showers: this is due to the dominant production mechanism being the photo-neutron reaction at the giant dipole resonance of ^{12}C at 23 MeV.

Correspondingly, the average range of neutrons associated with ^{11}C production is also much lower than the average range of all the neutrons produced in the shower. We also note that a neutron created in association with a ^{11}C nuclide production can trigger nuclear reactions knocking off other neutrons: our calculation gives an average number of 1.2 neutrons captured per neutrons produced in association with a ^{11}C nuclide. "Second" neutrons can affect the three-fold coincidence efficiency since they produce another ^{11}C nuclide after the time gate of the μ-$\gamma_{2.2MeV}$ coincidence is closed.

The efficiency ε in rejecting ^{11}C events tagged with the coincidence muon+neutron is equal to the combined efficiencies for the cut in space, $\xi(r)$, and in time, $\eta(t)$:

$$\varepsilon(r,t) = \xi(r) \times \eta(t) \tag{6.1}$$

where $\eta(t)$ is the efficiency for the rejection of ^{11}C events when a cut in time for a time span equal to t is applied around the neutron capture point. Given the expected decay distribution of ^{11}C, we obtain:

$$\eta(t) = 1 - e^{-t/\tau} \tag{6.2}$$

where τ is the mean life of ^{11}C, 30 minutes. $\xi(r)$, in equation 6.1, is the rejection efficiency for ^{11}C when a cut in space is applied around the neutron capture point, corresponding to a sphere of radius r centered around the capture point position.

Given the distribution *n(r)* for the range of neutrons, the efficiency for the rejection is equal to:

$$\xi(r) = \frac{\int_0^r n(s)ds}{\int_0^\infty n(s)ds}. \tag{6.3}$$

We define *R(r,t)* as the ratio of the *pep*+CNO neutrino signal (S) to the background rate from residual ^{11}C (B_{C11}) after suppression of all ^{11}C events identified through the the muon+neutron coincidence. Both numerator and denominator are computed in the 0.8-1.3 MeV energy window.

Assuming a trace contamination B_t of 0.6 events/day (as discussed in previous section), the general expression for R is:

Dead Volume-Time Fraction *D(r,t)*	Signal-To-Background ratio *R(r,t)*
5%	1
20%	1.2
50%	1.5

Table 6.3: Fraction of the dead volume-time in order to reach the correspondent signal-to-background ratio. C background is assumed in the *pep* and CNO neutrinos energy range [0.8 - 1.3] MeV and a residual activity from trace contamination of 0.6 events/day.

$$R(r,t) = \frac{S}{B_t + B_{C11} \times (\varepsilon(r,t) + \alpha)} \tag{6.4}$$

where S is the neutrino signal, B_{C11} and B_t the ^{11}C and trace contaminations, respectively, and $\alpha \sim 0.05$ is the fraction of ^{11}C production rate in invisible channels.

The dead mass-time fraction *D(r,t)* is defined as the fraction of data taking lost due to the space and time cuts around a neutron capture event. Treating η and ξ as independent variables, t and r can be derived by inverting equations 6.2 and 6.3, respectively. We can then compute the dead mass-time fraction *D(r,t)* corresponding to the chosen values of the cuts and as:

$$D(r,t) = 1 - e^{(\frac{r}{R})^3 \cdot \frac{t}{T} \cdot N} \tag{6.5}$$

where N is the number of neutrons in the time of observation T in the detector (R is the radius of the fiducial volume).

Figure 6.6 shows the correlation between the signal to reduced background ratio *R(r,t)* and the dead mass-time fraction *D(r,t)* for Borexino, as a function of spatial (ξ) and time (η) efficiencies for ^{11}C events rejection. In Table 6.3, example values of the dead mass-time fraction *D(r,t)* for Borexino are reported for fixed and given values of the ratio *R(r,t)* between signal and reduced background. The values are calculated by minimizing the dead mass-time fraction *D(r,t)* while keeping the product of the two efficiencies, constrained to the value of corresponding to the chosen value of *R(r,t)*.

6.6 Concluding remarks

The efficiency for rejection of the ^{11}C background is calculated making simple assumption on the basis of published data and Monte Carlo calculations. The results outlined in this section should be regarded mainly as a proof of concept.

From the values listed in Table 6.3, we see that in Borexino a measurement with signal to background ratio, *R(r,t),* 1.2 is indeed possible, with a dead mass-time of only 20%. A

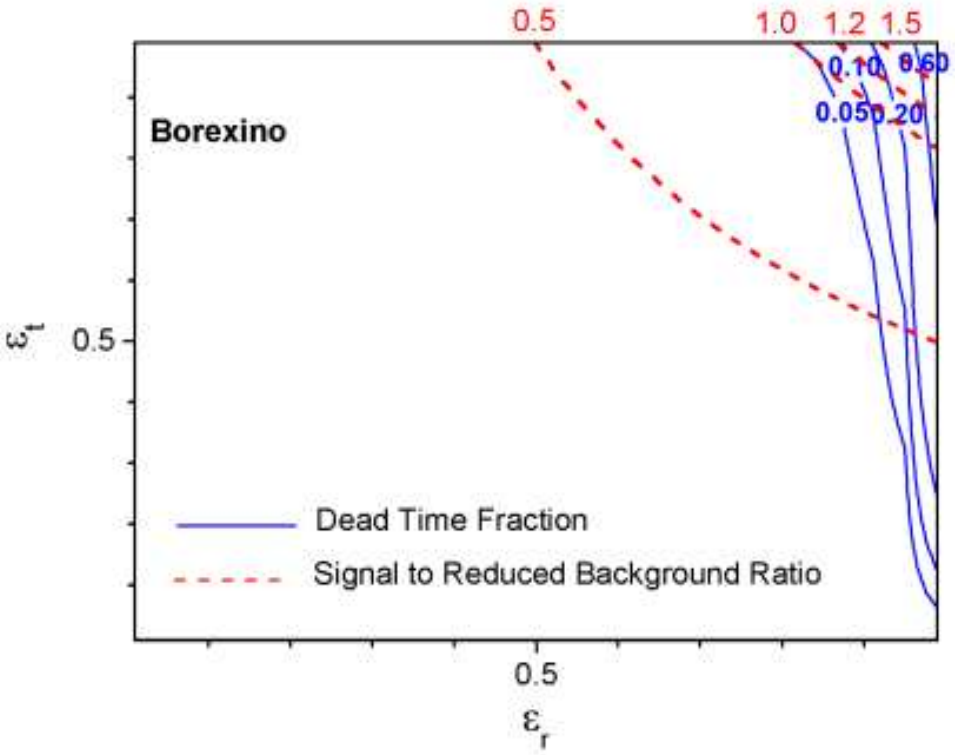

Figure 6.6: Correlation between the signal to reduced background ratio, *R(r,t)*, and the dead mass-time fraction, *D(r,t)*, for Borexino, as a function of spatial (ξ) and time (η) efficiencies of ^{11}C events rejection for Borexino. Isocontours for the ratio *R(r,t)* are represented with dashed lines. Isocontours for the dead mass-time fraction *D(r,t)* are represented with solid lines. ^{11}C background is assumed in the *pep* and CNO neutrinos energy range [0.8 - 1.3] MeV and a residual activity from trace contamination of 0.6 events/day.

measurement with a signal to background ratio of 1.5 is also possible, sacrificing as much as 50% of data taking. These figures of merit are achieved just by identifying the ^{11}C events on a one-by-one basis. On top of this, there is also the possibility to improve the signal to background ratio by statistical subtraction. To that end, the three-fold coincidence with the muon and the neutron will be instrumental as it will allow to determine precisely the fraction of ^{11}C events leaking through the cuts.

Actually, Borexino is performing a more detailed study of the parent muon tracks and of the related neutron captures in order to determine their efficiencies in rejection of ^{11}C background. In particular, we intend to exploit the information about the μ-track provided by the muon identification system (inner and outer detector). A second cylindrical volume cut, indeed, intersecting the spherical cut around the $\gamma_{2.2MeV}$ can further reduce the loss of volume-time detector, *D(r,t)*.

In conclusion, we found that invisible channels (no neutron emission) affect the ^{11}C production for only $\sim$ 5%. Moreover, FLUKA code, tested simulating the experiment at CERN [107], shows that the rejection of ^{11}C background requires a contained loss of the detector volume-time. The next step is to implement the muon identification system in order to reach a higher signal to background ratio, but, already with the presented results, we have shown that Borexino has the potential to open the window to the *pep* and CNO spectroscopy.

In order to demonstrate that the three-fold coincidence is a powerful tool for discriminating the ^{11}C background, it has been applied on the CTF data. A detailed description of analysis and results is reported in the next chapter.

Chapter 7

In situ ^{11}C production by cosmic μ in CTF

7.1 Introduction

As already mentioned in the previous chapter, the main challenge of correlating the ^{11}C with the preceding neutron is the long ^{11}C life time of $\tau = 29.4$ min. Two requirements have to be overcome for a successful application of a ^{11}C rejection cut:

- there should be no convective currents on the time scale of hours moving the ^{11}C atom away from its production site;
- the location of the ^{11}C production location needs to be reconstructed with sufficient accuracy.

Recent data from the KamLAND detector have shown that there are no convective currents on the time scale of the ^{222}Rn decay ($t_{1/2} = 3.6$ d). This stability is achieved by keeping a temperature gradient over the whole detector of about 4 degrees Kelvin.

The expected cosmogenic nuclide rates, scaled for CTF from the target experiment on the muon beam at CERN (already described in Section 6.1), are reported in Table 7.1. The major expected contribution involves ^{11}C which represents 80% of the total rate of the μ-^{12}C reaction products. Investigating only the *pep*-ν energy region (0.8 - 1.4 MeV), the ^{11}C contamination represents more then 99% of all the μ-^{12}C reaction products.

In this chapter, I will show that the ^{11}C decays can be tagged in CTF with high efficiency, thus indicating that ^{11}C discrimination should be feasible in Borexino by a simple neutron correlated space cut. Together with the muon track reconstruction, we will have the possibility to cross calibrate the cut efficiencies and to discriminate the ^{11}C background with an efficiency sufficient to open the window to *pep* and CNO neutrino spectroscopy.

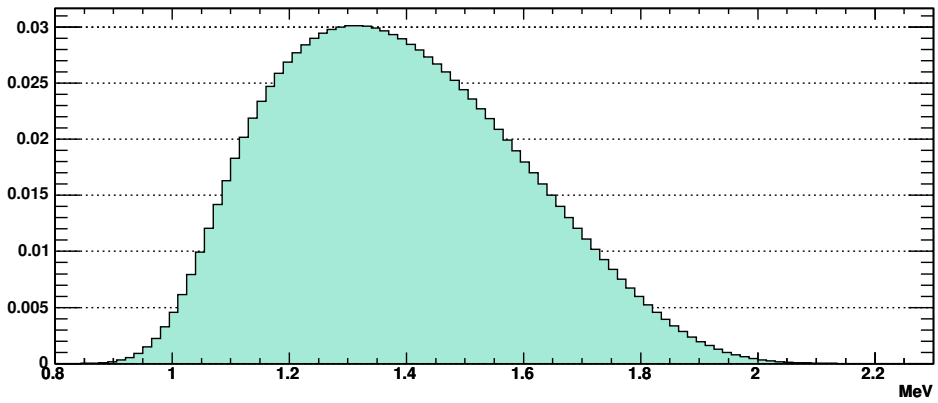

Figure 7.1: Theoretical spectrum of the ^{11}C β^+ decay in CTF convoluted with the energy resolution of the detector.

Isotopes	counts/day in the full energy range
^{11}C	0.54 ± 0.06
^{7}Be	(1.3 ± 0.1) x 10^{-2}
^{11}Be	$< 10^{-3}$
^{10}C	(7.2 ± 0.8) x 10^{-2}
^{8}Li	(2.5 ± 0.6) x 10^{-3}
^{6}He	(3.7 ± 0.1) x 10^{-2}
^{8}B	(4.0 ± 0.7) x 10^{-3}
^{9}C	(2.8 ± 0.9) x 10^{-3}
$^{9}Li + ^{8}He$	(1.3 ± 0.2) x 10^{-3}

Table 7.1: Expected muon-induced background rates in CTF (3.7 tons of scintillator), scaled from [107].

7.2 Data Sample

The analyzed data belong to the period of detector stability from 24th June 2002 (run 2190) after the Si-Gel Column test to 24th May 2004 (run 2414). The effective data taking period is equal to 315 days.

The selection of "good" runs has been done in a very conservative way following the logbook indications, avoiding all runs in which electronic problems, laser or α/β tests, blackouts, or manipulations of the scintillator occurred. Moreover 13 runs with an anomalous high neutron-like capture rate (between 5-10 c/d) have been discarded. The discarded runs are listed in Table B.1.

7.3 ^{11}C detection technique

The cosmic muons and their secondary particles produce ^{11}C in the scintillator through the net reaction:

$$\mu +^{12} C \rightarrow n +^{11} C. \tag{7.1}$$

The cosmic muons are selected among the events tagged by the muon veto which saturates the electronics. The efficiency is ~ 1. At a depth of 3800 mwe, where the detector is located, cosmic muons have an average energy of $\langle E_\mu \rangle$ =320 $\pm 4_{stat.}$ $\pm 11_{syst.}$ GeV (as measured by the MACRO collaboration [125]) and they produce enough light to fire the μ-detector.

In a second step, the muon-induced neutron interacts with the hydrogen of the scintillator with a capture time of $\sim$200 μs through the reaction

$$n + p \rightarrow d + \gamma \tag{7.2}$$

producing the characteristic $\gamma_{2.2MeV}$. The $\gamma_{2.2MeV}$s are tagged by opening a gate (10 μs - 1 ms) following the detection of the muon. The energy spectrum of the so selected $\gamma_{2.2MeV}$ (Figure 7.2) is the superposition, as expected, of two components: the full energy deposits at 2.2 MeV and lower energy tail of Compton scattered and partially escaped gammas. The capture time obtained from the fit to the distribution of Figure 7.2 is:

$$\tau = 214 \pm 11\,\mu s. \tag{7.3}$$

The ^{11}C β^+ decay is characterized by a long mean life of τ = 29.4 min. In order to tag it, a time gate of 300 min ($\sim$10 τ) is opened after each detected $\gamma_{2.2MeV}$ with E $>$ 1.8 MeV in order to increase the selection of the only contained events. The efficiency $\varepsilon_{\gamma_{2.2MeV}}$ of the $\gamma_{2.2MeV}$ selection has been derived by a Monte Carlo simulation explained in Section 6.5.

The positron deposits energy in the scintillator between 0 and 0.96 MeV and annihilates

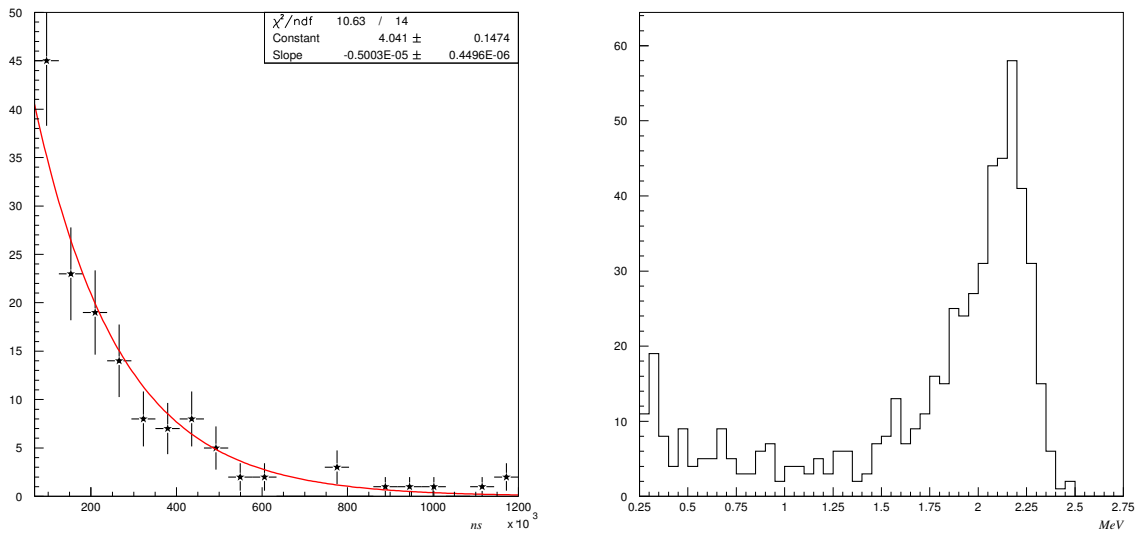

Figure 7.2: Fit of the capture time in the (n,p) reaction and energy spectrum of $\gamma_{2.2MeV}$'s from muon-induced neutron from CTF. The long low energy tail is due to $\gamma_{2.2MeV}$'s which escape the vessel.

with the emission of two gammas of 0.511 MeV. The detector measures the total deposited energy, i.e., in the range [1.02 - 1.98] MeV. A small distortion in the energy spectrum happens when a $\gamma_{0.511MeV}$ escapes the vessel. A $\gamma_{0.511MeV}$ however has a mean free path in the scintillator of only $\sim$ 7 cm and a radial cut of 80 cm around the center of the vessel cm avoids such distortion.

In order to maximize the signal-to-background ratio, due to the presence of other contaminants like ^{210}Bi, ^{214}Bi and ^{40}K, a more restrictive energy range definition is applied: the analyzed energy region [1.1 - 1.65] MeV collects the ε_{en} = 82% of ^{11}C decays.

7.4 Data Analysis

The analyses are performed on the time evolution of the events in the ^{11}C energy window assuming as reference the VAX time of the $\gamma_{2.2MeV}$ event which opens the time gate.

The purposes of the analyses are twofold:

- confirming the presence of the ^{11}C events by fitting their mean life
- estimating the number of produced ^{11}C.

7.4.1 "*First event*" analysis: detection of lifetime τ

The "first event" analysis is based on the selection of the first event in time following each $\gamma_{2.2MeV}$ detected within the radial cut. "True" (^{11}C) events follow the decay distribution. They can be discriminated from random coincidences ("false") which follow the Poisson distribution.

We can identify three sets of events:

- true (A) and false (B) events coupled to the fraction (α) of $\gamma_{2.2MeV}$s originated by neutron spallation in ^{11}C production;
- events (C) coupled to the rest (1 - α) of the detected $\gamma_{2.2MeV}$s, identifiable as random coincidences.

The probability to detect an event belonging to set A (or B) at time t_1 is composed by:

- the probability to have no random event before t_1:

$$P_1 = e^{-b\,t_1} \tag{7.4}$$

  where b is rate of the random;

- the probability to have no ^{11}C event before t_1:

$$P_2 = e^{-t_1/\tau} \tag{7.5}$$

  where τ is the ^{11}C mean life;

- the probability to have a ^{11}C event in t_1:

$$P_3 = \frac{1}{\tau} \tag{7.6}$$

- the probability to have a random event in t_1:

$$P_4 = b \tag{7.7}$$

The probability related to select an event belonging to set C is Poissonian:

$$P_5 = b \cdot e^{-bt_1}. \tag{7.8}$$

Composing and summing all the probabilities, the final distribution is defined by:

$$\begin{aligned} P(\alpha,\tau,b) &= \alpha \cdot P_1 \cdot P_2 \cdot (P_3 + P_4) + (1-\alpha) \cdot P_5 \\ &= \alpha\,(b + 1/\tau)\,e^{-(b+1/\tau)\,t} + (1-\alpha)\,b\,e^{-b\,t} \end{aligned} \tag{7.9}$$

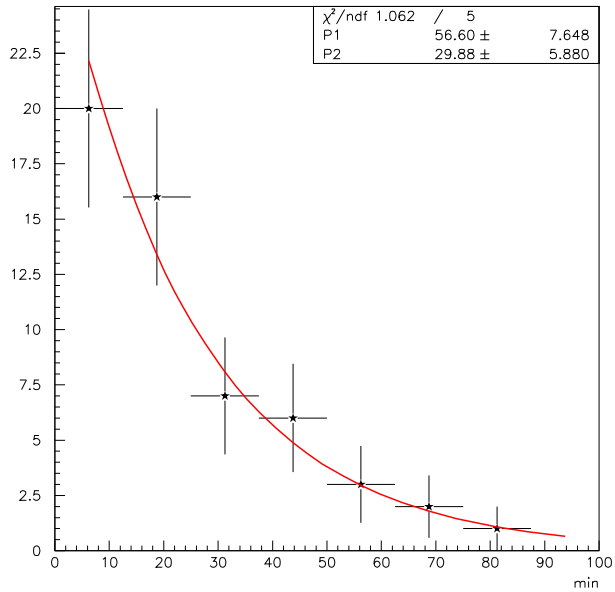

Figure 7.3: Fit of the "first events" sample in a spherical cut around the $\gamma_{2.2MeV}$ of 0.7 m.

and, defining the number of events N , the fit function is:

$$F(N, \alpha, \tau, b) = N \times P(\alpha, \tau, b). \tag{7.10}$$

The rate b of random coincidences is fixed in the fit (Figure 7.3) to the measured rate in the time gate after 2 hours from detecting a muon event within the radial cut. N is fixed to the number of events in the selected sample.

The fit function identifies a decay constant of 30 $\pm$ 11 min which is consistent with the hypotheses of *in situ* produced ^{11}C decay. Despite the high statistical error, the "first event" analysis provides a first confirmation on the possibility to detect and tag the ^{11}C contamination.

7.4.2 "*All event*" analysis: detection of produced ^{11}C rate

"All event" analysis is a quantitative analysis devoted to measure the ^{11}C activity.

The time profile of all events following each detected $\gamma_{2.2MeV}$ in a time gate of 300 min is fitted by:

$$F(t) = \frac{N}{\tau} e^{-\frac{t}{\tau}} + B. \tag{7.11}$$

which includes the decay rate of ^{11}C and a constant background B. The applied radial cut

is in the range [0.7 - 0.8] m which corresponds to a sensitive mass range of [1.25 - 1.90] tons (below 0.7 m the statistics is too low).

As expected, if τ is a free parameter, the fit returns a value (28.4 $\pm$ 16.4 min) compatible with the ^{11}C decay constant but with a very large error ($\sim$ 58%).

Fixing τ to the literature value (29.4 min), the fit identifies $N = 45 \pm 12$ events (Figure 7.4) in $m_R = 1.3$ ton of scintillator (radial cut R = 0.7 m) in T = 315 days and in the energy window [1.1 - 1.65] MeV.

In order to obtain the ^{11}C rate, we have to include all the detection efficiencies:

- Geometrical efficiency (ε_r): N must be normalized to the entire CTF volume taking into account possible non uniformity of the ^{11}C spatial distribution.
- Normalization over the entire ^{11}C energy spectrum: ε_{en}= 0.82.
- Neutrons detection (ε_n): neutrons can escape the vessel without opening the time gate.
- $\gamma_{2.2MeV}$ detection (ε_γ): $\gamma_{2.2MeV}$ from neutron capture can partially deposit energy outside the vessel.
- Invisible ^{11}C production channels: ε_{inv}= 0.95 (see Section 6.2).

Muon and $\gamma_{0.511MeV}$ (from positron annihilation) detection efficiencies are assumed to be equal to 1. The radial cut, indeed, drastically reduces the possibility that $\gamma_{0.511MeV}$ can escape the vessel since it covers a mean free path of few centimeters.

The total rate is then defined by:

$$\begin{aligned} r &= \frac{N}{T \times \varepsilon_{en} \times \varepsilon_n \times \varepsilon_r \times \varepsilon_\gamma \times \varepsilon_{inv}} \\ &= \frac{0.18 \pm 0.05}{\varepsilon_n \times \varepsilon_r \times \varepsilon_\gamma} \end{aligned} \tag{7.12}$$

To estimate ε_n, ε_γ and ε_r, we used a Monte Carlo simulation described in the next section

7.5 Monte Carlo simulation

The simulation described in Section 6.3 for studying the Borexino potential of rejecting the ^{11}C contamination was focused on the physics of the μ-induced ^{11}C without taking into account the effects of the detector geometry. In order to study the effects of the small scintillator volume and of the water buffer of CTF, a dedicated and more exhaustive simulation is required. Moreover, we included the tracking of the neutron capture $\gamma_{2.2MeV}$ which shifts the neutron detection point, not studied in the Borexino simulation.

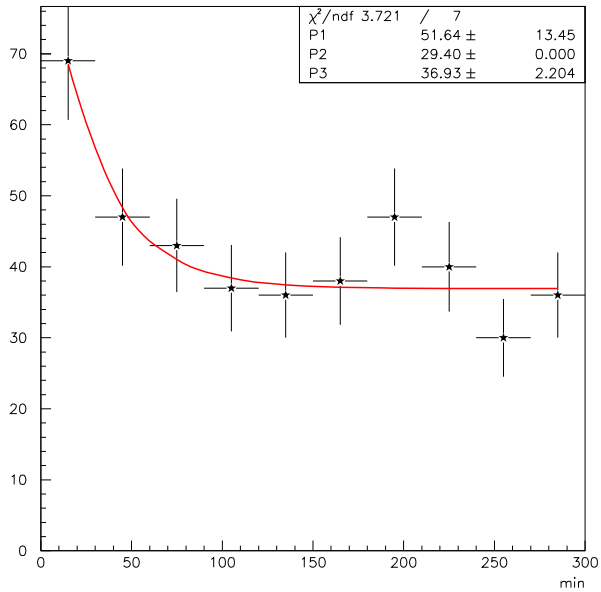

Figure 7.4: Fit of the "all events" sample.

The Monte Carlo strategy consists in simulating the detector geometry and materials, and a downward-ray of negative muons with a fixed energy of 320 GeV (the averaged muon energy at the depth of the Gran Sasso Lab) uniformly distributed over all the water tank of CTF. We used FLUKA (version 2003.1b [126]) already described in Section 6.3.

The neutrons produced in scintillator and in water are tracked until they are captured. Each capture position is then inserted in the official tracking and reconstruction codes of CTF as the $\gamma_{2.2MeV}$ starting position. The tracking code requires that the starting position of the $\gamma_{2.2MeV}$ must be ahead the photomultiplier which correspond to a sphere of 2.7 m radius from the center of the detector.

We assume that the ^{11}C event is located exactly in the neutron production point. Indeed the positron annihilation $\gamma_{0.511MeV}$ covers only a path of a few centimeters and, as already demonstrated by KamLAND, fluid dynamics effect in the time scale of the analysis (few hours) can be neglected. The ^{11}C event position is then not tracked neither reconstructed. The consequent error has been evaluated and included in the systematics.

The output of the FLUKA simulation has been adapted to be read by the CTF tracking code for simulating $\gamma_{2.2MeV}$s.

The tracking code simulates the conversion of each energy deposit into optical photons. The optical photons are propagated inside the detector and tracked up until they are absorbed in the detector material or detected on the PMT's. The tracking code takes into account the

Photomultiplier Tubes:	
Cathode radius	0.095 m
Curvature radius	0.11 m
Time jitter	1 ns
Quantum efficiency	20%
Practical coefficient	0.6
Light Guides:	
Radius of entry aperture	0.157 m
Radius of exit aperture	0.095 m
Length	0.230 m
Reflection coefficient	90%
Effective coverage	30.6%
Liquid Scintillator:	
Formula	PC+PPO (1.5 g/l)
Refractive index	1.505
Photon yield	1.68 x 10^4

Table 7.2: Parameters in the Monte Carlo tracking

following processes studied in CTF [51]:

- scintillation light production (decay time and emission spectra of PC+PPO),
- absorption and reemission process in the scintillator,
- diffusion on the nylon vessel,
- Rayleigh elastic scattering in the scintillator and in the buffer,
- reflection on surfaces and the quantum efficiencies of pseudocumene, PPO and the phototubes.

The light collected on the photocathodes is then converted into a time and charge signal, thus simulating the real data collection. The output for the CTF tracking code is properly formatted to be read by the reconstruction code (Section 5.2).

7.6 Results and systematics

A comparison between the expected and the measured neutron capture time allows to cross check the reliability of the simulation. The neutron capture time (τ) depends mainly on the number of hydrogen atoms per molecules in water and PC (Table 7.3). Carbon and oxygen targets, indeed, have a cross section of two orders of magnitude lower than the hydrogen and don't affect significantly τ. We can assume thus that in CTF the capture time is mainly composed by two components: a fast one due to the capture in water (from simulation, τ_{sim}

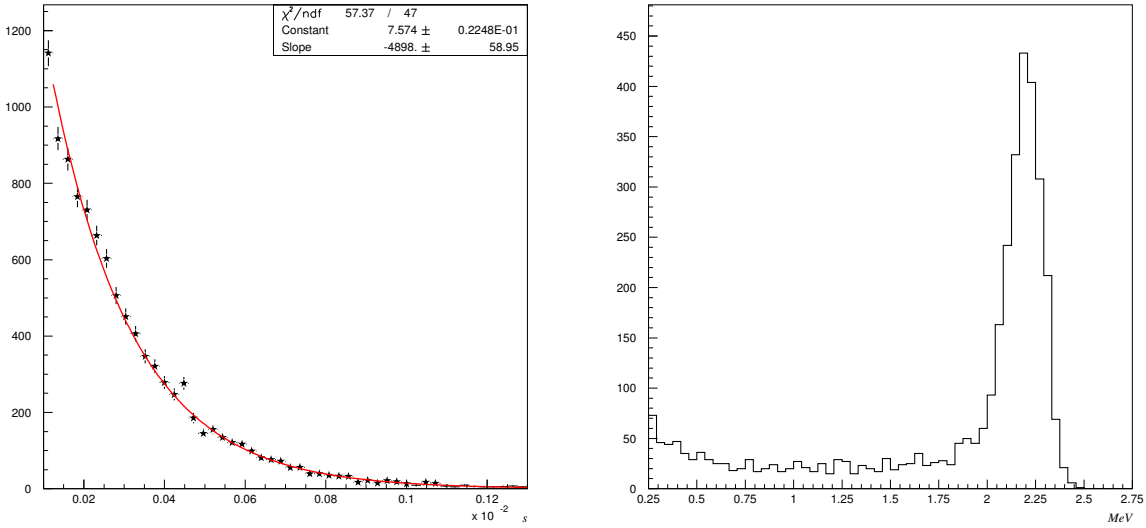

Figure 7.5: (a) Fit (red line) of the capture time for the n-H reaction. (b) Energy spectrum of the $\gamma_{2.2MeV}$ from muon-induced neutron simulated in CTF (right).

	Water	PC
Molecular weight	18	120
Hydrogen atoms per molecules	2	12
Hydrogen mass fraction [%]	12	10
Density $[\frac{g}{cm^3}]$	1	0.87
n $[10^{22} \cdot cm^{-3}]$	7.2	5.1
τ_{sim} $[\mu s]$	204 $\pm$ 2	260$\pm$ 2

Table 7.3: Physical quantities affecting the mean capture time of thermal neutrons in water and in PC. The capture time τ_{sim} is obtained fitting the simulated distribution in water and in PC.

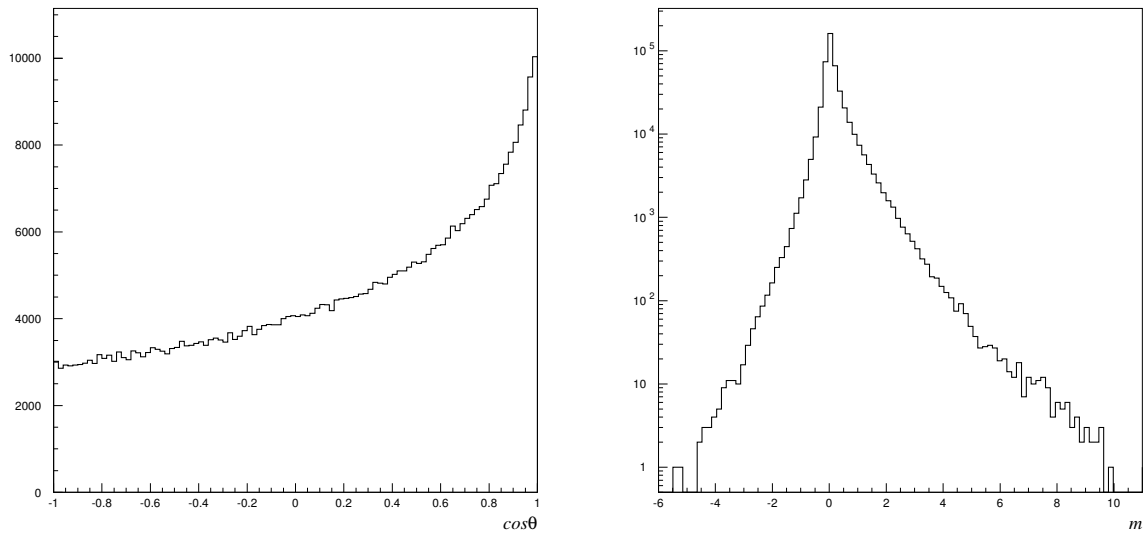

Figure 7.6: (a) Neutron angular distribution with respect to the muon direction . (b) Distance covered by neutrons along the z-axis (muon direction).

=204 ± 1) and a slow one due to the capture in PC (τ_{sim} =260 ± 2). A global fit of the capture time distribution in water and in PC (Figure 7.5) for all the neutrons inside a sphere of 3 m from the center of the detector (approx the distance of the PMT's), we obtain τ_{sim} = 207 ± 1 μs. The value measured in CTF (as reported in Section 7.1) is equal to τ_{meas} =214 ± 11 μs . The agreement of τ_{meas} with τ_{sim} within 1σ confirms of the reliability of the simulation.

From the FLUKA simulation, it turns out that at least a ^{11}C nuclide is produced in association with 31% of neutrons. In the Borexino simulation (Section 6.5), the estimated probability was found lower (13%). The difference is due to the small size of CTF, which limits the propagation of the μ-induced shower and thus the secondary neutron production.

The energy spectrum in Figure 7.7 shows that 90% of the neutrons has a kinetic energy below 250 MeV and more than 50% has energy below 40 MeV. The neutron angular distribution with respect to the muon direction (Figure [7.8]), as expected, is forward peaked, partially smoothed by the contribution of the secondary neutrons. The anisotropy increases at the increasing of the energy as shown in Figure 7.8. The multiplicity depends strongly on the size of the detector: up to 400 neutrons can be produced along the maximum distance that a muon can covered in CTF (about 10 m). However 90% of the muons produces up to 40 neutrons and more than 50% generates less than 5 neutrons.

It's interesting to observe that 83% of the neutrons simulated in CTF covers a distance less than 1 m (Figure 7.9) but, taking into account that $\gamma_{2.2MeV}$ in scintillator covers a distance of

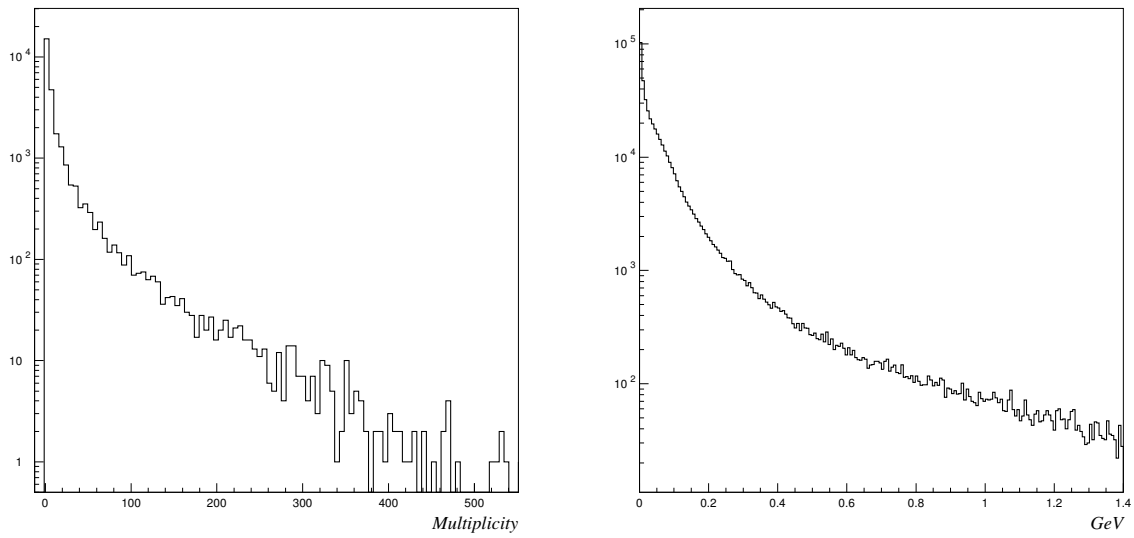

Figure 7.7: (a) Neutron multiplicity. (b) Energy distribution of the neutrons.

20-30 cm, the cumulative probability to detect a neutron as function of the covered distance is reduced and at 1 m is equal to 74%.

The energy cut on the $\gamma_{2.2MeV}$ spectrum is correlated to the radial cut. $\gamma_{2.2MeV}$ events belonging to the peak centered on 2.2 MeV, indeed, deposit all the energy inside the vessel and have a higher probability to be contained in the fiducial volume than events in the tail (Figure 7.5).

In order to derive the correlated efficiency $\epsilon(\varepsilon_r, \varepsilon_\gamma)$, we apply first the cut on the $\gamma_{2.2MeV}$ energy and then the radial cut, as we did on the real data (Section 7.3):

- I) cut on the $\gamma_{2.2MeV}$ energy spectrum (E $>$ 1.8 MeV);
- II) radial cut (r $<$ 0.7 m).

The total detection efficiency is then equal to:

$$\varepsilon_{tot} = \varepsilon_{en} \times \varepsilon_{inv} \times \varepsilon_n \times \epsilon(\varepsilon_r, \varepsilon_\gamma) = 0.23. \tag{7.13}$$

The main systematics sources are two: the uncertainties on the scintillator mass determination and on the light yield measurement from the ^{14}C energy spectrum which affects both the ^{11}C and the $\gamma_{2.2MeV}$ energy spectra (see Section 5.4). Systematic errors are reported in Table [7.4].

Inserting (7.13) in (7.12), the ^{11}C rate results:

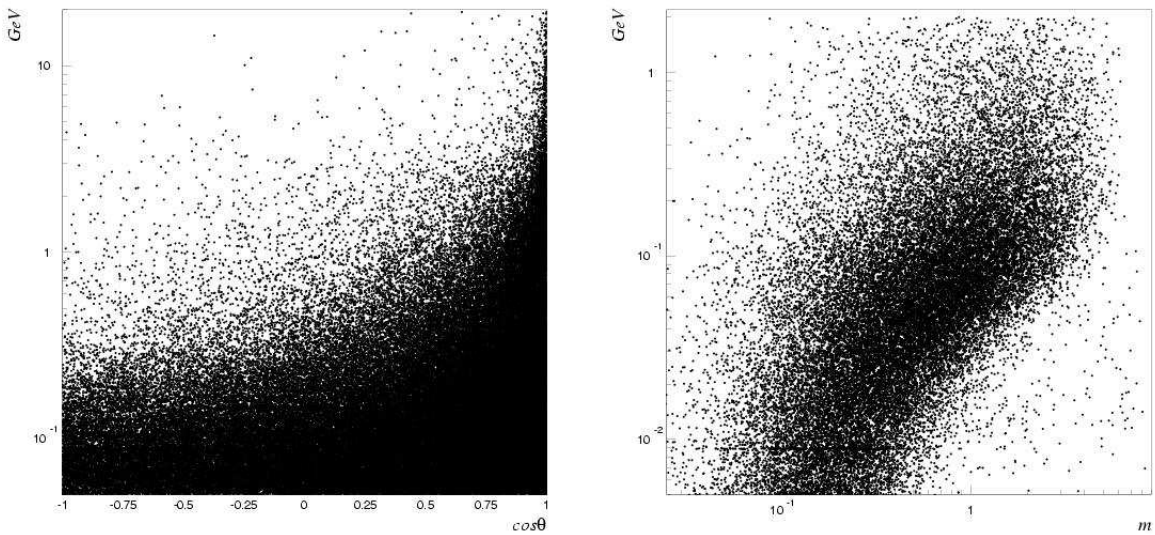

Figure 7.8: (a) Scatter plot of the neutron kinetic energy as function of the angular distribution. (b) Scatter plot of the neutron kinetic energy as function of the covered distance.

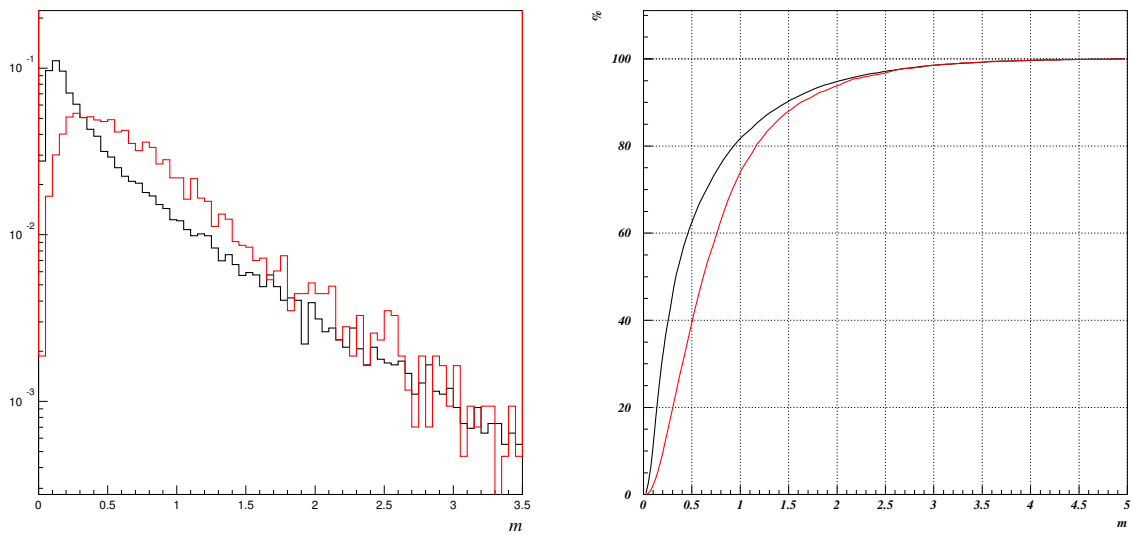

Figure 7.9: (a) Distributions of the distances between the neutron production and capture points (black line) and between neutron production and the center of mass of the $\gamma_{2.2MeV}$ (red line). (b) Cumulative probabilities corresponding to the distributions in Figure (a).

Source of the systematics	Uncertainty	Systematics on the ^{11}C rate (+)	(-)
Mass of the scintillator	4.5%	4.5%	5.5%
Light Yield:	7.5%		
^{11}C energy spectrum		8.2%	0.0%
$\gamma_{2.2MeV}$ energy spectrum		2.3%	2.3%
Total		9.6%	6.0%

Table 7.4: Estimated systematics on the on the ^{11}C rate evaluation from different sources.

$$r = \frac{N}{T \times \varepsilon_{en} \times \varepsilon_{inv} \times \varepsilon_n \times \epsilon(\varepsilon_r, \varepsilon_\gamma)} = 0.64 \pm 0.17\,(stat.)\,^{+0.06}_{-0.04}\,(syst.)\,c/d. \tag{7.14}$$

which is in good agreement (within 1σ) with the expected rate ($r = 0.54 \pm 0.06$) scaled from the measurement at CERN (Table 7.1).

The cosmic μ-induced neutrons detected in CTF have a count rate equals to:

$$r_n = \frac{1.70 \pm 0.06\,c/d}{\varepsilon_n \times \varepsilon_\gamma} = 2.25 \pm 0.08\,c/d. \tag{7.15}$$

The probability (r/r_n) that a neutron is produced in association with a ^{11}C nuclide is equal to 0.28±0.08. The agreement with the predicted value from FLUKA, $r/r_n = 0.31$, represents a further test of the robustness of the results.

Despite the large uncertainties mainly due to the low statistics sample, the agreement of r with the independent measurement at CERN [107] within 1σ shows that the three-fold coincidence method is successful in tagging cosmogenic ^{11}C. Inefficiencies like escaping neutrons or $\gamma_{2.2MeV}$'s will be drastically reduced in Borexino, thanks to the large fiducial mass. Invisible ^{11}C decay channels affect the ^{11}C rate measurement only for a 5%.

In conclusion, the CTF measurement and the results from simulation (Chapter 6) have demonstrated that Borexino has the potential to extend the energy window up to 1.4 MeV in order to probe *pep* and CNO neutrinos.

Conclusion

The work I carried out in the last three years was focused on the development and test of purification systems and data analysis techniques for the Borexino experiment.

Nitrogen plays a fundamental role in the Borexino experiment. It is widely used to remove gaseous contaminants from the scintillator, water and buffer liquid and to flush the large volume ancillary components such as storage tanks, columns and pipes. Nitrogen usually contains radioactive nuclides which can contaminate Borexino materials in the sparging purification step. In order to purify nitrogen we investigated the adsorption technique based on activated carbons and zeolites. While zeolites were proved to be unable to remove argon and krypton, carbon-based adsorbers were found to be highly effective only on krypton nuclides.

At the same time, we tested the purity of nitrogen available on the market. Measuring several samples with mass spectrometer and proportional counters, we identified the proper product which fulfills the Borexino specifications.

The goals of the analysis of the CTF-3 data campaign are twofold: to identify each contamination source and to study the efficiency of the purification system.

Analyses of the delayed coincidences have successfully quantified single isotope activity, even when it was less than 1 event per day (e. g. Ra). The statistical analyses (energy and radial) have confirmed the coincidence results and allowed the identification of the Po contamination, whose high activity was unexpected.

The measurement of background before and after the purification phases has given us the possibility to estimate the efficiencies in purifying single isotopes with water extraction and silica gel. Further tests which include also distillation will be needed to finilize the Borexino purification strategy.

Borexino's primary goal is to measure the solar ^{7}Be flux. However, beyond this objective, Borexino has the potential to probe solar neutrinos from the *pep* fusion process and from the CNO cycle. Several possible background sources determine the detectability of *pep* and CNO solar neutrinos in Borexino. Among such sources, the cosmogenic ^{11}C nuclide plays a central role. ^{11}C is produced underground in reactions induced by the residual cosmic muon flux. We

investigated on the efficiency of the three-fold coincidence with the parent muon track and the subsequent neutron capture on protons in tagging ^{11}C on a one-by-one basis. ^{11}C removal technique imposes a loss of dead volume time detector fraction. Taking into account also the residual activity from trace contamination, we estimated that Borexino can reach a signal to background ratio equal to 1 loosing 5% of the data taking.

The three-fold coincidence has been applied on the CTF data. We evaluated the detection efficiency with a Monte Carlo simulation. Despite the large uncertainties mainly due to the low statistics sample, the agreement of the observed ^{11}C activity with the independent measurement at CERN [107] within 1σ shows that the three-fold coincidence method is a powerful tool for discriminating the ^{11}C background.

Appendix A

Uranium And Thorium Chains

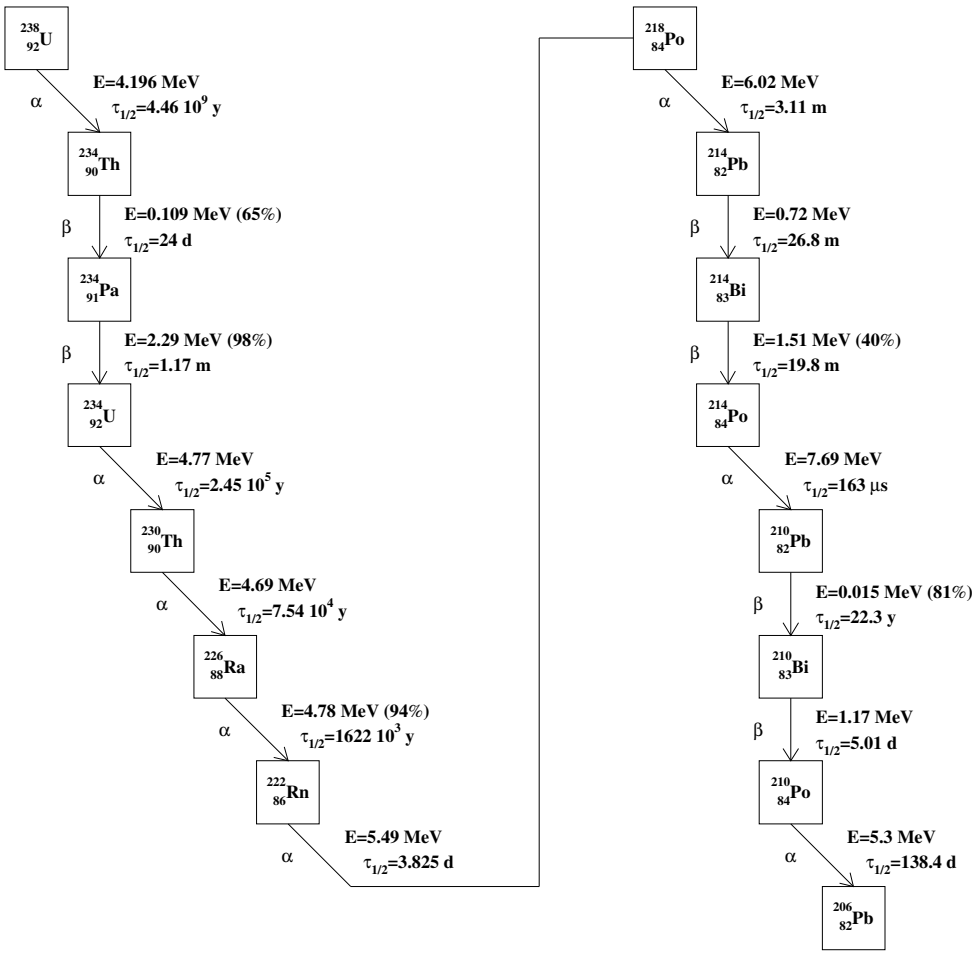

Figure A.1: Uranium Chain

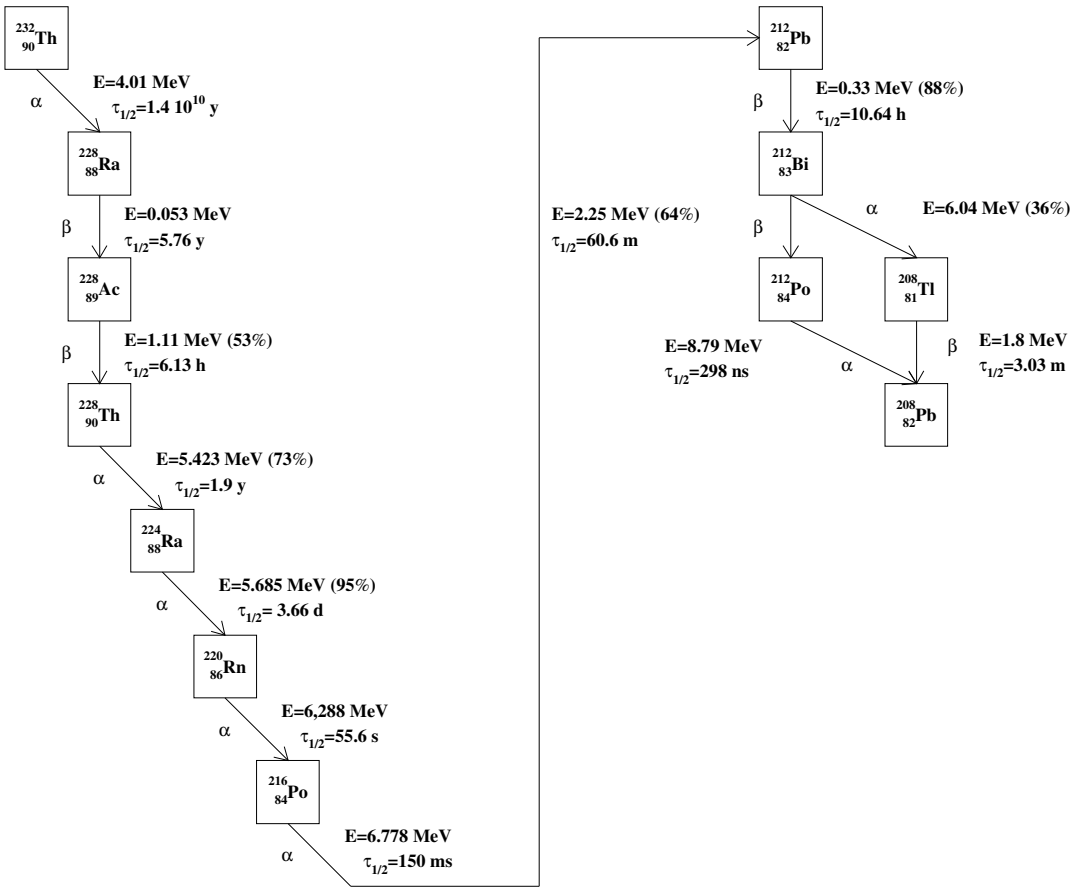

Figure A.2: Thorium Chain

Appendix B

Discarded Runs

run	problem	run	problem	run	problem
2055	E	2245	R	2316	E
2056	E	2248	R	2322	R
2062	L	2253	R	2326	E
2072	E	2255	E	2327	L
2074	E	2259	E	2328	L
2085	L	2260	E	2329	R
2112	E	2261	E	2347	L
2121	L	2262	E	2348	L
2123	E	2263	E	2349	L
2124	E	2264	E	2356	E
2135	E	2267	R	2358	L
2179	E	2271	E	2363	E
2191	L	2272	E	2364	E
2196	R	2273	E	2370	L
2199	R	2276	E	2375	E
2201	R	2277	E	2378	L
2204	E	2278	E	2379	L
2211	E	2279	E	2381	L
2212	E	2280	E	2384	L
2213	E	2291	E	2385	L
2217	R	2294	E	2392	E
2220	E	2296	R	2393	E
2221	E	2297	E	2396	E
2222	E	2299	E	2406	L
2223	E	2300	E	2407	E
2225	E	2306	E	2414	E
2227	E	2311	R	2415	E
2242	E	2313	E	2423	E

Table B.1: List of discarded runs: (L) = Laser Run, (E) = Electronic Problem, (R) = High Muon Trigger Rate (possible noise).

Bibliography

[1] C. L. Cowan and F. Reines, *Search for antineutrino interaction with deuterons*, Phys. Rev. 107, (1957) 1609-1611.

[2] H. A. Bethe and C. L. Critchfield, *The formation of deuterons by proton combination*, Phys. Rev. 54, (1938) 248-254.

[3] C. F. von Weizsäcker, *Über Elementumwandlungen in Innern der Sterne. II*, Physik. Z., 39 (1938) 633.

[4] H. A. Bethe, *Energy Production in Stars* , Phys. Rev., 55, 434 (1939).

[5] S. Bludman, N. Hata, P.Langacker, *Astrophysical solutions are incompatible with the Solar Neutrino data*, Phys.Rev. D 49 (1994) 3622-3625.

[6] J. N. Bahcall, *The luminosity constraint on solar neutrino fluxes*, Phys. Rev. C 65 (2002).

[7] J. N. Bahcall, M. H. Pinsonneault and S. Basu, *Solar Models: current epoch and time dependences, neutrinos, and helioseismological properties*, Astrophys. J. 555, (2001) 990-1012.

[8] J. N. Bahcall and M. H. Pinsonneault, *What do we (not) know theoretically about solar neutrino fluxes?*, Phys. Rev. Lett. 90 21802, (2004).

[9] A. Formicola et al., *Astrophysical S-factor of* $^{14}N(p, \gamma)^{15}O$, Phys. Lett. B 591 (2004), 61.

[10] R. Davis, D.S. Harmer, and K.C. Hoffman, *Search for Neutrinos from the Sun*, Phys. Rev. Lett. 20, (1968) 1205-1209.

[11] B. Pontecorvo, *Inverse β process*, National Research Council of Canada, Division of Atomic Energy, Chalk River Laboratory Report No. P.D. 205, 1946 (unpublished). Available at http://pontecorvo.jinr.ru .

[12] SAGE collaboration (J. N. Abdurashitov e.t al.), *Measurement of the solar neutrino capture rate by SAGE and implications for neutrino oscillations in vacuum*, Phys. Rev. Lett. 83, (1999) 4686-4689.

[13] GALLEX Collaboration (W. Hampel et al.), *GALLEX solar neutrino observations: results for GALLEX IV*, Phys. Lett. B 447 (1999) 127-133.

[14] GNO Collaboration (M. Altmann et. al.), *GNO Solar Neutrino observations: results for GNO I*, Phys. Lett. B 490 (2000) 16-26.

[15] The Kamiokande Collaboration, H. Hirata et al., *Observation of ^8B Solar Neutrinos in the Kamiokande-II Detector*, Phys. Rev. Lett. 63, (1989) 16.

[16] The Kamiokande Collaboration, Y. Fukuda et al., *Solar Neutrino Data Covering Solar Cycle 22*, Phys. Rev. Lett. 77, (1996) 1683.

[17] The Super-Kamiokande Collaboration, Y. Fukuda et al., *Solar ^8B and hep Neutrino Measurements from 1258 Days of Super-Kamiokande Data*, Phys. Rev. Lett. 86, (2001) 5651.

[18] SNO Collaboration (McDonald et.al.), *The Sudbury Neutrino Observatory*, Nucl. Inst. Meth. A 449, (2000) 172.

[19] SNO Collaboration, (MacDonald et al.), *Measurement of the rate of $\nu_e + d \rightarrow p + p + e^-$ interactions produced by ^8B neutrinos at the Sudbury Neutrino Observatory*, Phys. Rev. Lett. 87, (2001) 071301.

[20] The SNO Collaboration, (Q. R. Ahmad et al.), *Direct evidence for neutrino flavor transformation from neutral-current interactions in the Sudbury Neutrino Observatory*, Phys. Rev. Lett., 89, (2002) 011301.

[21] The SNO Collaboration, (Q. R. Ahmad et al.), *Measurement of the total active ^8B solar neutrino flux at the Sudbury Neutrino Observatory with enhanced neutral current sensitivity*, Phys. Rev. Lett. 92, (2004) 181301.

[22] The SNO Collaboration, (Q. R. Ahmad et al.), *Measurement of day and night neutrino energy spectra at SNO and constraints on neutrino mixing parameters,* Phys. Rev. Lett. 89, (2002) 011302.

[23] J. N. Bahcall and H. A. Bethe, *Solution of the solar-neutrino problem*, Phys. Rev. Lett. 65, (1990) 2233-2235.

[24] Courtesy from the John N. Bahcall Web Site: http://www.sns.ias.edu/~jnb/.

[25] J. N. Bahcall, M. H. Pinsonneault, S. Basu and J. Christensen-Dalsgaard, *Are standard solar models reliable?,* Phys. Rev. Lett. 78, (1997) 171-174.

[26] B. Pontecorvo, *Mesoniums and antimesoniums*, Sov. Phys. JETP, 6, (1958) 429 .

[27] Z. Maki, M. Nakagawa and S. Sakata, *Remarks on the unified model of elementary particles*, Prog. Theor. Phys., 28, (1962) 870.

[28] B. Pontecorvo, *Neutrino experiments and the question of leptonic-charge conservation,* Zh. Eksp. Teor. Fiz., 53, (1967) 1717.

[29] S.P. Mikheyev, A.Y. Smirnov, *Resonance enhancement of oscillations in matter and Solar Neutrino spectroscopy*, Sov. Jour. Nucl. Phys. 42, (1985) 913-917.

[30] S.P. Mikheyev, A.Y. Smirnov, *Neutrino oscillations in a variable density medium and ν-bursts due to the gravitational collapse of stars*, Sov. Phys. JETP 64, (1986) 4-7 .

[31] L. Wolfenstein, *Neutrino oscillations in matter*, Phys. Rev. D 17, (1978) 2369-2374.

[32] C. W. Kim and A. Pevsner, *Neutrinos in physics and astrophysics*, Harwood Academic Publishers, Chur, Switzerland (1993).

[33] J. N. Bahcall, M. C. Gonzalez-Garcia and C. Pena-Garay, *Before and After: How has the SNO NC measurement changed things?*, JHEP 07, (2002) 054.

[34] KamLAND Collaboration, *Neutrino physics with the KamLAND detector*, Nucl. Phys. Proc. Suppl. 87, (2000) 312-314.

[35] KamLAND Collaboration, *First results from KamLAND: evidence for reactor antineutrino disappearance*, Phys. Rev. Lett. 90, 021802 (2003).

[36] KamLAND Collaboration, *Measurement of neutrino oscillation with KamLAND: evidence of spectral distortion*, hep-ex/0406035 (2004).

[37] J. N. Bahcall, M. C. Gonzalez-Garcia and C. Pena-Garay, *Solar neutrinos before and after KamLAND*, JHEP 0302, (2003) 009.

[38] J. N. Bahcall, M. C. Gonzalez-Garcia and C. Pena-Garay, *Solar neutrinos before and after Neutrino 2004*, JHEP 08, (2004) 016.

[39] IMB Collaboration, *The electron neutrino and the muon neutrino content of the atmospheric flux*, Phys. Rev. D46, (1992) 3720-3724.

[40] Kamiokande Collaboration, *Observation of a small atmospheric ratio in Kamiokande*, Phys. Lett. B280 (1992), 146-152.

[41] Kamiokande Collaboration, *Atmospheric muon-neutrino/electron-neutrino ratio in the multi-GeV energy range*, Phys. Lett. B 335, (1994) 237.

[42] Soudan 2 Collaboration, *Measurement of the atmospheric neutrino flavor composition in Soudan-2,* Phys Lett B 391, (1997) 491-500.

[43] MACRO Collaboration, *The observation of up-going charged particles produced by energy muons in underground detectors,* Astrop. Phys. 9 (1998), 105-117.

[44] Super-Kamiokande Collaboration, *Tau neutrino favored over sterile neutrinos in atmospheric muon neutrino oscillations*, Phys. Rev. Lett., 85, (2000) 3999.

[45] G. L. Fogli, E. Lisi, A. Marrone, D. Montanino, *Status of atmospheric $\nu_\mu \leftrightarrow \nu_\tau$ oscillations and decoherence after the first K2K spectral data,* Phys.Rev. D67 (2003) 093006.

[46] K2K collaboration, *Search for electron neutrino appearance in a 250 km long baseline experiment*, Phys. Rev. Lett. 93, (2004) 051801.

[47] J. N. Bahcall and C. Pena-Garay, *A road map to solar neutrino fluxes, neutrino oscillation parameters, and tests for new physics*, Jour. High Energy Phys. 0311 004, (2003).

[48] Borexino Collaboration (G. Alimonti et al.), *The science and technology of Borexino : a real time detector for low energy solar neutrinos*, Astrop. Phys. 16, (2001) 205-234.

[49] L. Cadonati, *The Borexino solar neutrino experiment and its scintillator containment vessel,* Ph.D. thesis, Princeton University (2001).

[50] Borexino Collaboration (G.Alimonti et al.), *A large scale low background liquid scintillator detector: the Counting Test Facility* , Nucl. Inst. Meth. A 406 (1998) 411.

[51] Borexino Collaboration (G.Alimonti et al.), *Light propagation in a large volume liquid scintillator* , Nucl. Inst. Meth. A, 440 (2000), 360.

[52] J.B. Birks, *The theory and practice of scintillation counting*, Pergamon Press, 1974.

[53] M. Deutsch, *Proposal for a cosmic ray detection system for the Borexino solar neutrino experiment*, Massachussetts Institute of Technology, 1996.

[54] M. Chen, *Muon veto supplement proposal for the Borexino Experiment*, editor. National Science Foundation Princeton University, Apr 1998.

[55] R. Dossi, A. Ianni, G. Ranucci, and O. Ju. Smirnov, *Methods for single photoelectron counting with photomultipliers*, Nucl. Instr. Meth. A, 451, 623 (2000).

[56] V. Lagomarsino and G. Testera, *A gateless charge integrator for Borexino energy measurement*, Nucl. Instr. Meth. A, 430, 435 (1999).

[57] F. Gatti et al., *The Borexino read out electronics and trigger system*, Nucl. Instr. Meth. A, 461, 474 (2001).

[58] F. Elisei et al., *Measurements of liquid scintillator properties for the Borexino detector*, Nucl. Instr. Meth. A, 400, 53 (1997).

[59] G. Ranucci, A. Goretti, and P. Lombardi, *Pulse-shape discrimination of liquid scintillators*, Nucl. Instr. Meth. A, 412, 374 (1998).

[60] G. Ranucci, *An analytical approach to the evaluation of the pulse shape discrimination properties of scintillators*, Nucl. Instr. Meth. A, 354, 389 (1995).

[61] G. Ranucci et al., *Scintillation decay time and pulse shape discrimination of binary organic liquid scintillators for the Borexino detector*, Nucl. Instr. Meth. A, 350, 338 (1994).

[62] The Borexino Collaboration, G. Alimonti et al., *Science and technology of Borexino: a real-time detector for low energy solar neutrinos*, Astrop. Phys., 16(3), 205 (2002).

[63] J. Maneira. In A. Mourao, M. Pimenta, and P. Sa, editors, Proc. Second Intern. Workshop on "*New Worlds in Astroparticle Physics*", Faro, Portugal, page 131, 1998.

[64] B. Caccianiga et al, *A multiplexed optical-fiber system fro the PMT calibration of the Borexino experiment*, Nucl. Instr. Meth. A496 (2003), 353-361.

[65] M. Johnson et al., *A ^{222}Rn Source for Low-background Liquid Scintillation Detectors*, Nucl. Instr. Methods A 414 (1998), 459.

[66] J.B. Benziger et al., *A scintillator puri cation system for a large scale solar neutrino experiment*, Nucl. Instr. Meth. A, 417 (1998), 278.

[67] BOREXINO Collaboration, *Phenylxylylethane (PXE): a high-density, high-flashpoint organic liquid scintillator for applications in low-energy particle and astrophysics experiments*, Nucl. Instr. Meth., (2004) physics/0408032.

[68] G. 't Hooft, *Prediction for neutrino-electron cross-sections in Weinberg's model of weak interaction*, Phys. Lett. B 37 (1971) 195.

[69] J. Benziger, F. P. Calaprice et al. editors, *A proposal for participation in the Borexino solar neutrino experiment*, Princeton University, 1996.

[70] S. Schoenert, *Probing the solar MSW larg mixing angle aolution with Terrestrial antineutrinos from European nuclear reactors with Borexino*, Nucl. Phys. B (Proc. Suppl.), 70 (1999), 195.

[71] R. S. Raghavan et al., *Measuring the global radioactivity in the Earth by multidetector antineutrino spectroscopy*, Phys. Rev. Lett., 80 (1998), 635.

[72] C. Rothschild et al., *Antineutrino geophysics with liquid scintillator detectors*, Geophys. Res. Lett., 25 (1998), 1083.

[73] L. Cadonati, F. Calaprice, and M. Chen. *Supernova neutrino detection in Borexino*, 2000.

[74] L. Cadonati, *Supernova neutrino detection in Borexino*, Borexino collaboration internal memo, Princeton University, February 1999.

[75] M. Aglietta et al., *Upper limit on the solar anti-neutrino flux according to LSD data*, JETP Lett., 63 (1996), 791.

[76] H. H. Loosli, H. Oeschger, ^{37}Ar *and* ^{81}Kr *in the atmosphere*, Earth Planet. Sci. Lett. 7, (1969) 67.

[77] Langmuir I., *The adsorption of gases on plane surfaces of glass, mica and platinum,* J. Am. Chem. Soc. 40 (1918), 1361-1403.

[78] S. Brunauer et al., *Adsorption of gases in multimolecular layers*, J. Am. Chem. soc. 60 (1938), 309-319.

[79] K. S. W. Sing et al., *Reporting physisorption data for gas/solid systems with specific reference to the determination of surface area and porosity,* Pure & Appl. Chem. 57 (1985), 603-619.

[80] S. Maurer et al, *Henry coefficients of adsorption predicted from solid Hamaker constants*, Chem. Eng . Sci. 56 (2001), 3443-3453.

[81] W. A. Steele, *The interaction of gases with solid surfaces*, Pergamon Press Oxford (1974).

[82] A. S. Said, *Theory and mathematics of chromatography,* Huethig Verlag, Heidelberg (1981).

[83] J. Hopp et al., Max-Planck-Institut fur Kernphysik Hedielberg, Annual Report (2000), 299-300.

[84] J. Kiko et al., Max-Planck-Institut fur Kernphysik Hedielberg, Annual Report (1992), 251.

[85] G. Zuzel et al., *Ar and Kr concentrations in nitrogen as a measure of the* ^{39}Ar *and* ^{85}Kr *activity in connection with the solar neutrinos experiment Borexino*, accepted for publication in App. Rad. Isot. (2004).

[86] S. Schoenert, K. H. Schuhbeck, *A liquid handling and purification modeule for CTF and Borexino,* Borexino Internal Report (1999).

[87] R. Von Hentig et al. *Determination of radioactive trace elements in ultra low background detectors by means of neutron activation Analysis*, Czech. J. Phys., 49 Suppl. S1 (1999), 277

[88] The Borexino Collaboration, G. Alimonti, et al. *Measurement of the ^{14}C abundance in a low background liquid scintillator*, Phys. Lett. B, 422 (1998), 349.

[89] The Borexino Collaboration, G. Alimonti et al., *Ultra-low background measurements in a large volume underground detector*, Astrop. Phys., 8 (1998), 141.

[90] F. James, *MINUIT*, Technical report, CERN Program Library, (1994).

[91] C. Galbiati, *Data taking and analysis of the Counting Test Facility of Borexino*, Ph.D. thesis, Università degli Studi di Milano, 1999.

[92] The Borexino Collaboration, H. O. Back et al., *Search for electron decay mode $e \rightarrow \gamma + \nu$ with prototype of Borexino detector* , Phys. Lett. B, 525(1-2), 29 (2002).

[93] The Borexino Collaboration, H. O. Back et al., *New limits on nucleon decays into invisible channels with the BOREXINO counting test facility* , Phys. Lett. B, 563(1- 2), 23 (2003).

[94] Garcia and Brown, Phys. Rew. C vol. 52 N 6, 3416-27 (1995).

[95] O. Yu. Smirnov et al., Phys. of Atom. Nucl. Vol. 66 No. 4, 712-723 (2003).

[96] Calaprice and Holstein, Nucl. Phys. A273, 301 (1976).

[97] Wietfeldt et al., Phys. Rev. C 52, 1028 (1995).

[98] Genz et al., Z. Phys. A 341, 9 (1991).

[99] A. Pocar, *Low background techniques and experimental challenges for Borexino and its nylon vessels,* Ph.D. Thesis at Princeton University (2003).

[100] S. Bonetti, O. Donghi, C. Salvo and G. Testera, Borexino Internal Report (1998).

[101] W. R. Leo, *Techniques for nuclear and particle physics experiments*, Springer-Verlag, page 37 (1994).

[102] M. Neff, *Internal note on the laboratory measurements of quenching factors*, (1996).

[103] K. McCarty and A. Pocar, *Internal memo on the CTF-3 radial event distribution*, Borexino Internal Report, (2004).

[104] D. Franco, Tesi di laurea, Universita' di Milano (2001).

[105] J. Maneira, *Calibration and monitoring for the Borexino solar neutrino experiment*, Ph.D. thesis, Universidade de Lisboa, (2001).

[106] M. Deutsch, contribution to a BOREXINO general meeting (1997).

[107] T. Hagner et al., *Muon-induced production of radioactive isotopes in scintillation detectors*, Astr. Part. Phys. 14 (2000) 33-47.

[108] L. Katz et al, Can. Jour. Phys. 29 (1951), 518; L. Cohen et al, Phys. Rev. 2 (1959), 263; V. Emma et al, Phys. Rev. 118 (1960), 1297; J. Roalsvig et al, Can. Jour. Phys. 39 (1961), 643; H. Fuchs et al, Zeit. Nat. A 17 (1962), 439; W. Del Bianco et al Phys. Rev. 126 (1962), 709;V. Verbinski et al, Nucl. Phys. 73 (1965), 398; W. Lochstet et al, Phys. Rev. 141 (1966), 1002; E. Bazhanov et al, Yad. Fiz. 3 (1966), 711; H. Schier et al, Nucl. Phys. A 229 (1974), 93; J. Annand et al, Phys. Rev. Lett. 71 (1993), 2703.

[109] M. Goldhaber and E. Teller, Phys. Rev. 74 (1948), 1046.

[110] J. Brolley et al, Phys. Rev. 88 (1952), 618; O. Brill et al, Dok. Akad. Nauk 136 (1961), 55; P. Dimbylow, Phys. Med. Biol. 25 (1980), 637; P. Welch et al, Bull. Am. Phys. Soc. 26 (1981), 708; B. Anders et al, Zeit. Phys. A 301 (1981), 353; T. Soewarsono et al, JAERI Tokai Reports 27 (1992), 354; Y. Uno et al, Nucl. Sci. Eng. 122 (1996) 247; F. Nasyrov et al, Atom. Ener. 25 (1968), 437; E. Kim et al, Nucl. Sci. Eng. 129 (1998), 209.

[111] ENDF/B-VI, *Evaluated Nuclear Data File*, National Nuclear Data Center, Brookhaven National Laboratory (1990).

[112] J. Cumming et al, Phys. Rev. 111 (1958), 1386; V. Parikh, Nucl. Phys. 18 (1960), 628; P. Berio, Phys. Rev. 119 (1960), 316; N. Horwitz et al, Phys. Rev. 117 (1960), 1361; K. Goebel et al, Nucl. Phys. 24 (1961), 28; J. Cumming et al Phys. Rev. 125, (1962) 2078; H. Gauvin et al, Nucl. Phys. 39 (1962), 447; G. Butler et al, Phys. Rev. C 6 (1972), 1153; M. Barlett et al, Phys. Lett. B 264 (1991) 21; D. Carman et al, Phys. Lett. B 452 (1999), 8.

[113] P. Roos et al, Nucl. Phys. A 255 (1975), 187; K. Hosono et al, Nucl. Phys. A 343 (1980), 234; H. Ohnuma et al Jour. Phys. Soc. Japan 48 1812; G. Smith et al, Phys. Rev. C 30 (1984), 593.

[114] D. Chivers et al, Nucl. Phys A 126 (1969), 129; K. Hogstrom et al, Nucl. Phys A 215 (1973), 598; B. Dropesky et al, Phys. Rev. C 34 (1975), 821; M. Sternheim and R. Silbar, Phys. Rev. Lett. 34 (1975), 824; B. Lieb et al, Phys. Rev. C 19 (1979), 2405; J. Amann et al, Phys. Rev. Lett. 40 (1978), 758.

[115] W.C. Barber, Phy. Rev. 111, (1958) 1642; G. Kuhl and U. Kneissl, Nucl. Phys. A 195, (1972) 559; E. Wolynec et al., Phys. Rev. C 11, (1975) 1083; U. Kneissl, G. Kuhl, and K.H. Leister, Z. Physik A 281, (1977) 35; N.G. Shevchenko et al., Sov. J. Nucl. Phys. 28, (1978) 5.

[116] Galbiati et al., *Cosmogenic ^{11}C production and sensitivity of organic scintillator detectors to pep and CNO neutrinos,* hep-ph/0411002.

[117] MACRO Collaboration, Astr. Part. Phys. 10, (1999) 11-20.

[118] A. Fassò et al., *New developments in FLUKA modelling hadronic and EM interactions,* KEK Proceedings 97-5, (1997) 32-43.

[119] A. Fassò et al, *Electron-photon transport in FLUKA: Status,* Proceedings of the Monte-Carlo 2000 Conference, Lisbon, October 23-26 2000 (2001).

[120] G. Battistoni et al., in Proceedings of Vulcano Workshop on Frontier Objects in Astrophysics and Particle Physics, 1998, hep-ex/9809006.

[121] V.A. Kudryavtsev et al., *Simulations of muon-induced neutron flux at large depths underground*, Nucl. Instr. and Meth. in Phys. Res. A 505 (2003) 688-698.

[122] Y. F. Wang et al., *Predicting neutron production from cosmic-ray muons*, Phys. Rew. D 64 (2001) 013012.

[123] O. Ryazhskaya and G. Zatsepin, Izv. Akad. Nauk USSR Ser. Fiz. 29, (1956), 1946.

[124] M. Deutsch, *Proposal to NSF for a Borexino Muon Veto,* MIT (1996).

[125] MACRO Collaboration, Astr. Part. Phys. 10, (1999) 11-20.

[126] A. Fassò et al., *New developments in FLUKA modelling hadronic and EM interactions,* KEK Proceedings 97-5 (1997), 32-43.

[127] A. Fassò et al, *Electron-photon transport in FLUKA: Status,* Proceedings of the Monte-Carlo 2000 Conference, Lisbon, October 23-26 2000 (2001).

[128] G. Battistoni et al., in Proceedings of Vulcano Workshop on Frontier Objects in Astrophysics and Particle Physics, 1998, hep-ex/9809006.

[129] V.A. Kudryavtsev et al., *Simulations of muon-induced neutron flux at large depths underground*, Nucl. Instr. and Meth. in Phys. Res. A 505 (2003) 688-698.

[130] Y. F. Wang et al., *Predicting neutron production from cosmic-ray muons*, Phys. Rew. D 64 (2001), 013012.

[131] O. Ryazhskaya and G. Zatsepin, Izv. Akad. Nauk USSR Ser. Fiz. 29, (1956) 1946.

[132] M. Deutsch, *Proposal to NSF for a Borexino Muon Veto,* MIT (1996).V. Kudryavtsev et al., Nucl. Inst. Meth. A 505 (2003), 688.